Interactions of colloidal particles with simple electrolytes and polyelectrolytes

Skarba, Michal

How to cite

SKARBA, Michal. Interactions of colloidal particles with simple electrolytes and polyelectrolytes. Doctoral Thesis, 2008. doi: 10.13097/archive-ouverte/unige:610

This publication URL: https://archive-ouverte.unige.ch/unige:610
Publication DOI: 10.13097/archive-ouverte/unige:610

UNIVERSITÉ DE GENÈVE FACULTÉ DES SCIENCES
Section de chimie et biochimie
Département de chimie minérale,
analytique et appliquée Professeur Michal Borkovec

Interactions of Colloidal Particles with Simple Electrolytes and Polyelectrolytes

THÈSE

présentée à la Faculté des sciences de l'Université de Genève
pour obtenir le grade de Docteur ès sciences, mention chimie

par
Michal Skarba
de
Malinovo (Slovaquie)

Thèse N° 3973

GENÈVE
Atelier de Reproduction de la Section de physique
2008

UNIVERSITÉ DE GENÈVE

FACULTÉ DES SCIENCES

Doctorat ès sciences mention chimie

Thèse *de Monsieur Michal SKARBA*

intitulée :

" Interactions of Colloidal Particles with Simple Electrolytes and Polyelectrolytes "

La Faculté des sciences, sur le préavis de Messieurs M. BORKOVEC, professeur ordinaire et directeur de thèse (Département de chimie minérale, analytique et appliquée), M. MORBIDELLI, professeur (Eidgenössische Technische Hochschule Zürich – Departement Chemie-/Bioingenieurwissenschaften – Zürich, Suisse), et O. WENGER, professeur adjoint suppléant (Département de chimie minérale, analytique et appliquée), autorise l'impression de la présente thèse, sans exprimer d'opinion sur les propositions qui y sont énoncées.

Genève, le 26 mai 2008

Thèse - 3973 -

Le Doyen, Jean-Marc TRISCONE

N.B. - La thèse doit porter la déclaration précédente et remplir les conditions énumérées dans les "Informations relatives aux thèses de doctorat à l'Université de Genève".

Nombre d'exemplaires à livrer par colis séparé à la Faculté : - 7 -

Contents

Résumé

Dans ce travail de thèse, les interactions des particules colloïdales avec des espèces chargées ont été étudiées par des méthodes de diffusion de la lumière et méthodes électrochimiques. Nous avons étudié ces interactions avec trois différents types d'espèces, en commençant par de simples électrolytes, ensuite avec des polyéletrolytes et finalement avec des particules ayant des charges opposées.

Après l'introduction, le deuxième chapitre présente une étude sur l'agrégation et le comportement de l'accumulation de la charge des particules colloïdales de silice. La silice est bien connue pour ses comportements contradictoires par rapport à la théorie (DLVO). Dans certaines conditions, pour lesquelles la théorie DLVO prédit une agrégation rapide, les particules de silice restent stables. Pourtant, notre étude sur des particules colloïdales de silice préparées selon le procédé de Stöber révèle un comportement qui est quantitativement en accord avec la théorie DLVO. De plus, le phénomène est quantitativement en accord avec cette théorie lorsque les particules ont subi un traitement thermique. Des mesures potentiométriques démontrent que ce traitement thermique modifie substantiellement les propriétés de charges des particules. En même temps, ce traitement n'a presque aucune influence sur les valeurs de mobilités électrophorétiques. Nous suspectons que la stabilité de la suspension des particules qui ont non-traitées thermiquement est causée par la présence d'une couche formée de chaines d'acide polysilicilique ancrées aux surfaces des particules. Toutes les mesures mentionnées ont été effectuées en présence d'un simple électrolyte monovalent.

Dans le chapitre 3, nous avons étendu l'étude sur le comportement de l'accumulation de la charge des particules de silice en présence des simples électrolytes divalents. Dans ce cas, les cations divalents génèrent une différence appréciable dans les courbes de titrage et les valeurs de mobilités électrophorétiques sont elles aussi qualitativement différentes. Selon les courbes de titrage, les particules de silice sont chargées négativement, mais pour

les mêmes conditions expérimentales (pH et concentration de sel élevé) les mobilités électrophorétiques montrent que la surface des particules est chargée positivement. Ce phénomène d'inversion de charge est dû à la forte corrélation entre les ions. Ceci a été confirmé par des simulations de type Monte Carlo.

Les chapitres 4 et 5 sont dévoués à l'étude des interactions entre des particules colloïdales et des poly-ions ayant une charge opposée (polyélectrolytes) en présence de simples électrolytes monovalents. La structure de la couche de polyélectrolytes qui sont adsorbés a été étudiée par la méthode de diffusion de lumière dynamique et de la diffusion de neutrons à bas angle d'incidence. Nous avons présenté une technique de diffusion de la lumière qui permet de mesurer des couches de polyélectrolytes aussi minces que quelques nanomètres. Cette technique est capable de distinguer entre l'agrégation des particules et la croissance de la couche de polyélectrolytes. Les effets de la concentration de polyélectrolyte, de la charge et de la masse moléculaire sur l'épaisseur de la couche ont été étudiés pour trois systèmes différents. Malgré les grandes différences entre les particules et les polyélectrolytes utilisés, les résultats expérimentaux montrent plusieurs caractéristiques communes entre les différentes couches adsorbées. Des mesures indépendantes effectuées par diffusion de neutrons à bas angles d'incidence ont confirmé que la couche est aussi mince que 1.1 nm et elle est très compacte avec une fraction volumique de polymère de 0.6.

Finalement, nous avons étudié les interactions entre les particules colloïdales et d'autres types de particules à charge opposée. Les valeurs de taux d'agrégation hétérogènes ont été mésurées par les méthodes de diffusion de lumière statique et dynamique pour une large gamme des différents paramètres et en présence de homo-agrégation. Pour la première fois, les valeurs absolues des constantes des taux d'agrégation hétérogènes dans le régime d'agrégation rapide ont été précisément déterminées par des mesures de diffusion dynamique de lumière à multi-angle.

Abstract

Interactions of colloidal particles with other charged species are investigated by means of scattering and electrochemical methods. We examine interactions with three different types of species, starting from simple electrolytes, through polyelectrolytes to oppositely charged particles.

After introduction, the second chapter presents a study on the aggregation and charging behavior of colloidal silica particles. Silica is known to contradict the theory of Derjaguin, Landau, Verwey, and Overbeek (DLVO). At certain conditions, for which the DLVO theory predicts fast aggregation, silica particles stay stable. However, investigation of colloidal silica prepared according to the Stöber process revealed behavior, which quantitatively agreed with DLVO theory. After heat treatment of particles, even quantitative accordance with the theory was achieved. The heat treatment of particles substantially modified their charging properties, as examined with potentiometric titration. On the other hand, heat treatment had almost no influence on electrophoretic mobilities. We suspect that the suspension stability of the unheated particles is caused by the presence of a hairy layer of polysilicic acid chains on the surface. All mentioned measurements were performed in presence of a simple monovalent electrolyte.

In chapter 3, we extended the studies of charging behavior of silica particles for the case when simple divalent electrolyte is present. While divalent cations caused quantitative difference in titration characteristics, electrophoretic mobilities were qualitatively different. According to titration curves, silica particles possessed negative charge, but at the same experimental conditions (high salt and high pH), electrophoretic mobilities showed positively charged surface. The observed overcharging phenomena arose from strong ion-ion correlations, as confirmed by Monte Carlo simulations of titration and electrokinetic behavior.

Chapters 4 and 5 are devoted to the interactions of colloidal particles with oppositely charged organic polyions (polyelectrolytes) in presence of mono-

valent simple electrolyte. Structure of adsorbed polyelectrolyte monolayer was investigated by combination of dynamic light scattering and small angle neutron scattering. We presented a light scattering technique which allows to measure polyelectrolyte layer as thin as few nanometers. The technique rigorously separates aggregation of particles from growth of polyelectrolyte layer during an adsorption experiment. Effect of polyelectrolyte dose, charge and molecular mass on layer thickness was investigated for three different systems. Despite high variance in used particles and polyelectrolytes, experiments showed several common features of the adsorbed layer. Independent measurements by small angle neutron scattering confirmed that the layer is as thin as 1.1 nm and very compact, having the polymer volume fraction of 0.6.

Finally, in chapter 6 we studied interactions of colloidal particles with another type of oppositely charged particles. Heteroaggregation rate constants were measured with static and dynamic light scattering over a wide range of different parameters and in presence of homoaggregation. With multiangle dynamic light scattering, we were able to estimate absolute heteroaggregation rate constants accurately in the fast aggregation regime for the first time.

1 Introduction

1.1 Colloids and polyelectrolytes

Colloidal dispersions

In the beginning of 20th century, successful attempts were made to bridge the gap between molecular solutions on one hand and coarse mechanical suspensions on the other [1]. ”The world of neglected dimensions”, as the colloid chemistry was called before, became a very important separate discipline. As one of the pioneers in this field W. Ostwald put it, ”Since the birth of the so-called classical physical chemistry of the molecular solutions, at the end of 19th century, no branch of physics or chemistry has arisen which can be compared in importance, so far as scientific and technical applications are concerned, with that of colloid chemistry”.

Colloids are defined as dispersed systems, in which the dispersed particles have at least one dimension between 1 nm and 1 μm. Dispersed systems are known for all combinations of phases (solid, liquid and gaseous), except for gases, which are all miscible. Thus, we know eight categories of colloidal systems according to the phase of dispersed medium (particles) and continuous medium (solvent). Let us take a brief look on the group of dispersions where the continuous medium is liquid. If the dispersed medium is solid, dispersion is called colloidal suspension or sol (i.e. paint). Fine particles of unmiscible liquids can form an emulsion (i.e. milk), whereas gas particles dispersed in liquid are known as foam (i.e. whipped cream).

Colloids, surfactants, liquid crystals and polymers are often referred to as ”soft” matter [2], which originates from their macroscopic mechanical properties. The softness is a result of weak ordering of dispersed particles, which comes from lack of three-dimensional atomic long-range order found in crystalline solid. Nevertheless, there is always a degree of local order at least as great as that in liquid.

When immersed in an aqueous solution, some particles develop a charge at their surface. For example, this is the case for metal oxides such as SiO_2, TiO_2, Fe_2O_3. Charge on the particle surface results from dissociation of surface groups. Due to electrostatic interactions and thermal motion, solvated ions accumulate at the mineral/solution interface and form an ionic cloud, known as electric double layer.

One of the most important features of colloidal dispersions is stability of dispersion against aggregation. A very useful tool for understanding the stability of colloids is the theory by Derjaguin, Landau, Verwey and Overbeek (DLVO). The theory is based on balance of forces between electrical double layers, which are repulsive for similarly charged particles, and long-range van der Waals forces, which are usually attractive. In this theory, potential energy of particles is a sum of the two mentioned contributions. From the plot of potential energy as a function of separation between the surfaces of charged colloidal particles (fig. 1), it is possible to assess the stability of colloidal system against aggregation. If an electrolyte is present in colloidal dispersion, repulsive forces between electrical double layers will be screened. In the latter case, the potential energy curve has deep attractive minimum at small separations, the system will be unstable and aggregation will occur.

Interaction of colloidal particles with polyelectrolytes

Polyelectrolytes are polymers carrying charged ionizable groups. Depending on the charge, polyelectrolytes can be anionic or cationic. Polyampholytes are polyelectrolytes which possess both positive and negative chargeable groups. Synthetic polyelectrolytes have a wide range of industrial applications in oil recovery, paper making, mineral processing, etc. DNA and proteins are examples of natural polyelectrolytes.

For practical use of colloids, there is often a need to modify their properties. For example, in the process of waste water treatment, it is necessary to coagulate the dispersed particles. On the other hand, for many colloidal materials, we require that they will stay stable for a long time (e.g. paint).

Properties of colloidal particles can be substantially modified by attaching polyelectrolyte to the particle surface. This process is very important for many technologies, such as colloidal stabilization, lubrication, adhesion, water purification, drug transport, fabrication of hollow capsules [4].

There are two limiting cases of the way how a polymer can be attached to a surface: grafting by a covalent bond or adsorption from solution [5]. In the first case, the polyelectrolyte chain is terminally grafted to the surface forming a so-called brush [6]. In such a system, the amount of polymer attached to the surface is fixed and as response to the change of solvent properties (pH, ionic strength) the polymer can either stretch or coil. Second limiting situation occurs where there is an equilibrium between the adsorbed layer and the bulk polyelectrolyte solution. In this situation the number of polyelectrolyte chains at the interface is not fixed, so that if the electrostatic repulsion is

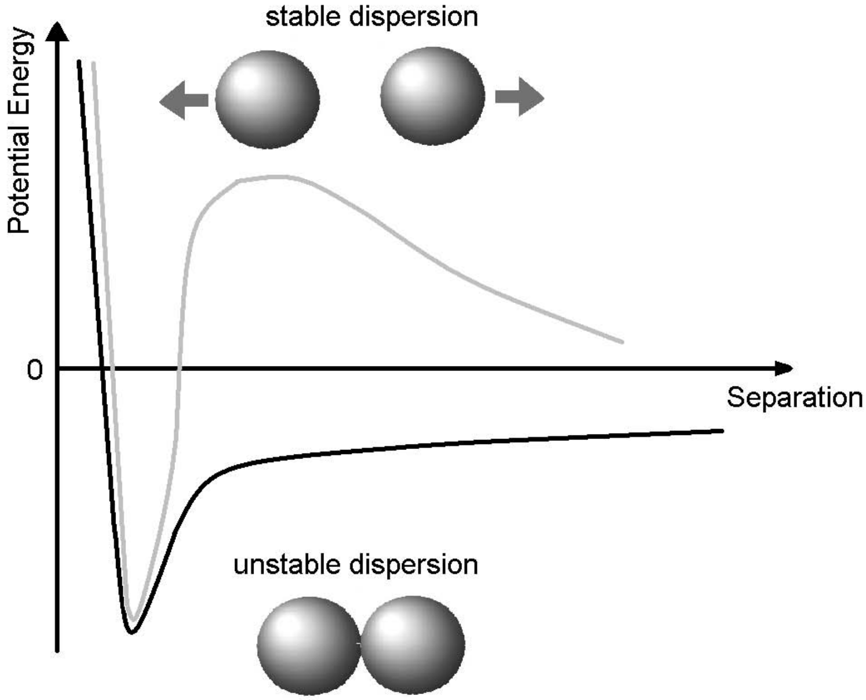

Figure 1: Potential energy as a function of separation between the surfaces of charged colloidal particles. Dispersion is stable with no salt added (grey line), but at high salt concentration (black line) aggregation occurs.

changed, the polyelectrolyte can respond by desorption or adsorption.

Adsorption and conformation of the polyelectrolyte in solution are governed mainly by electrostatic effects [7]. Surface conformation of the polyelectrolyte depends strongly on salt concentration. Some parts of polyelectrolyte chain can have many contacts with the surface (trains), other parts are bound more loosely (loops) or protrude into solution (tails). A typical configuration of an adsorbed polymer chain is illustrated in fig. 2.

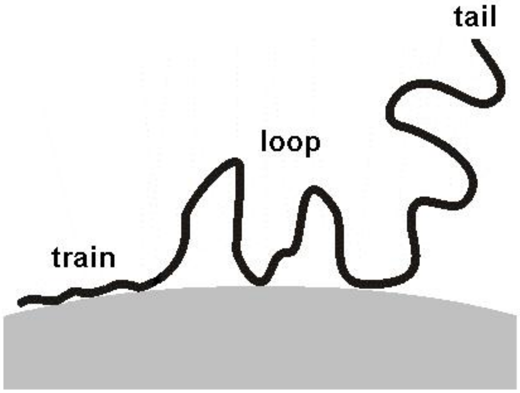

Figure 2: Conformations of adsorbed polyelectrolyte.

Polyelectrolytes adsorb strongly to interfaces due to large number of bonds, which they may form with a surface. A molecule in solution will adsorb to a surface provided that the adsorption energy is substantially larger than $k_B T$, where k_B is Boltzmann constant and T is the absolute temperature [7]. Upon adsorption, the polyelectrolyte looses both translational and configurational entropy. Once it adsorbs, it desorbs extremely slowly. In this thesis, we will mainly focus on adsorption of charged polymers at oppositely charged surfaces, where the binding is enhanced with electrostatic forces. In such systems, the adsorption is practically irreversible.

Many factors influencing the adsorption of polyelectrolytes to an oppositely charged surface can be divided into three main groups: surface, polyelectrolyte properties and properties of solvent. Concerning the surface features, the most important is the electrochemical character of surface groups (weak or strong electrolytes) and surface charge density. Regarding the properties of polyelectrolyte, we need to consider charge density, molecular mass, polydispersity, chemical and molecular structure, electrochemical character of ionizable groups, interactions between polymer segments themselves and the chain stiffness, as well as type of substrate-polymer interactions. Solvent parameters have major influence on the adsorption of polyelectrolytes, including solvent quality (good or bad solvent), effects of counterions, pH and concentration of background electrolyte. We will now discuss the latter in more detail. With increasing of concentration of a monovalent salt the adsorption of polyelectrolyte can either increase or decrease. Increase occurs if the repulsion between segments dominates the adsorption so that the screening of the repulsion at high electrolyte concentration causes the polyelectrolyte to behave partially as an uncharged polymer. Decrease of adsorption with increasing salt concentration appears if the interactions are purely electrostatic, due to the electrolyte screening both the segment-segment repulsion and the segment-surface attraction [8]. However, the screening effect is almost eliminated when a small non-electrostatic interaction is introduced. The scaling theory by Dobrynin et al. [9] predicts that the adsorption will first increase at low ionic strength before decreasing at high ionic strength.

1.2 Methods

In this section, we will give a brief overview of basic principles of methods used in this thesis.

Particle characterization

Particles used in this work were imaged by transmission electron microscopy (TEM). The TEM technique operates on the same basic principles as a light microscope, but uses electrons instead of light. The short wavelength enables to observe morphology of objects, which are smaller than the wavelength of light. Since high vacuum is required, sample has to be prepared in a dry state. A thin beam of electrons scans through a plate onto which the sample was deposited. Depending on the density of the material present, some of the electrons are scattered and disappear from the beam. Unscattered electrons hit a fluorescent screen, which gives rise to a shadow image of the sample. Analysis of TEM micrographs then yields important information on particle morphology.

Potentiometric titration

Surface charge density of colloidal particles can be accessed with potentiometric acid-base titration. Electrostatic potential between reference (Ag|AgCl) and indication (glass) electrode is proportional to the concentration of free H_3O^+ ions in solution. The latter quantity is in turn related to the amount of titratable sites on particle surface.

Scheme of our home-built precise automatic titrator [10] is depicted in fig. 3. The four burette setup allows us to perform titration experiments at constant ionic strength by additions of salt or water. Prior to sample titration, the setup is calibrated by performing a blank titration, that is a titration of strong acid with a strong base [11]. From a non–linear fit to the blank curve, following parameters can be derived: sensitivity of electrodes, concentration of base, mean activity coefficient of H_3O^+ and OH^- ions and pK of water. Another useful information can be retrieved from fitting residuals, i.e. from a difference between fitted blank curve and the experimental one. In the latter dependence, characteristic peaks for carbonates can be identified. The peak height allows us to assess the quality of the burette solutions in terms of contamination with dissolved CO_2. Resulting charging characteristics as a function of pH is then derived from a difference between sample and blank titration.

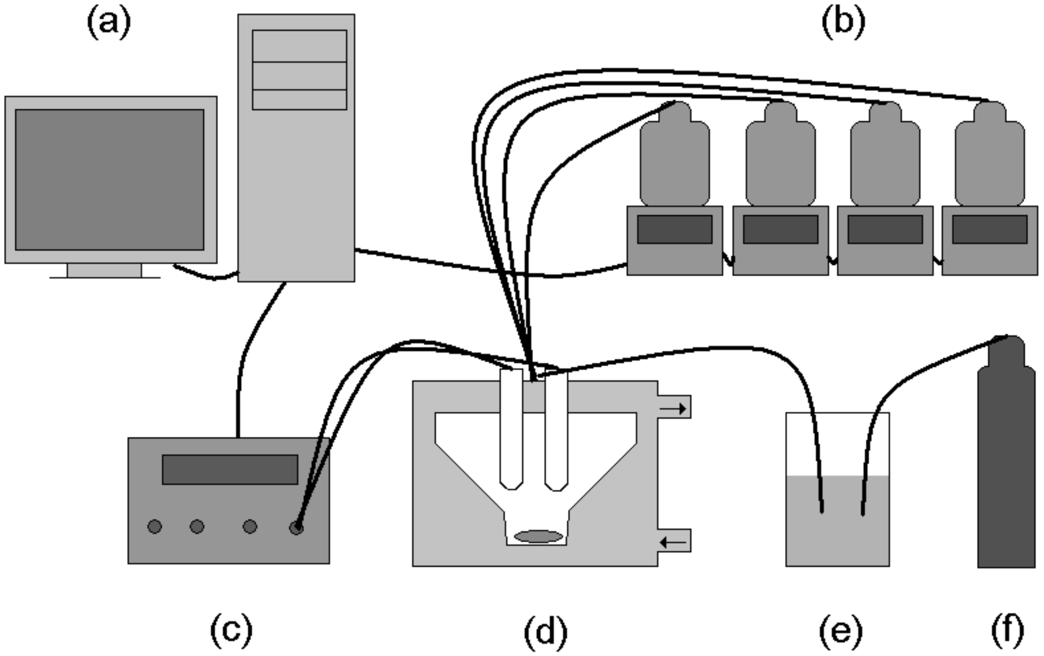

Figure 3: Scheme of titrator setup: personal computer (a) drives automatic burettes (b) and reads potential between pair of electrodes connected to high-impedance voltmeter (c). Titration experiment is conducted in a thermostated cell (d), which is continually flushed with nitrogen (f). Washing solutions (e) saturate the nitrogen with water vapour and remove residual CO_2.

Electrophoretic mobility

When an electric field $\vec{E}$ is applied to a colloidal suspension, charged particles will start to move with velocity

$$\vec{v} = u\vec{E}, \tag{1}$$

where the factor u is defined as electrophoretic mobility [7]. Electrophoretic mobility provides valuable information on particle properties, since it is related to particle surface charge and with the potential at a distance from the particle surface, where the particle counterions are no longer dragged along with a moving particle. The latter quantity is known as the ζ–potential.

The velocity of moving particles $\vec{v}$ can be measured directly with light microscope only if the particles are sufficiently big. For smaller particles (diameter < 500 nm), laser Doppler velocimetry can be used instead (fig. 4). This technique takes the advantage of the fact that light scattered from a moving particle experiences a frequency shift. The latter can be determined by optical mixing technique. Mutually coherent laser beams are arranged to cross in the electrophoretic cell, where the particles are moving due to the applied electric field. Light scattered by moving particles is then detected by looking along one of the beams; this is the so–called heterodyne experiment.

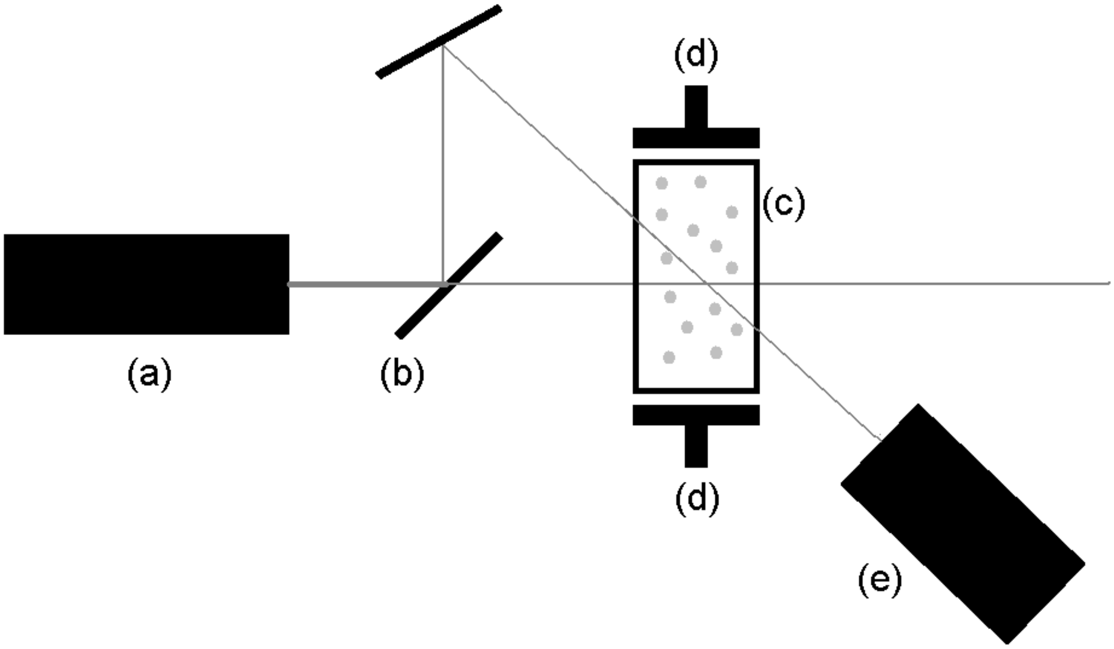

Figure 4: Scheme of laser Doppler velocimetry setup: Laser source (a) provides beam, which is splitted on mirror (b) into two mutually coherent parts. The beams are arranged to cross in electrophoretic cell (c), filled with the investigated suspension. Electric field is applied across the cell with electrodes (d). One of the beams is analyzed by detector (e).

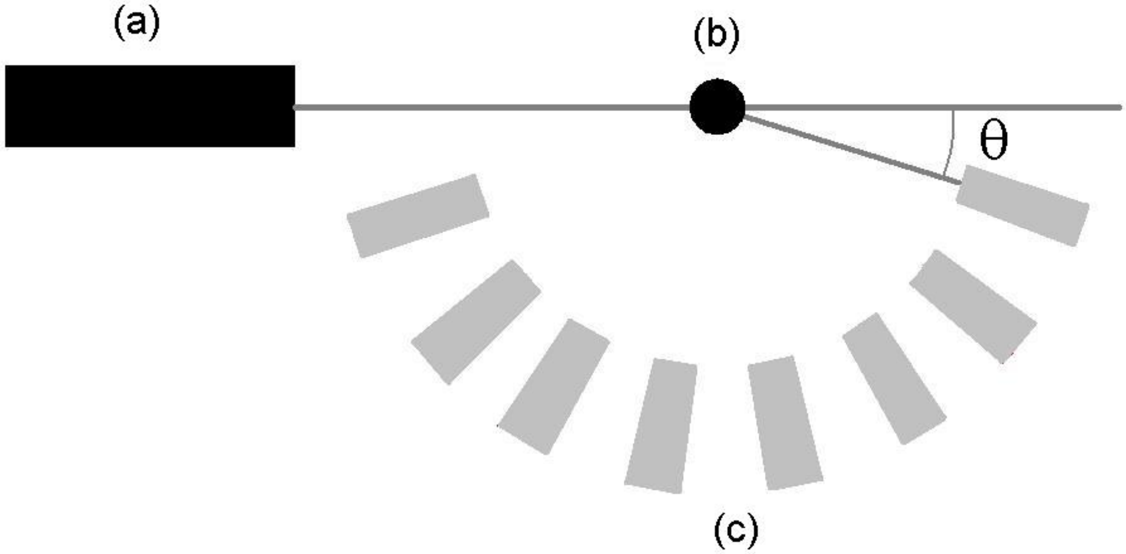

Figure 5: Scheme of a light scattering setup. Incident beam from laser source (a) impinges on sample (b). Intensity of scattered light is recorded by one or more detectors (c), in the case of DLS or SLS, respectively.

Light scattering

Light scattering is nowadays one of the most important techniques for determination particle size of colloidal dispersions [12]. Unlike majority of other scattering techniques, the source of radiation for light scattering is easily available on a daily basis, measurements are non-invasive and take typically few minutes. Modern setups can access wide range of particle size and one setup can be usually employed for both the dynamic and static light scattering (fig. 5). In the following, we will describe the basic principles of the two light scattering techniques.

Dynamic light scattering (DLS), also known as photon correlation spectroscopy (PCS) or quasi elastic light scattering (QELS), uses temporal fluctuations of light scattered by a colloidal dispersion to determine particle size.

The time-dependent fluctuations of the scattered light intensity arise from the fact that dispersed particles undergo Brownian motion. Distance between particles are constantly varying, and the motion of particles can be followed due to constructive and destructive interferences of light scattered by neighbouring particles within the illuminated zone. Scattered light is recorded by one of the detectors positioned at angle θ with respect to the incident beam (fig. 5). Analysis of the temporal fluctuation of the scattered intensity yields the diffusion coefficient of the particles; details can be found elsewhere [13]. Knowing the viscosity of solvent, hydrodynamic radius of the particles can be calculated with Stokes-Einstein relation

$$D = \frac{k_B T}{6\pi\eta r_h} \tag{2}$$

where k_B is the Boltzmann constant, T the absolute temperature, η the dynamic viscosity of solvent and r_h the hydrodynamic radius of particles. In the case of spherical shape, the latter is equal to the particle radius.

Static light scattering (SLS) is a classical light scattering technique, based on the fact that angular dependence of the scattered light contains information about the size and shape of scattering centers. A modern setup (fig. 5) is equipped with a field of detectors, capable to record intensity of scattered light at multiple angles at the same time. Particle size can be obtained by fitting an appropriate function to the angular dependence of scattered intensity.

Simultaneous static and dynamic light scattering (SSDLS) combines the two aforementioned techniques and is typically used to determine absolute rates.

Small angle neutron scattering

Small angle neutron scattering (SANS) is a technique very well suited for investigation of soft matter. The basic principle is similar to the light scattering. Some of the neutrons directed at a sample are elastically scattered by atomic nuclei. The contrast in neutron scattering measurements comes from different scattering length density, which is a measure of the strength of the interaction of a neutron wave with a given nucleus. Scattered neutrons at small angles are recorded at a detector. Particle size, polydispersity and other properties can be derived by fitting of the profile of scattered intensity as a function of scattering angle with an appropriate function.

The advantage of substantial difference between scattering length density of hydrogen and deuterium can be used to measure structure of polyelectrolyte layers on colloidal particles. In the latter experiment, known as the contrast matching, by tuning the ratio of H_2O and D_2O in solvent, it is possible to set the same scattering length for particles and dispersing medium. In this case the particles do not scatter and the layer alone can be observed.

2 Aggregation and charging of Stöber-type silica[1]

2.1 Introduction

Aggregation and charging behavior of colloidal particles have major influence on suspension stability. In this chapter, we will focus on stability of silica particles in the presence of a simple 1:1 electrolyte.

The colloidal stability of silica suspensions is known to contradict the famous theory of Derjaguin, Landau, Verwey, and Overbeek (DLVO). This classical theory predicts that colloidal particles aggregate rapidly at sufficiently high salt levels and/or when the particles are weakly charged [15–19]. However, silica particles have been reported to be stable at high salt levels and at low pH, where silica bears little charge [20–26]. Moreover, other silica systems show a minimum in the stability plot [27, 28] or in the critical coagulation concentration, which separates the regions of slow and fast aggregation [21, 23, 24]. These anomalies have been typically reported for nanometer sized silica particles, but also for submicrometer sized particles, and they are in sharp contrast to predictions of DLVO theory. One relevant factor determining colloidal stability of silica is certainly the particle size [22, 25, 26], but other factors influencing the surface morphology must be important as well. Sub-micrometer sized silica has been sometimes reported to behave similarly to DLVO theory [23, 28–31], whereby silica produced with the method of Stöber et al. [32] always appears to fall into this class [13,14,16]. This fact may appear surprising, as Stöber particles have been found to be porous based on potentiometric titration experiments [33, 34]. These studies reported that Stöber silica has an extremely high charge density in the presence of small alkali metal counterions, which can penetrate the micropores. The charge density decreases substantially in the presence of large tetraalky-

---

[1] This chapter resulted in the following publication: Kobayashi, M.; Skarba, M.; Galletto, P.; Čakara, D.; Borkovec, M. *J. Colloid Interface Sci.*, **2005**, *292*, 139.

lammonium counterions, which cannot enter the micropores [33]. Heating the particles at 800°C has a similar effect, which has been interpreted to originate from the shrinkage of the micropores [34]. On the other hand, no unusual features have been reported in the electrokinetic behavior of Stöber silica [33,35].

Our work aims to clarify the effect of heat treatment on the charging behavior on Stöber-type silica particles, and to relate these findings to the colloidal stability of these systems. Interestingly, the stability of the heated particles turns out to be in quantitative agreement with DLVO theory. This important finding demonstrates that stability of colloidal silica does not follow a unique pattern, but that it may vary widely depending on the silica type.

2.2 Materials and methods

Silica particles

In our work we used four different batches of colloidal silica particles. Two of them, referred as KEP10 and KEP30, were kindly provided by the manufacturer (Nippon Shokubai, Japan). The particles were synthesized similarly to the Stöber procedure. The KEP10 and KEP30 particles were washed with 0.1 M HCl three times and then with Milli-Q water (Milli-Q A10 UV/UF, Millipore) by repeated centrifugation and decantation until the electrical conductivity of supernatant decreased below 2 μS/cm.

Two additional batches, referred as KEP30H and KEP10H, were prepared by heating the silica powders KEP10 and KEP30 in a covered quartz crucible at 800°C for 24 h. After the heat treatment, the particles remained flowing powder. The heated particles were used without further purification. The heated particles were not left dispersed in water more than a week.

Particle characterization

Micrographs of particles were obtained by transmission electron microscopy setup TEM Philips EM410. Analysis of micrographs yielded particle morphology and the size distribution. The number average radius $\langle r \rangle$ and coefficient of variation $\mathrm{CV} = (\langle r^2 \rangle / \langle r \rangle^2 - 1)^{1/2}$ were evaluated by measuring 100–300 particles from the micrographs. The angular brackets denote number-weighted averages. Particle size was also measured on a multi-angle goniometer (ALV CGS-8, Langen) equipped with eight fiber optic detectors and a 532 nm solid-state laser as light source. Dynamic light scattering (DLS) was performed in dilute suspensions (1–10) mg/L in 0.1 mM KCl at pH around 8 at a scattering angle of 90°. From the second order cumulant fit, the hydrodynamic radius, r_h, was evaluated and was compared with the TEM data using the relationship $r_h = \langle r^6 \rangle / \langle r^5 \rangle$. The Schultz distribution was assumed to estimate the higher moments. Static light scattering (SLS) was used to extract an apparent radius, r_s, by fitting the angle dependence to the Rayleigh–Debye–Gans (RDG) theory [36]. This value can be compared with the TEM data by using the relation $r_s^2 = \langle r^8 \rangle / \langle r^6 \rangle$. The density of the particles, ρ, was measured in aqueous suspensions by pycnometry. The specific surface area of the silica particles, a, was determined with nitrogen gas adsorption (BET) measurements performed with a Gemini 2375 (Micromeritics, USA), and based on the relation $a = (3/\rho)\langle r^2 \rangle / \langle r^3 \rangle$ compared with TEM [18].

Potentiometric titration

Sample titration is performed at similar conditions as the blank (cf. section 1.2). Difference between sample and blank curves yields molar amount of charge on particles. Knowing the sample mass and specific surface of particles determined by gas adsorption, the molar amount can be converted to the surface charge density. Further details on such titration techniques are given elsewhere [38, 39].

Burette solutions contained 0.25 M HCl, 0.25 M KOH, 3.0 M KCl, and pure water. Solution of acid and base were prepared from analytical concentrates (Titrisol from Merck and CO_2-free concentrate from Mallinckrodt Baker, respectively). Analytical grade solid KCl was provided by Acros Organics (Geel, Belgium). All solutions were prepared from CO_2-free boiled Milli-Q water. Separated glass and Ag|AgCl reference electrodes were purchased from Metrohm (Herisau, Switzerland), with ordering numbers 6.0123.100 and 6.0733.100, respectively.

Acidified silica suspensions of concentrations in the range 8.65 g/L were first titrated with KOH, and then back-titrated with HCl, maintaining a constant ionic strength and a temperature of 25°C. The electrode readings were recorded after the drift criterion of 1 mV/min was satisfied. Each forward and backward titration run was repeated three times, and the overall ionic strength of the sample was increased by addition of KCl solution to start the next series of runs. Titrations of silica particles were conducted at pH below 9 to minimize the effect of silica dissolution [37].

Electrophoretic mobility

A laser Doppler velocimetry setup (Zeta Sizer 2000, Malvern) was used to measure the electrophoretic mobility of the particles as a function of pH in solutions of different KCl concentrations [17,18]. Prior to each measurement, silica suspension, KCl solution, and HCl or KOH were mixed with water, and the mixture was injected into the measurement cell. The pH of suspension was measured with a combination electrode 6.0234.110 from Metrohm (Herisau, Switzerland). The concentrations of silica particles were around 40 mg/L. The temperature of electrophoresis cell was maintained at 25°C.

Absolute aggregation rates with light scattering

Early-stage particle aggregation was monitored with time-resolved light scattering performed on a multi-angle goniometer with eight optical detectors (ALV CGS-8, Langen) in two ways. Most experiments were carried out with

DLS with one detector positioned at 90°. Simultaneous static and dynamic light scattering (SSDLS) measurements were also performed for fast aggregation conditions [40, 41].

Quartz and borosilicate glass cuvettes were cleaned with hot 3:1 mixture of concentrated sulphuric acid and hydrogen peroxide and by extensively rinsing with Milli-Q water. Prescribed amounts of HCl or KOH, KCl solution, and water were mixed in the cuvette, and stable silica suspension was added. The cuvette was sealed and quickly shaken with a vortex mixer, and immediately monitored with a time resolution of 20 s for (10–60) minutes at a temperature of 25°C (see Fig. 6). The suspension pH was measured with a combination electrode 6.0234.110, (Metrohm, Herisau, Switzerland) in the cuvette after the measurement. A typical result of a time resolved DLS experiment is shown in fig. 6. The initial particle number concentration N_0 was chosen in the range 3×10^{14} m^{-3} – 7×10^{15} m^{-3} (0.8 mg/L – 220 mg/L). This value is sufficiently low to ensure that the initial increase of the light scattering signals corresponds to the formation of dimers in the early stages of the aggregation. This point was asserted such that the relative increase of the hydrodynamic radius did not exceed 20% in the region used for estimation of the rate constant, and that the radius extrapolated towards the initial time agrees with the radius in the stable suspension within 5%. An equivalent way to ensure that the aggregation remains in its early-stage is to show that the half-time of the aggregation $T_{1/2} = 2/(kN_0)$ is larger than or at least comparable to the experimental window [40]. This condition is satisfied as $T_{1/2}$ is in the range of (20–60) minutes.

Aggregation rate constants were obtained from the initial slope of the record of the hydrodynamic radius $r_h(q,t)$ as a function of time t. This quantity also depends on the magnitude of the scattering vector

$$q = \frac{4\pi}{\lambda}\sin(\theta/2) \tag{3}$$

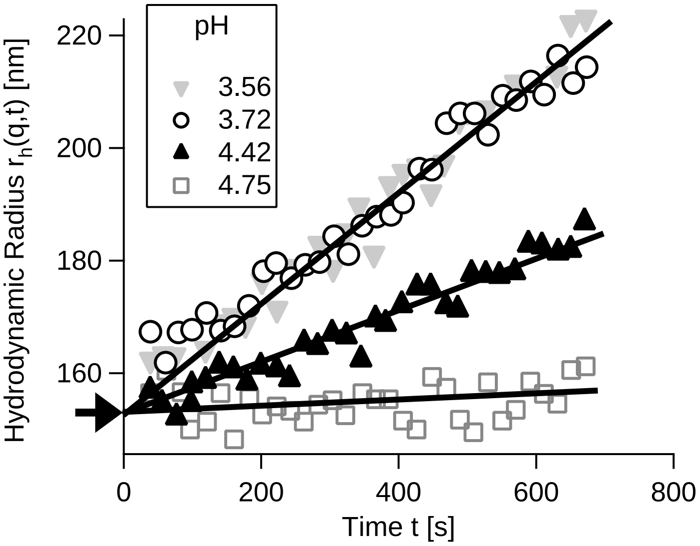

Figure 6: Determination of aggregation rate constants by time-resolved light scattering. Record of the apparent hydrodynamic radius a function of time for heated KEP30H particles at 10 mM and different pH originating from the radius of the stable suspension (arrow). From the slope, the rate constant is obtained (solid line).

where λ is the wavelength of the light in the scattering medium and θ is the scattering angle. The resulting apparent DLS rate can be expressed in terms of the aggregation rate constant k by applying the Rayleigh–Debye–Gans (RDG) approximation, which leads to the relation [40, 41]

$$\frac{1}{r_h(q,0)}\frac{dr_h(q,t)}{dt}\bigg|_{t\to 0} = \left[1+\frac{\sin(2rq)}{2rq}\right]\left(1-\frac{1}{\alpha}\right)kN_0 \tag{4}$$

where r = $\langle r \rangle$ is the number averaged particle radius and α is the relative hydrodynamic radius of the doublet. The hydrodynamic radius of the doublet can be estimated as $\alpha \simeq 1.39$ at low Reynolds numbers. Equation 4 is reliable for sufficiently small particles, typically below 200 nm in diameter [40–42].

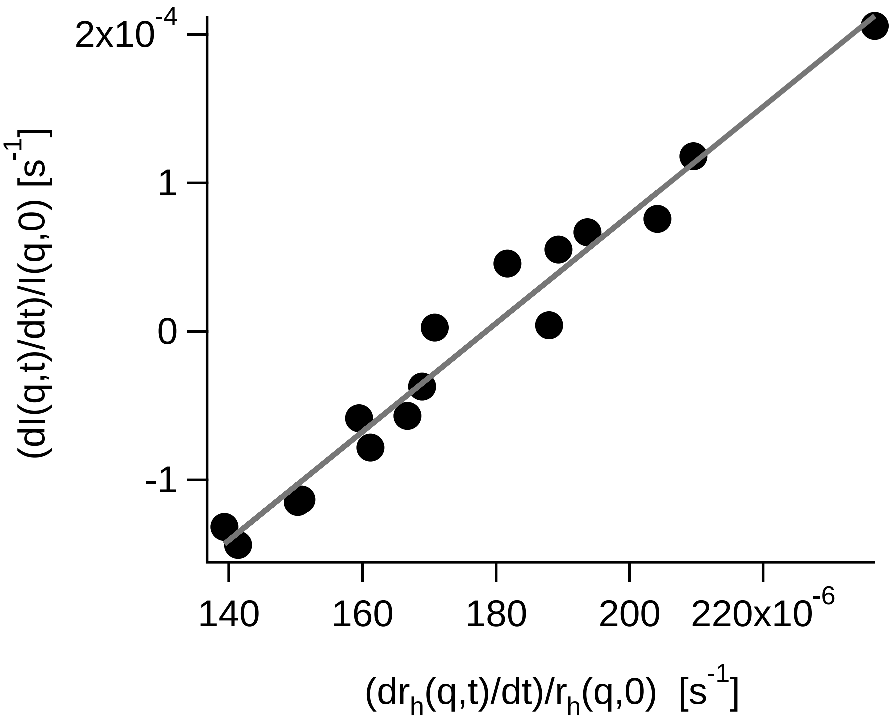

Figure 7: Scatter plot of the apparent static and dynamic aggregation rates obtained from an SSDLS experiment for KEP10 at pH 10 and 1 M. The data are fitted to a straight line, whose intercept gives the absolute aggregation rate constant.

Fast aggregation conditions were obtained in 1 M KCl and pH 6-11, and the corresponding results are summarized in Table 1. For the larger particles, the SSDLS measurements were carried out to compare with the absolute fast rate constants obtained with DLS. In this case, the rate constants can be evaluated without any assumptions concerning unknown optical or hydrodynamic properties of the doublets by plotting the apparent rate constant obtained from SLS as a function of the one obtained from DLS. The data were fitted to a straight line according to the relation [41]

$$\frac{1}{I(q,0)}\frac{dI(q,t)}{dt}\bigg|_{t\to 0} = \frac{1}{r_h(q,0)}\frac{dr_h(q,t)}{dt}\bigg|_{t\to 0}\left(\frac{\alpha}{\alpha-1}\right) - kN_0 \tag{5}$$

Table 1: Fast aggregation rate constants of the silica particles

Particles	$k_{fast}(\times 10^{-18}$ m^3/s)		
	DLS[a]	SSDLS[b]	DLVO[c]
KEP10	1.9	-	8.4
KEP10H	1.4	-	8.4
KEP30	2.7	2.4	8.4
KEP30H	2.9	3.2	8.4

[a] Obtained from time-resolved measurement with dynamic light scattering (DLS).
[b] Obtained from simultaneous static and dynamic light scattering (SSDLS).
[c] Obtained from DLVO theory with the Hamaker constant $A = 8.3 \times 10^{-21}$ J.

where $I(q,t)$ is the time-dependent scattering intensity. Fig. 7 shows typical experimental data and their fit to eq. 5. The resulting relative hydrodynamic radii of the doublets α were in close agreement with the theoretical value stated above. The results of the fast rate constants are summarized in table 1. We further report the rate constants in terms of the customary stability ratios defined as

$$W = \frac{k_{fast}}{k} \tag{6}$$

where k_{fast} is the fast aggregation rate for KCl concentration above 1 M and the pH in the range 6-11. Under these conditions, the aggregation rates reach constant values characteristic for the fast aggregation regime.

2.3 Results

Particle characterization

The TEM pictures shown in fig. 8 demonstrate that the particles are monodisperse and nearly spherical. Nevertheless, the samples KEP10 and KEP10H contained some deformed particles. The number-weighted mean radii $\langle r \rangle$ and the corresponding coefficients of variation (CV) are summarized in table 2. The TEM gave particle radii around 60 nm for KEP10 and KEP10H, and around 150 nm for KEP30 and KEP30H. The CV was 0.05 ± 0.01 indicating monodisperse samples. For the larger KEP30 particles, heating induced a slight decrease in the particle size of about 6%. This effect is probably due to shrinkage of pores, but is not clearly observable for the smaller particles. Otherwise, the particle morphology was not significantly influenced by the heat treatment.

The particle densities and the surface areas measured by gas adsorption are summarized in table 2. The surface area is consistently higher than the geometrical surface areas of perfect spheres estimated from TEM data. This effect is particularly pronounced when comparing KEP30 and KEP30H. Densities determined by water pycnometry were around 2.0 g/cm^3 and 2.2 g/cm^3 for unheated and heated particles, respectively. The former values are close to reported densities of Stöber silica in the range 1.7 g/cm^3 – 2.0 g/cm^3 [33,43]. The latter value agrees with the density of nonporous amorphous silica, but is lower than the one of quartz of 2.6 g/cm^3 [44]. The decrease of surface area and increase of the particle density upon heating can be again understood due to pore shrinkage.

Surface charge density

Markers in fig. 9 show the values of measured surface charge density of silica particles obtained by potentiometric titration. The particles carry a negative charge, and its magnitude increases with increasing pH.

The titration curves of the unheated silica samples (figs. 9a and 9b) lack reversibility at high ionic strength (i.e., hysteresis effect) and they indicate very high charge densities. This unusual behaviour has already been observed for Stöber silica, and interpreted in terms of nanometer-scale porosity of the unheated silica particles (i.e., microporosity) [33, 34]. The hysteresis effect

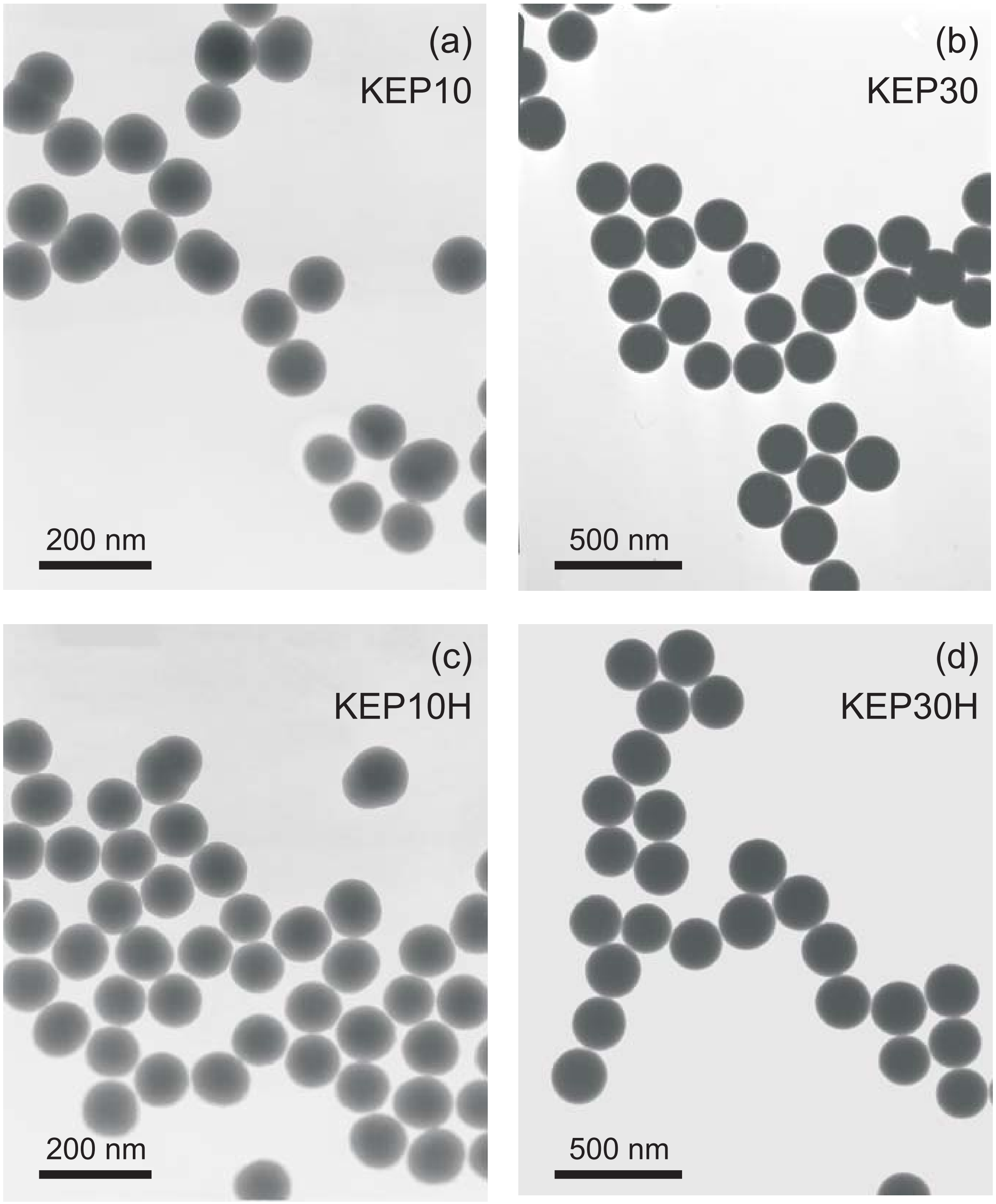

Figure 8: Transmission electron micrograph (TEM) pictures of silica particles. Unheated (a) KEP10 and (b) KEP30 are compared with heated (c) KEP10H and (d) KEP30H.

Table 2: Characteristics of the silica particles studied

Particles	$\langle r \rangle$ [nm][a]	CV [1] [b]	r_h [nm][c]		r_s [nm][d]		a [m^2/g] [e]		ρ [g/cm^3] [f]
	TEM	TEM	DLS	TEM	SLS	TEM	BET	TEM	
KEP10	58	0.06	69	59	67	59	43	24	2.13
KEP10H	57	0.05	67	58	68	58	32	24	2.19
KEP30	156	0.04	160	157	157	158	51	9.4	2.03
KEP30H	143	0.04	153	144	147	144	14	9.6	2.18

[a] Number-weighted particle radius $\langle r \rangle$ determined by transmission electron microscopy (TEM)

[b] Coefficient of variation (CV) obtained by the same method.

[c] Apparent hydrodynamic radius r_h obtained by dynamic light scattering (DLS) and calculated from TEM.

[d] Intensity-weighted radius r_s obtained by static light scattering (SLS) and calculated from TEM.

[e] Measured specific surface area by nitrogen adsorption (BET) and compared with calculated values based on TEM and particle densities.

[f] Particle density measured by water pycnometry.

at high ionic strengths is likely caused by particle porosity [33, 34], since the protons slowly diffuse into the particle interior. At lower ionic strengths, overlapping double layers close off these pores, and the titration becomes reversible. The large magnitude of the charge densities can be explained by the large internal surface of the pores, whose surface is probably covered with a hairy (gel–like) layer. This layer is penetrable to protons in solution, but impenetrable to nitrogen in the dry state.

The titration curves of the heated silica samples (Figs. 9c and 9d) are reversible and their surface charge density is much lower. The interpretation of this effect is that the micropores are closed off upon heating, and the surface areas probed by protons in solution and nitrogen in the gas phase become the same [33, 34]. The surface modification by heating seems to be reversible, however, as the surface charge of heated silica increases with

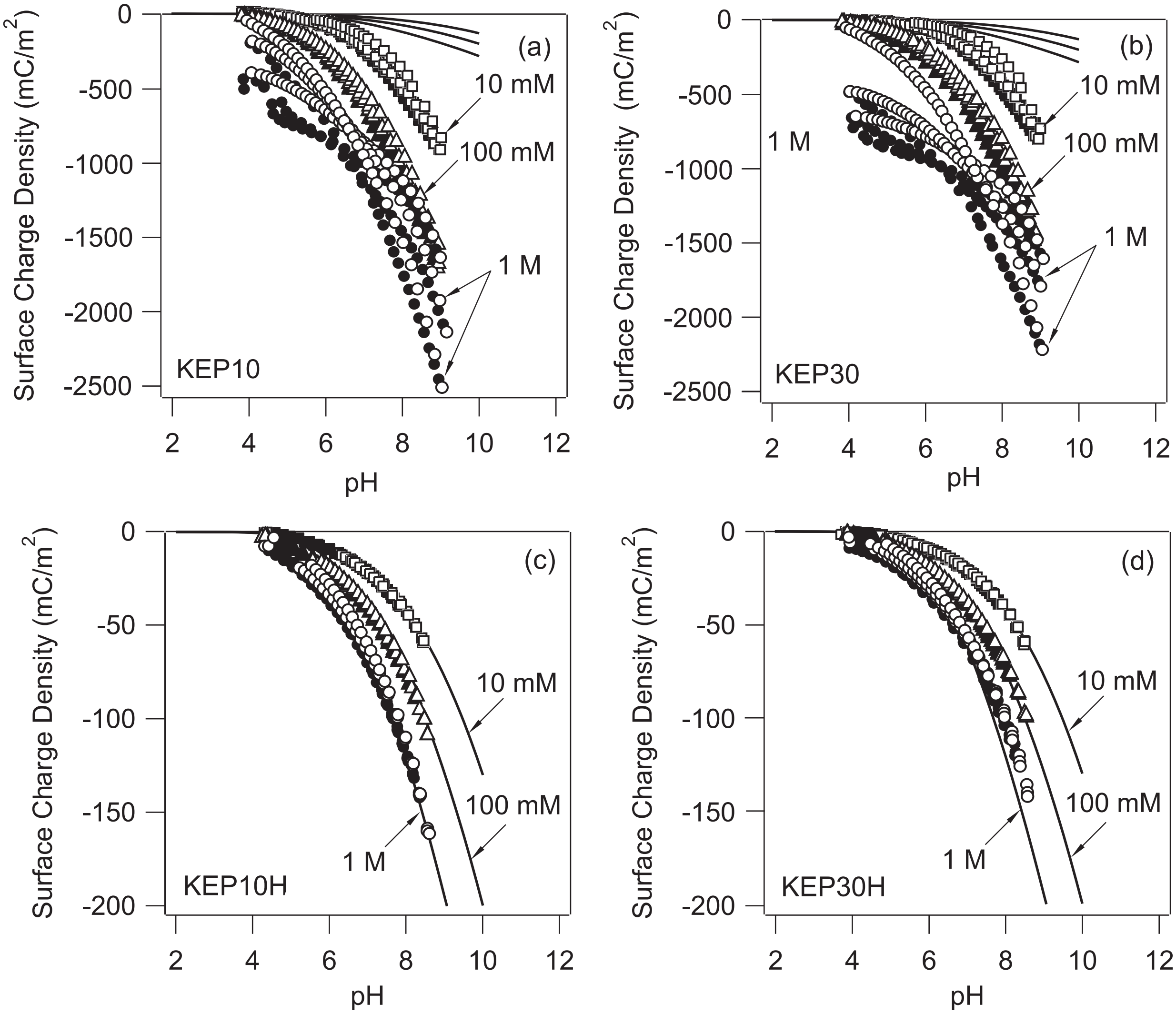

Figure 9: The surface charge density of silica particles as a function of pH at different ionic strength adjusted with KCl. Symbols denote the experimental results obtained by forward (open symbols) and backward potentiometric titrations (closed symbols). The solid lines were calculated with the 1–pK basic Stern model with the parameters pK = 7.5, $C_S = 2.9$ F/m^2, and $\Gamma_0 = 8$ nm^{-2} [51]. Unheated (a) KEP10 and (b) KEP30 are compared with heated (c) KEP10H and (d) KEP30H

.

increasing contact time with water [34].

Electrophoretic mobility

The measured electrophoretic mobilities are plotted as markers in fig. 10. The particles exhibit negative mobility, and the magnitude of the mobility increases with increasing pH as expected from the surface charge. In spite of the fact that unheated silica samples are more strongly charged than the heated ones, the mobilities remain similar for both samples. Therefore, the chargeable sites within the pores in the interior of the particles do not substantially contribute the electrophoresis. Previous investigators have drawn similar conclusions [33, 35].

Colloidal stability

Fig. 11 summarizes the stability ratios as a function of the solution pH. One observes that all silica samples exhibit similar aggregation behavior. Fast aggregation conditions are encountered in KCl concentration above 1 M and pH in the range 6–11. Fast aggregation rate constants are summarized in table 1, and their values are around $(2.0 \pm 0.6) \times 10^{-18}$ m^3/s. Comparable values were observed for silica by others [22, 31].

Colloidal silica has been often reported to be anomalous, and in qualitative disaccord with DLVO theory [20, 22, 23, 26]. However, the results presented here are definitely in line with DLVO theory. At high ionic strength, the aggregation is always fast and pH independent. The stability ratios increase with decreasing ionic strength due to decreased screening, and they decrease with decreasing magnitude of particle charge due to diminishing electrostatic repulsion. In section 2.4, we show that the present stability data are even in quantitative accord with DLVO theory.

An anomalous non–DLVO feature in silica aggregation is its high stability at high ionic strength and at low pH [20,22,23,26]. While this feature was not observed for the present samples in a pronounced fashion, their stability is

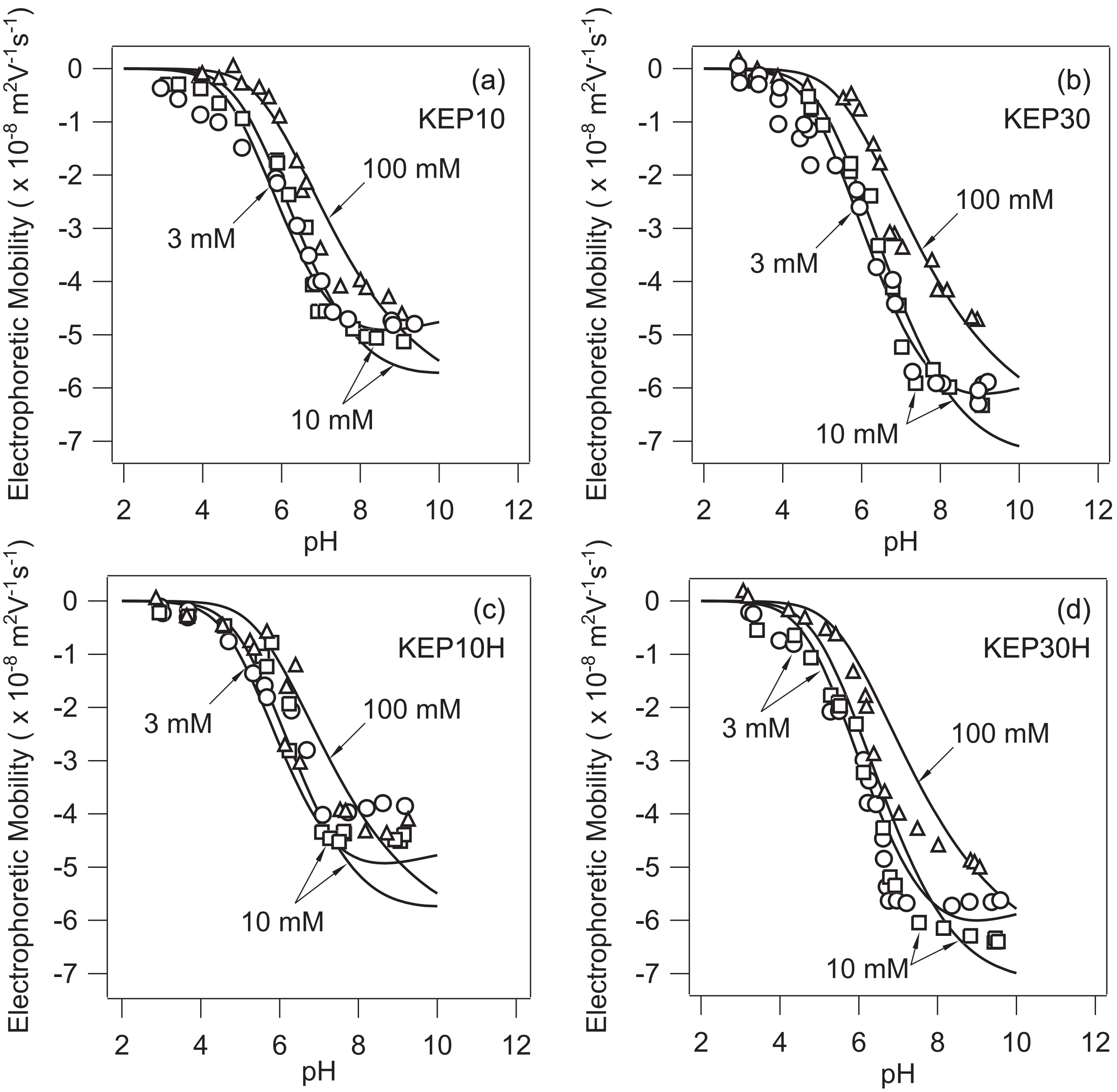

Figure 10: The electrophoretic mobility of silica particles as a function of pH at different ionic strength adjusted with KCl. Symbols denote the experimental results. The solid lines were calculated with the standard electrokinetic model with a fixed distance of the plane of shear of $d = 0.25$ nm and the 1–pK basic Stern model with the parameters p$K = 7.5$, $C_S = 2.9$ F/m^2, and $\Gamma_0 = 8$ nm^{-2} [51]. Unheated (a) KEP10 and (b) KEP30 are compared with heated (c) KEP10H and (d) KEP30H.

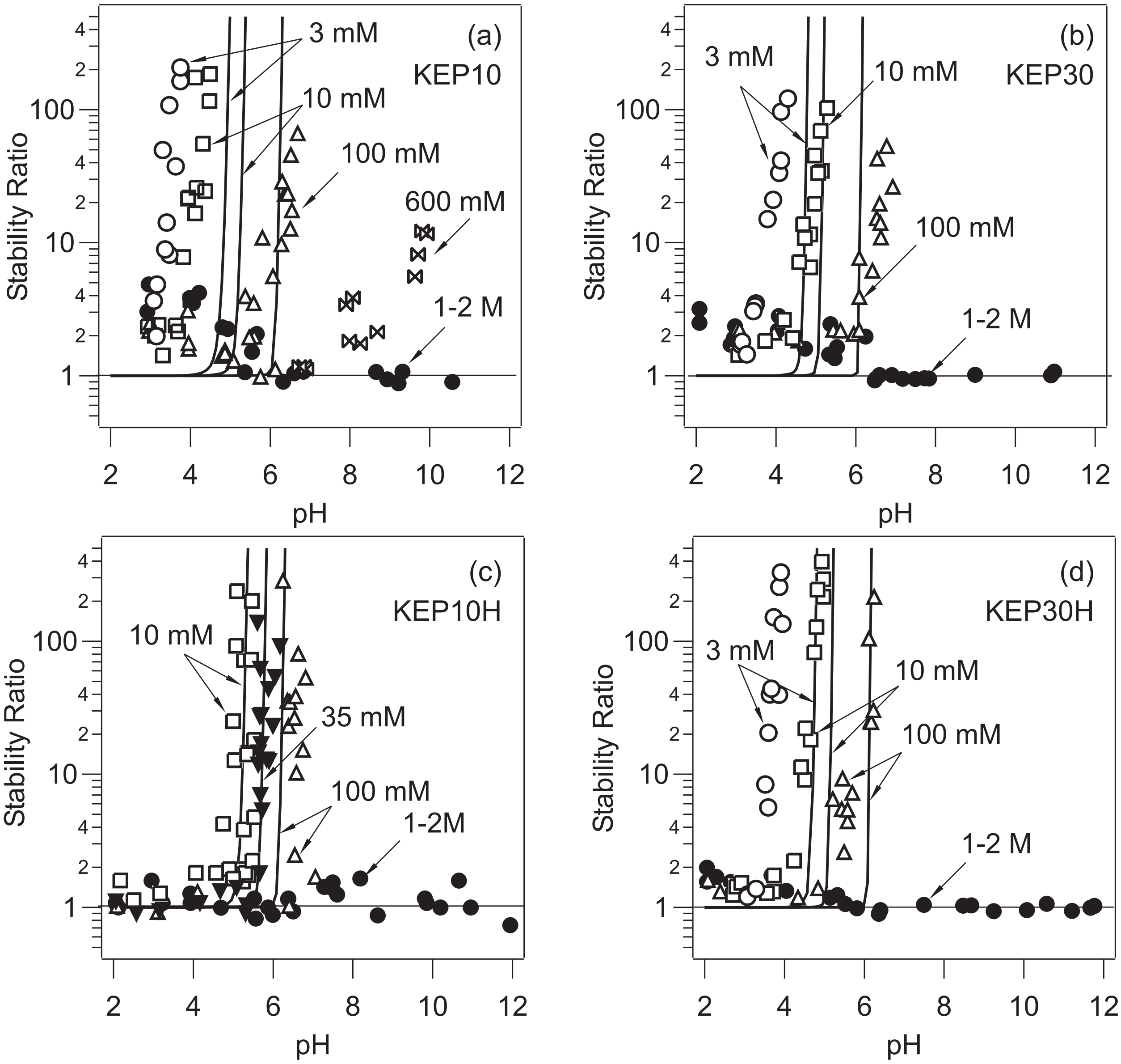

Figure 11: Stability ratios of silica particles as a function of pH at different ionic strength adjusted with KCl. Symbols denote the experimental results obtained by time-resolved dynamic light scattering. The solid lines were calculated with the classical DLVO theory. The electrostatic interactions are based on nonlinear Poisson–Boltzmann equation and they include full charge regulation based on the 1–pK basic Stern model with the parameters pK = 7.5, $C_S = 2.9$ F/m^2, and $\Gamma_0 = 8$ nm^{-2} [51]. The van der Waals interaction uses a Hamaker constant of $A = 8.3 \times 10^{-21}$ J. Unheated (a) KEP10 and (b) KEP30 are compared with heated (c) KEP10H and (d) KEP30H.

somewhat increased below pH 6. This trend can be clearly established for the unheated samples (KEP10 and KEP30). Similar trends were reported earlier [26, 31]. The increase of stability at low pH can be ascribed to an additional repulsive force, which probably originates from a steric repulsion induced by hairy (or gel–like) surface layer consisting of polysilicic acid chains protruding from the surface into the solution [26, 45–48]. Existence of such a layer has been suggested on the basis of direct force measurements [46–48] and from a relatively high value of the Stern capacitance [49]. For the heated samples, the stability at low pH is unaffected for KEP10H, or increases only slightly for KEP30H. This difference between the heated and unheated samples is probably due to dehydration of the hairy layer. This trend is in line with the observations of increased stability of colloidal silica after extensive storage period [27]. Aging of silica in water probably promotes the growth of the hairy layer and amplifies the anomalous features of colloidal stability of silica.

2.4 Modelling and discussion

Surface charge density

The 1–pK basic Stern model is used to describe the surface charge density of silica. This model has been shown to rationalize the charging behaviour of various oxides [50, 51], and suggests that the charge of silica originates from the deprotonation of silanol groups on the surface, according to

$$\mathrm{SiOH} \leftrightarrow \mathrm{SiO^-} + \mathrm{H^+} \tag{7}$$

The mass action law for the reaction equilibrium relates the site densities of Γ_{SiOH} and Γ_{SiO^-} as

$$\frac{a_H \Gamma_{\mathrm{SiO^-}}}{\Gamma_{\mathrm{SiOH}}} = K \exp(e\beta\psi_0), \tag{8}$$

where a_H is the activity of the protons, K the intrinsic equilibrium constant, e the elementary charge, β the inverse thermal energy, and ψ_0 the surface potential. Customarily, one expresses some of these quantities as pH = -log a_H, pK = -log K and $k_BT = 1/\beta$, where k_B is the Boltzmann constant and T the absolute temperature. Since the number of surface sites is constant, the total number density of chargeable sites is

$$\Gamma_0 = \Gamma_{\mathrm{SiOH}} + \Gamma_{\mathrm{SiO^-}} \tag{9}$$

The surface charge originates from the negatively charged groups, and its density is therefore given by

$$\sigma = -e\Gamma_{\mathrm{SiO^-}}. \tag{10}$$

The surface charge density is further proportional to the potential drop across the Stern layer, namely

$$\sigma = C_S(\psi_0 - \psi_d), \tag{11}$$

where C_S is the Stern capacitance and ψ_d is the diffuse layer potential. The surface charge density can be finally related to the diffuse layer potential through the Grahame equation

$$\sigma = \frac{2\varepsilon\varepsilon_0\kappa}{\beta e}\sinh\left(\frac{\beta e\psi_d}{2}\right), \tag{12}$$

where $\varepsilon\varepsilon_0$ is the total permittivity of water, and the Debye length is given by

$$\kappa^{-1} = \sqrt{\frac{\varepsilon\varepsilon_0}{2N_A\beta e^2 I}} \tag{13}$$

where N_A is the Avogadro number and I is the ionic strength of the solution. Equations 8-13 define the basic Stern model for silica, and can be solved numerically.

The results of the calculations based on the present Stern model are shown as lines in Fig. 9. The model parameters were not fitted, but we have used the values p$K = 7.5$, $C_S = 2.9$ F/m^2, and $\Gamma_0 = 8$ nm^{-2} proposed by Hiemstra et al. [51]. In spite of the fact that there are no adjustable parameters, the model describes the charging of heated silicas very well. On the other hand, it is incompatible with the high charge densities and hysteresis effects observed for the unheated silica. As argued above, the unheated silicas are microporous, and their surface area is underestimated by the gas adsorption measurement.

Electrophoretic mobility

The standard electrokinetic model proposed by O'Brien and White [52] was used to interpret the electrophoretic mobility of the silica particles. The important input parameter is the surface potential at the shear plane, which is denoted as the ζ potential. The shear plane is assumed to lie at a distance d away from the surface, and is estimated from the potential profile of the diffuse layer as [53]

$$\zeta = \frac{4}{\beta e}\text{arctanh}\left[\tanh\left(\frac{\beta e\psi_d}{4}\right)\exp(-\kappa d)\right]. \tag{14}$$

The diffuse layer potential is calculated using the 1–pK Stern model with the same parameters as discussed above.

The solid lines in fig. 10 represent the results of calculated electrophoretic mobility assuming that the distance of slipping plane from the surface is $d = 0.25$ nm [53]. The model was found to be able to describe all the measured mobilities reasonably well, including unheated silica particles. The good agreement suggests that the surface of the heated silica particles is relatively smooth and that the basic Stern provides a consistent model of the charging behavior. For the unheated silica particles, the good agreement indicates further that the surface of the unheated particles resembles the one of the heated ones, and that the additional charges observed by potentiometry reside in the interior of the particles [33,35]

Stability ratios

The aggregation rate constant of two spherical colloidal particles is obtained by solving the steady state diffusion equation including the interactions between the particles with the result [17,18,53]

$$k = \frac{8}{3\beta\eta}\left\{2r\int_0^\infty \frac{B(h)}{(2r+h)^2}\exp[\beta V(h)]dh\right\}^{-1}, \tag{15}$$

where η is the viscosity of the solution, h is the distance between the surfaces, $B(h)$ is the hydrodynamic resistance function, and $V(h)$ is the interaction potential. The resistance function can be approximated by [54,55]

$$B(h) = \frac{6(h/r)^2 + 13(h/r) + 2}{6(h/r)^2 + 4(h/r)}. \tag{16}$$

The DLVO theory assumes that the interaction potential $V(h)$ can be approximated by the superposition of the attractive van der Waals potential $V_{vdW}(h)$ and repulsive potential due to double–layer overlap potential $V_{dl}(h)$, namely

$$V(h) = V_{vdW}(h) + V_{dl}(h). \tag{17}$$

We will evaluate this potential within the Derjaguin approximation. The van der Waals potential is thus given by

$$V_{vdW}(h) = -\frac{Ar}{12h}, \tag{18}$$

where A is the Hamaker constant. The double–layer overlap potential $V_{dl}(h)$ is calculated numerically from the Poisson–Boltzmann equation between two charged plates including full charge regulation [56, 57]. The stability ratio is obtained from eq. 6 by realizing that the fast rate constant can be obtained by considering the van der Waals interactions only.

The theoretical results of the stability ratios with the DLVO theory are shown as lines in fig. 11. The calculations employ the parameters used to describe the potentiometric titration data, namely the parameter values pK = 7.5, C_S = 2.9 F/m^2, and Γ_0 = 8 nm^{-2} proposed by Hiemstra et al. [51]. The Hamaker constant $A = 8.3 \times 10^{-21}$ J used in the calculations corresponds to the currently accepted value for the interaction of silica across water [19].

Given the fact that there are no adjustable parameters, one observes that the stability of the Stöber silica particles can be predicted with the classical DLVO theory reasonably well. In particular, the prediction is very good for the KEP10H particles, where the theory provides the right onset of the slow aggregation and the proper pH and salt dependence. While colloidal stability of silica particles has been often suggested to be anomalous and in disagreement with DLVO theory, to our knowledge this is the first time when quantitative agreement is reported.

While the other systems studied here behave similarly to the DLVO predictions, systematic deviations are observed. In the following, we will discuss their origin, and relate them to the anomalous stability of silica observed by other authors. The most likely interpretation of these anomalies is the presence of a hairy layer consisting of polysilicic acid on the particle surface. On the other hand, the particle porosity appears to have little influence. Three main types of discrepancies between experimental stability ratios and DLVO theory predictions shown in fig. 11 can be identified, namely the onset pH of slow aggregation, the slope of the stability curves in the slow aggregation regime, and increased stability at low pH.

The first discrepancy dominates for KEP30H, and it can be reconciled neither by shifting the relative planes of origins of the double–layer force and of the van der Waals force nor by modifying the Hamaker constant [53]. The shift of the plane of origin of the double–layer force was able to explain the measured forces between silica surfaces within DLVO theory [46] and indeed displaces the calculated stability curves to lower pH. However, this displacement is very small, and cannot explain any of the observed discrepancies. Decreasing the Hamaker constant produces a qualitatively similar effect, but its value must be decreased unrealistically by about two orders of magnitude to modify the onset pH appreciably. We suspect that the shift in the onset of slow aggregation is related to repulsive forces originating from the overlap of the hairy layers.

The second discrepancy is the weaker pH dependence of the experimental data in the slow aggregation regime than what is predicted theoretically. This effect is particularly pronounced for the unheated KEP10 and KEP30 particles. The discussed shift of the planes of origin or modification of the Hamaker constants lead only to parallel shifts of the calculated stability curves along the pH axis, but they do not affect their slope in the slow aggregation regime.

Similar discrepancies have been described for positively charged hematite particles, and for carboxyl latex particles [53, 58], and they can be reconciled by surface charge heterogeneities [29, 58, 59]. In the present case, we also suspect that these deviations are similarly related to lateral inhomogeneities on the surface of the silica particles.

The third effect concerns the increase of the stability ratios at low pH and high ionic strength. The effect is particularly pronounced for the unheated KEP10 and KEP30 particles, but is also noticeable for the heated KEP30H particles. Stabilization at low pH and high salt levels is characteristic for the anomalous stability of silica, and has been observed in a much more pronounced fashion for other silica systems. We suspect that this stabilization is related to repulsive forces between hairy surface layers. It is characteristic that this stabilization is accentuated for the unheated samples (KEP10 and KEP30), and for the heated samples it is either nonexistent (KEP10H) or very weak (KEP30H).

Absolute aggregation rates

The fast aggregation rate constants predicted by DLVO theory are $k_{fast} = 8.4 \times 10^{-18}$ m^3/s, which is about a factor 3-4 larger than experimentally observed (see table 1). The disagreement cannot be explained by assuming a different Hamaker constant. While the theoretical value decreases with decreasing Hamaker constant, it would be necessary to decrease the Hamaker constant by two orders of magnitude to reduce the rate constant by a mere factor of two. While such a low value of the Hamaker constant is not only unrealistic, the currently used value of $A = 8.3 \times 10^{-21}$ J gives good agreement with the stability data for the KEP10H sample. One might be tempted to suspect that additional repulsive forces due to the hairy layers might be responsible for the slow–down of the aggregation, but we do not favour this explanation. The main reason is that similar disagreement in the fast aggregation rates has been observed for sub–micrometer sized particles for hematite [45] and latex particles [41,53,60]. Otherwise, these systems behave according to DLVO theory, and there is no necessity to invoke a hairy surface layer. We rather suspect that these discrepancies are caused by inaccuracies of the interaction potential predicted by van der Waals theory at larger distances.

2.5 Conclusion

In this chapter we aimed to investigate the effect of heating on stability of colloidal silica particles in the presence of simple 1:1 electrolyte. We have shown that colloidal stability of heated Stöber silica particles follows the predictions of DLVO theory quantitatively. The particles were extensively characterized with respect to their size and charge, and their stability behavior can be predicted without adjustable parameters reasonably well. The present observation of agreement between silica stability and DLVO theory is in sharp contrast to many reports of anomalous colloidal stability of silica, in particular, featuring high stability at low pH and high salt levels. In the present work, we did confirm these trends for unheated Stöber silica particles, albeit to a much smaller extent than what was reported for other silica systems. We suspect that these anomalies are related to the repulsion between hairy surface layers of protruding polysilicic acid chains. This hypothesis is further confirmed by the present results, which demonstrate that simple heat treatment alters the colloidal stability of silica, which must be therefore related to different surface morphologies.

3 Charging of silica particles in the presence of divalent counterions

3.1 Introduction

In chapter 2, we studied behavior of colloidal silica particles in presence of monovalent salt – KCl. We showed that upon heating, the charging characteristics of originally porous Stöber–type silica particles will follow the 1–pK basic Stern model. Electrophoretic mobility in presence of monovalent counterions was rationalized with the model of O'Brien and White. In this chapter, we extend our studies of surface charge for the case when a 2:1 electrolyte is present.

Ca^{2+} ions are one of the most common cations present in the Earth's crust. From the viewpoint of colloid chemistry, Ca^{2+} compounds have numerous applications, for example as a coagulation agent in food industry or as a major component of building materials. Regarding the latter application, silica particles in presence of Ca^{2+} is an interesting model system for investigation of interaction between particles in cement [72]. Despite their significance, thorough studies on charging behavior of these colloidal systems are scarce. There is still large gap between the importance of the charging process of systems containing multivalent ions and our understanding of these systems. Dove et al. [63] performed titrations of pyrogenic nonporous silica particles in mixture of Na^{+} with various monovalent and divalent ions. They found that the surface charge in presence of divalent counterions was higher for the whole range of accessible pH, compared to the charge developed in mixtures of purely monovalent cations. Labbez et al. [64] provided support of the latter results with simulations, showing that exchange of monovalent for divalent counterions allowed much higher ionization of surface.

3.2 Materials and Methods

For measurements of both surface charge density and electrophoretic mobility, we used the KEP10H Stöber-type silica particles. These particles were thoroughly characterized as described in previous chapter, and their properties are summarized in table 2.

Potentiometric titrations at constant ionic strength were performed with home-built precise automatic titrator [10], in a similar way than described in chapter 2. Software which drives the titration experiment was beforehand adapted such that it was able to perform titrations at constant ionic strength with a 2:1 base, 1:1 acid and 2:1 salt. Doses of acid, base, salt and water added during blank titration were used for verification that the ionic strength is kept constant for each measured point. Typical mass of titrated sample of KEP10H silica was 1 g. Titrator burettes were filled with 0.25 M HCl prepared from Titrisol concentrate by Merck (Zug, Switzerland), analytical grade 3 M $CaCl_2 \cdot 6\ H_2O$ from Fluka (Buchs, Switzerland), 0.019 M $Ca(OH)_2$ and water. Solution of $Ca(OH)_2$ was obtained by heating of $CaCO_3$ purchased from Acros Organics (Geel, Belgium) at 1000°C and dissolving the calcium oxide in water. The solution of base was replaced with a fresh one every 3 days. All solutions were prepared from CO_2-free boiled water, purified beforehand with Milli-Q A10 UV/UF system (Millipore, Billerica, USA). To minimize the contamination with carbonates coming from air, all burette solutions were flushed with CO_2-free nitrogen and sealed.

Concentration of carbonates in solutions titrated with $Ca(OH)_2$ was approximately twice higher than in the case of titration with KOH. Nevertheless, the amount of carbonates remained low, typically less than 30 μM, and stayed almost constant during experiments. This point was verified by comparing silica titrations against two blank titrations: one performed before and the other after a set of sample titrations. No significant difference could be observed for the two blanks.

Measurement of electrophoretic mobility in presence of Ca^{2+} was performed at conditions very similar to those used for measurements with K^+ (chapter 2). Ionic strength was adjusted by addition of $CaCl_2$, pH of sample was set with HCl or $Ca(OH)_2$, with the same chemicals as used for potentiometric titrations. Before measurement, the sample was divided in two parts. One part was used to determine electrophoretic mobility, and in the second part the pH of the sample was simultaneously measured with a combination electrode 6.0234.110 from Metrohm (Herisau, Switzerland). Value of pH was read as soon as there was no observable drift. Again, attention was paid to minimize contamination of samples with CO_2 from air.

3.3 Monte Carlo simulations

In chapter 2, we used the 1–pK basic Stern model and the model of O'Brien and White to calculate theoretical surface charge and electrophoretic mobility, respectively. Theoretical predictions by these classical models agreed very well with experimental data in presence of monovalent ions (fig. 10). However, as pointed by Labbez et al. [64], in the presence of divalent counterions and/or high surface charge, the prediction by the above mentioned methods does not describe the experiments very well. Moreover, the O'Brien and White theory fails to explain electrophoretic mobility experiments even qualitatively. Therefore, an other model had to be adopted to describe the experiments.

We are grateful to Dr. Christophe Labbez from the University of Bourgogne in Dijon (France) for performing Monte Carlo simulations, using a model he developed together with Prof. Bo Jönsson from the Lund University, in Lund (Sweden). Their simulations are based purely on electrostatic interactions, without any assumption of chemical specific interactions. Here we briefly summarize basic features of the Monte Carlo (MC) model, further details might be found elsewhere [64,71,72]. MC method in the grand canonical ensemble allows to simulate the titration behavior of solid surfaces. A surface is defined by explicit titratable sites, which have the same intrinsic dissociation constant. Titratable sites have defined surface density and a minimum separation between the ions and the sites. In this approach, unlike for the 1-pK basic Stern model, there is no need for introducing Stern capacitance. Ions are modeled as charged hard spheres, solvent is treated as a dielectric continuum, and solid surfaces are assumed to be smooth and uniformly charged – the so-called primitive model. Simulation of a titration consists of many attempts of deprotonation and protonation. For each such attempt trial energy is evaluated and the protolytic reaction is only accepted if Boltzmann factor of the trial energy is smaller than a random variable. The aforementioned Monte Carlo simulations were previously shown to fit well to experimental results on calcium silica hydrate ($CaO\cdot SiO_2\cdot H_2O$) particles [64] in the presence of monovalent and divalent counterions. Measurements of ζ-potential of spherical silica particles [69] were also in accordance with the MC simulations. Despite the fact that no fitting parameters had to be included, MC simulations agreed very well with the results of classical 1–pK basic Stern model [64] in the presence of monovalent counterions.

3.4 Results and discussion

Surface charge

According to the observations of Dove et al. [63] and also following the MC simulations presented further in fig. 14b, surface charge in presence of Ca^{2+} should be for the whole range of measured pH higher than the charge in the presence of K^+. However, from the comparison of titration curves for KEP10H silica in presence of K^+ and Ca^{2+} ions in fig. 12, one can see that at low pH, the charge in presence of potassium is higher than the one in the presence of calcium. Finally at higher pH, silica is considerably more charged in presence of calcium for all ionic strengths. In other words, the Ca^{2+} curve seems to be shifted along pH axis towards higher pH value. Another feature of curves for the various ionic strengths of Ca^{2+} is that they seem to be slightly

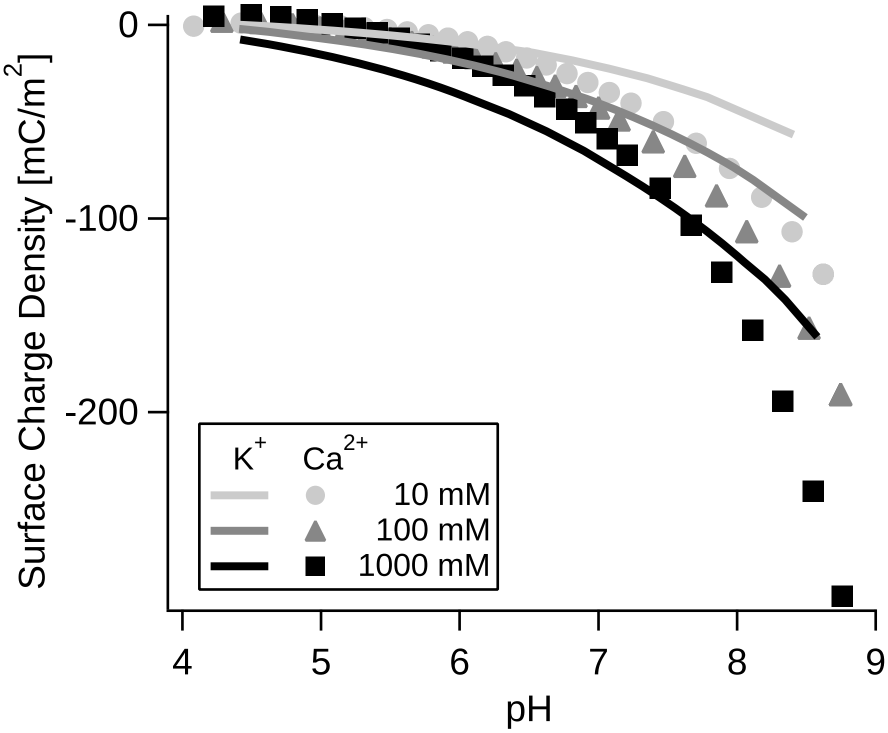

Figure 12: Surface charge density of KEP10H silica particles in presence of K$^+$ (lines) compared with Ca^{2+} (markers) at different values of ionic strength. Forward titration curves shown only. Characteristics of KEP10H particles can be found in tab. 2.

closer, indicating less pronounced dependence of charge on ionic strength. While the latter can be explained by better ability of Ca^{2+} ions to screen the charge, more investigation is necessary to gain insight to the overall shift of the charging curve in presence of Ca^{2+}.

In presence of divalent counterions, MC simulations predict complete ionization of surface groups at pH 13–14 for CaO·SiO$_2$·H$_2$O particles [64]. In order to assess to which extent our silica particles can be charged in the presence of Ca^{2+} ions, we performed an other titration experiment with the range of pH extended to 10.5. The maximum value of pH was chosen following the work of Kobayashi et al. [26]. In the latter paper authors were investigating the effect of pH on silica dissolution and found that at pH 10.5 the dissolution rate was not negligible, but still small. However, above pH 12 it becomes significant. We repeated the experiment with extended range of pH in presence of Ca^{2+} three times, in order to check the reproducibility of results and reversibility of forward and backward titration steps. Reversibility appeared to be problematic for some previous experiments in presence of K^+ ions (see fig. 9a and b).

Charging curves of KEP10H silica titrated with $Ca(OH)_2$ up to pH 10.5 (fig. 13b) are compared with a similar titration, in which the maximum pH was limited to 8.5 (fig. 13a). Upon increase of upper pH limit, the coincidence between forward titration (acidic to basic, full symbols) and backward titration (basic to acidic, open symbols) becomes poor. Repeating the same experiment three times (fig.13c and d) served as a check of reproducibility. For each experiment, curves at ionic strength (10, 100 and 1000) mM were measured in forward and backward direction. While the very first runs (forward 10 mM) from the three independent experiments show good reproducibility (fig. 13c), once the suspension reaches pH above 8.5, the reproducibility of the following 10 mM backward curves (fig. 13d) is lost. Similar trends were observed for all consequent curves (100 mM and 1000 mM, not shown).

We observed the lack of reversibility before at higher ionic strengths for unheated Stöber-type silica (KEP10 and KEP30, chapter 2) titrated with KOH. This observation was explained by the microporosity of unheated particles. Upon heating, the pores were closed off and titration curves became reversible (fig. 9). However, at certain conditions the surface modification by heating seems to be reversible [34]. For titrations with $Ca(OH)_2$ at high pH, calcium ions were most probably able to re-open the pores and so the amount of titratable sites was changing during the titration. Unlike the case of titration with KOH, with $Ca(OH)_2$ the hysteresis effect appeared even for heated particles and also at low ionic strength. The latter can be rationalized by better ability of Ca^{2+} ions to screen the charge, which facilitates creation of new surface by opening pores. In addition, we cannot rule out formation of small quantities of calcium silicate hydrate layer on particle surface. The

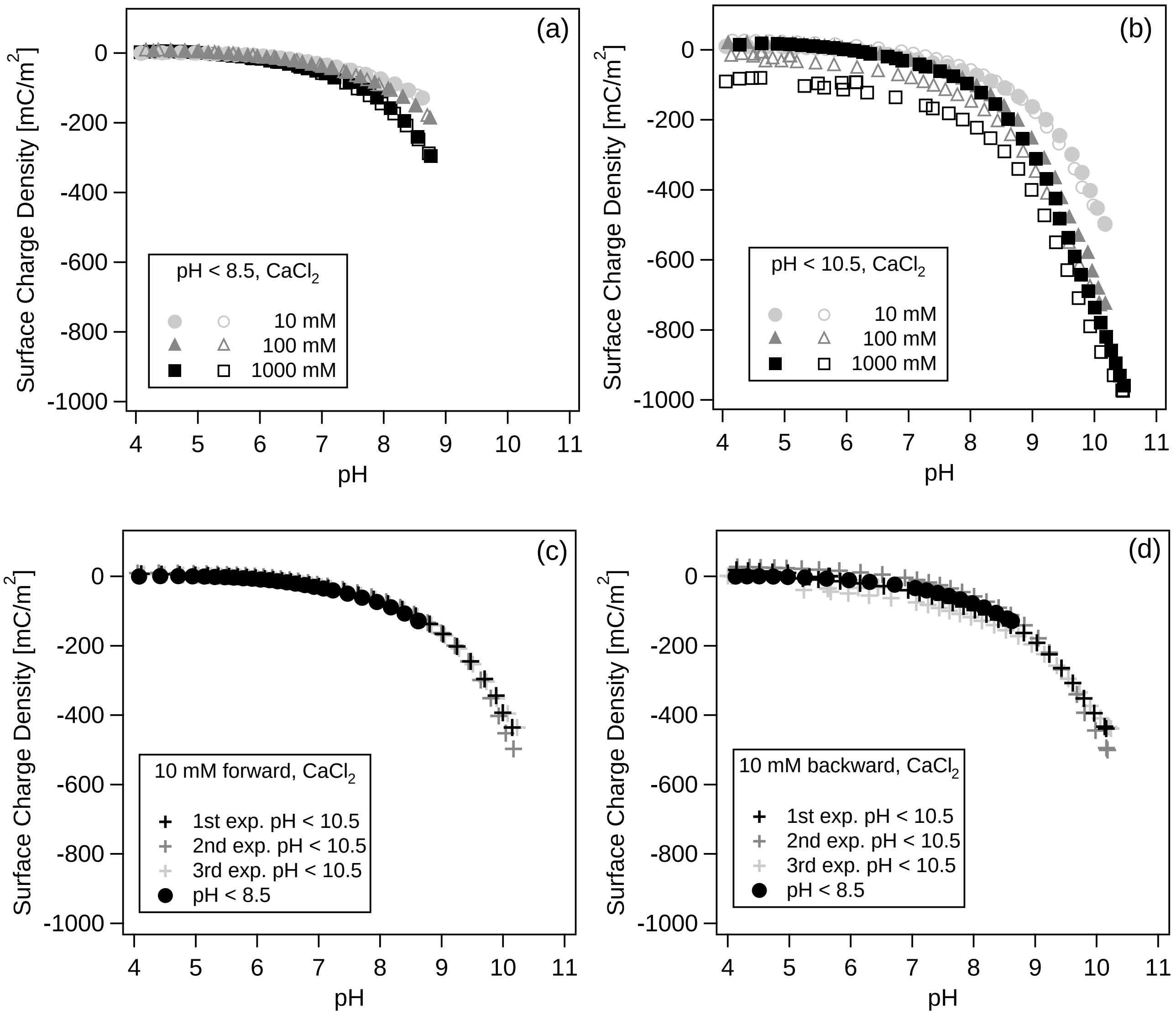

Figure 13: Potentiometric titration of KEP10H silica particles with $Ca(OH)_2$ at constant ionic strength. Full markers denote forward titrations, open markers are for backward curves. Titration up to (a) pH 8.5, and (b) pH 10.5. Curves selected from three independent titration experiments are (c) first forward titrations (10 mM) and (d) first backward titrations (10 mM) both performed up to pH 10.5 and compared with corresponding curve from (a).

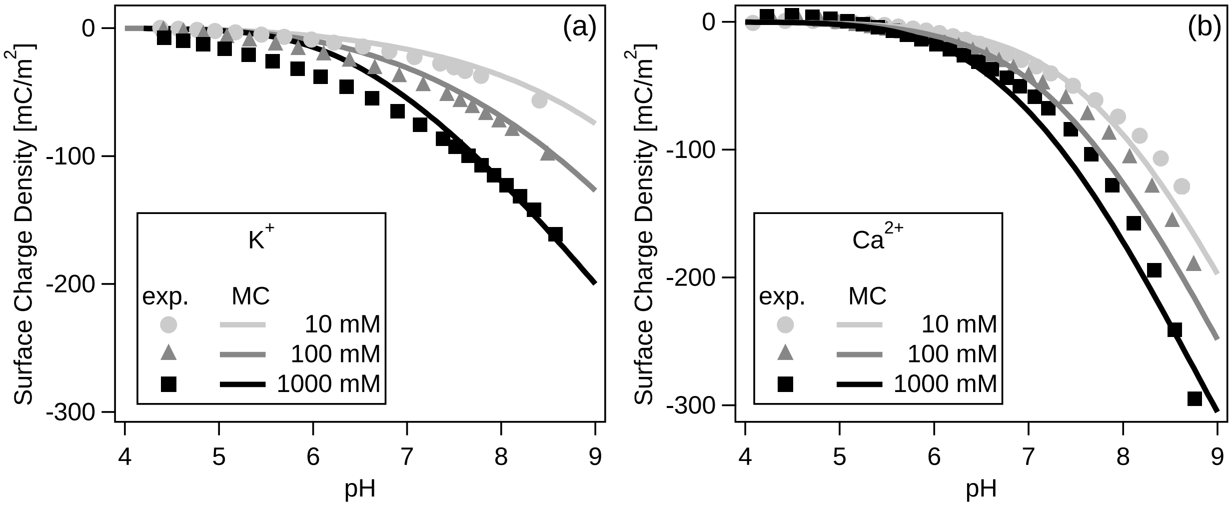

Figure 14: Potentiometric titration of KEP10H silica in presence of (a) K^+ and (b) Ca^{2+} ions. Experiments (markers) are compared to Monte Carlo simulations (lines) with parameters: p$K = 7.7$, surface site density 5 nm^{-2}, minimum separation between the ions and the silanol groups 0.15 nm.

latter compound is only stable at pH above 10.3 [64] and its appearance could also contributed to the hysteresis effect.

Experimental charging data obtained by potentiometric titrations are compared with MC simulations in fig. 14. Simulations in presence of both K^+ and Ca^{2+} represent the best fits to the experimental data, using the following parameters: p$K = 7.7$ and surface site density of 5 nm^{-2}, minimum separation between the ions and the silanol groups was set to 0.15 nm. The values of pK and surface site density differ somewhat from those used in chapter 2 for the same particles. In the latter case, p$K = 7.5$ and surface site density of 8 nm^{-2} as proposed in [51]. Nevertheless, assuming that the MC simulations are based purely on electrostatic interactions and do not need to use a fitting parameter, the data coincide well with those obtained with 1–pK basic Stern model.

Problems arising from poor reproducibility of charging curves could be possibly resolved by changing the silica sample each time it reaches pH above 8.5. Complete ionization of Stöber-type silica surface could not be observed by titration with $Ca(OH)_2$. However, in presence of trivalent ions (e.g., La^{3+}) full surface ionization of Stöber-type silica particles might be possible.

Electrophoretic mobility

Electrophoretic mobility of KEP10H silica particles in presence divalent cations as a function of pH was compared with MC simulations (fig. 15). Comparison of electrophoretic mobility in presence of Ca^{2+} with analogous measurements in presence of K^+ (fig. 16) reveals qualitatively different behavior. While in presence of monovalent cations the electrophoretic mobility monotonically increases in absolute value with increasing pH, in presence of divalent cations a maximum around pH 6.5 appears. For higher pH, mobility diminishes, and eventually at the highest measured ionic strength, reaches even slightly positive values. On the contrary, surface charge density in presence of K^+ as well as Ca^{2+} increases monotonically in absolute value for the entire range of pH measured, as observed by potentiometric titrations (fig. 13).

We assign the inversion of electrophoretic mobility at high pH to the overcharging phenomenon. Overcharging is an occurrence of electric double layer, in which there is more countercharge than charge on the surface [70]. However, it is always important to specify the kind of charge we are discussing. While the electrokinetic charge, as sensed by measurement of electrophoretic mobility, reverses its sign with increasing concentration of Ca^{2+}, the sign of the surface charge, as measured by potentiometric titration, does not change. On the contrary, its absolute magnitude even increases because of better screening (cf. fig. 12). Strong accumulation of counterions in the vicinity of the surface originates from ion-ion correlations [64], which are favored by high pH and/or high concentrations of Ca^{2+}. Neglect of ion-ion correlation in the 1–pK basic Stern model leads to an underestimation of the accumulation of calcium ions close to the charged surface.

As we can see from fig. 15, the coincidence of MC simulation with experimental data is not ideal. We suggest two possible explanations, which

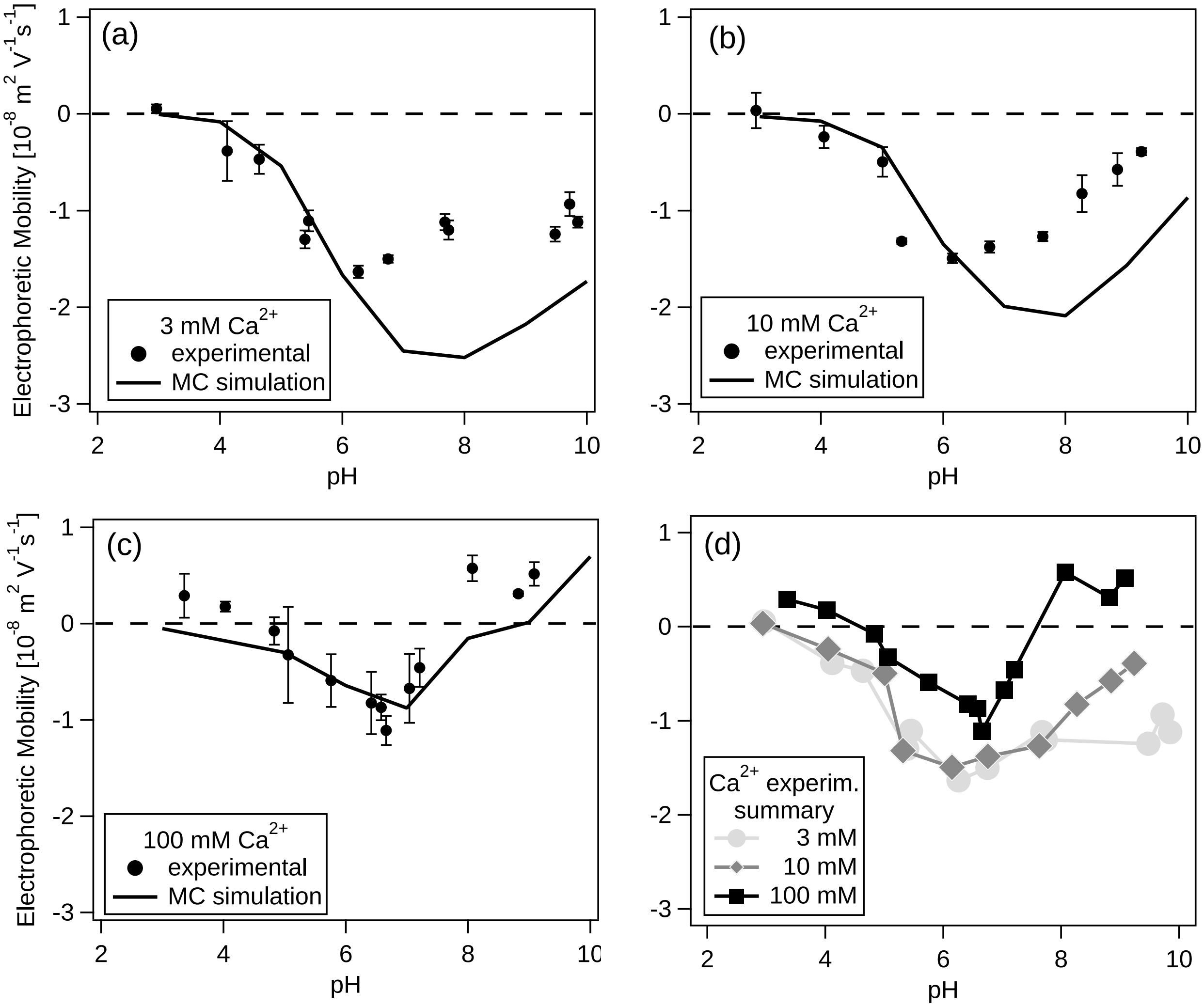

Figure 15: Electrophoretic mobility of KEP10H silica particles in presence divalent cations, at ionic strengths (a) 3 mM, (b) 10 mM and (c) 100 mM. Experimental data (small circles) are compared with MC simulations (solid lines) with the following parameters: pK = 7.7, surface site density 5 nm^{-2}, minimum separation between the ions and the silanol groups 0.15 nm. Error bars are standard deviations from 6 measurements. Dashed lines indicate zero mobility. Figure (d) summarizes experimental data from figures (a), (b) and (c); lines are for eye guide only.

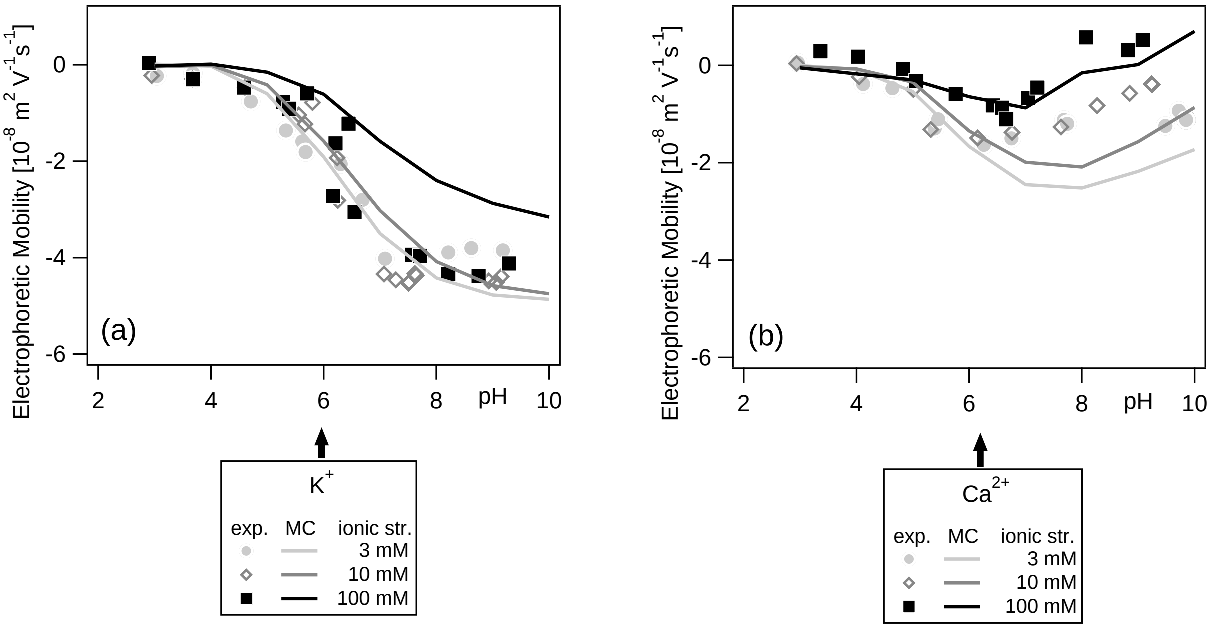

Figure 16: Electrophoretic mobility of KEP10H silica particles in presence of K^+ (a) and Ca^{2+} (b) at different ionic strengths . Experiments (markers) are compared with MC simulations (lines) with following parameters (applies for both (a) and (b)): $\mathrm{p}K = 7.7$, surface site density $5\ \mathrm{nm}^{-2}$, minimum separation between the ions and the silanol groups 0.15 nm.

are arising from limitations of the used model [73]. In the first place, the position of slipping plane used in calculations is model-dependent, and it is rather an abstraction with weak correlation to the real situation. Second weak point is the self-consistency of our approach. On one hand, in order to calculate ζ-potential, we use an exact solution of the primitive model, which includes finite ion size and accounts exactly for the ion-ion correlations. As mentioned above, latter phenomena has to be taken into account for the system including divalent counter ions, otherwise the predictions would fail even qualitatively. On the other hand, we use O'Brien and White theory [52], which is a mean–field approximation of the primitive model, to calculate electrophoretic mobility from the simulated ζ-potential. Thus, as a consequence of the two drawbacks of used model, even though the MC simulations captured the trends in experimental data very well, they should be treated as semi-quantitative. Better description would need a more detailed knowledge of the particle surface state and very complex numerical approach, which is not yet available.

The MC simulations were able to explain the sign reversal of the electrophoretic mobility without any assumptions of non-physical interactions. More specifically, no assumptions about chemical interactions, such as specific adsorption were used. Following parameters were used for MC simulations of ζ-potential as a function of pH: surface density of the silanol groups 5 nm^{-2}, intrinsic ionization constant of silanol groups $\mathrm{p}K = 7.7$ and the minimum separation between the ions and the silanol groups was set to 0.15 nm.

While positive electrophoretic mobility is predicted by MC simulations at higher pH, it is more difficult to understand the charge reversal at the lowest pH for the 100 mM curve. If this was a result of decreased sensitivity of the instrument around zero mobility, we would expect to observe significant data scattering also for other ionic strengths, as well as for the experiments with KCl as background electrolyte. However, such scattering was not observed. Therefore, we suspect that the positive mobility at low pH might be a sign of a low, non-electrostatic adsorption of Ca^{2+} to the silica surface. Nevertheless, pure electrostatic interaction is most probably the major parameter that governs the charging process and electrokinetic behavior of silica in contact with monovalent and multivalent ions [64, 73].

Due to intrinsic limits of the setup used for electrophoretic mobilities, the highest accessible ionic strength of sample was 100 mM. Electroacoustic measurements could in future overcome this limit, and most probably will enable us to observe the overcharging effect even more pronounced at ionic strengths above 100 mM.

3.5 Conclusion

In the present chapter, we have examined surface charge density and electrophoretic mobility of colloidal silica particles in presence of divalent counterions. We have compared titration behavior of silica in presence of 2:1 electrolyte with MC simulations as well as with similar experiment in presence of 1:1 salt. Electrophoretic mobility measurements in presence of Ca^{2+} ions revealed qualitatively different behavior of silica, compared to analogous experiment in presence of K^+. Inversion of the sign of the electrophoretic mobility, which was not observed for the 1:1 electrolyte, was predicted by MC simulations and rationalized by ion-ion correlations. Neglect of the latter phenomena in systems containing divalent counterions caused the classical models to fail. Since the MC simulations were based purely on electrostatic interactions, we suppose that electrostatic interaction is the most important factor that features the charging process and electrokinetic behavior of silica in presence of monovalent and divalent ions. Non-electrostatic interactions can be equally important, but they are most probably not the main mechanism determining surface charging.

In the next chapter, we will advance in our investigations of interactions between colloidal particles with ions. Interaction of organic multivalent ions (polyelectrolytes) with particles will be addressed, and the structure of adsorbed monolayer of a polyelectrolyte will be studied.

4 Hydrodynamic thickness of polyelectrolyte monolayer on colloidal particles

4.1 Introduction

So far we were concerned with behavior of colloidal particles in presence of a simple electrolyte. In this chapter, we would like to investigate more complex systems, which will be composed of colloidal particles, monovalent simple electrolyte, and organic polyions – polyelectrolytes. Although there are numerous studies on thick layers of neutral polymers or alternating multilayers of positively and negatively charged polyelectrolytes, little is known about the first adsorbed layer. Properties of the first layer may be different from the next layers [77], especially the thickness of layers deposited immediately onto the solid substrate is lower than of those further away. Understanding the properties of the first adsorbed monolayer, which may constitute the starting block for further multilayer build-up, can bring substantial insight into the mechanisms of polyelectrolyte adsorption.

Due to the intrinsic nature of the adsorbed polyelectrolyte layer, which is likely to be thin and not dense, studies on the thickness of an adsorbed polyelectrolyte monolayer are scarce. Liu et al. [74] investigated adsorbed monolayer of humic acid on planar mica surface. Humic acid formed rather isolated islands with height (4–6) nm as found by atomic force microscopy. An et al. [5] examined structure of a diblock co-polymer at a flat substrate. The chargeable segments of co-polymer were adsorbed, whereas the neutral units were partially grafted onto the surface. Therefore, the layer exhibited properties of both adsorbed layer and polymer brush. Investigation of layer structure revealed that it was composed of a thin dense layer containing all neutral segments and a diffuse layer containing only chargeable units. Maximal overall layer thickness did not exceed 4 nm. Thorough study on layer of co-polymer, composed of both neutral and charged monomeric units, adsorbed on colloidal silica particles, was performed by Bauer et al. [75]. Properties of the co-polymer layer were examined as a function of molecular mass, pH and ionic strength. Layer thickness was increasing with higher adsorbed co-polymer amount and with increasing co-polymer molecular mass and was in general in the range of 1 nm to 17 nm. Rustemeier [78] has shown that the monolayer of poly-L-lysine is relatively very thick. They observe up to 35 nm at the highest salt levels. Monolayer thickness can be also estimated from the thickness of PE multilayer by dividing the overall thickness by number of layers deposited. Alternating layers of negatively charged poly(styrene sulfonate) and positively charged poly(allylamine) hydrochloride adsorbed on surface-modified Si wafers were studied in this respect [76]. Thickness of one monolayer was 3.5 nm and 2.0 nm, for the polyanion and polycation, respectively.

In this chapter, we aim to investigate thickness of an adsorbed monolayer of polyelectrolyte on an oppositely charged colloidal particles by means of dynamic light scattering. By term "monolayer" we mean layer composed of only one type of polyelectrolyte, as opposed to multilayers formed by two or more types of polymers.

Layer buildup versus particle aggregation

The thickness of a polyelectrolyte monolayer on spherical colloidal particles can be determined as a difference between the mean radius of particles before and after polyelectrolyte adsorption. This simple approach was used before to determine thickness of long grafted polymer chains [79] or the thickness of a stack of polyelectrolyte multilayers [80]. In both mentioned cases, the thickness of the layer was in the same order of magnitude as the size of particles, or larger.

Our aim was to investigate adsorbed polyelectrolyte monolayer, whose hydrodynamic thickness is expected to be one to two orders of magnitude smaller than the particle size. If the above-mentioned simple approach would be employed for measurement of such thin layer, the measured thickness could be seriously overestimated due to neglect of particle aggregation. Therefore, special attention has to be paid to the experimental conditions, in order to ensure that the observed increase of particle size is only due to the buildup of the layer.

4.2 Materials and methods

Colloidal particles

Two types of colloidal particles were used: amidine latex and sulfate latex. All data on particle properties in table 3 were provided by the manufacturer, except the hydrodynamic radii measured with dynamic light scattering by us.

Prior to use, the original suspensions were cleaned with dialysis against Milli-Q water with cellulose ester membrane (molecular mass cutoff 300 kg/mol) until no change in the conductivity of the surrounding water was detected. Alternatively, we purified suspensions with ultrafiltration in a stirred cell Amicon 8010 (Millipore, Billerica, USA), with PLGC02510 regenerated cellulose filter (nominal molecular mass limit 10 kg/mol). Concentration of purified suspension was then determined with static light scattering.

Polyelectrolytes

Three types of polyelectrolytes were used for layer thickness measurements.

Poly(dimethyl-diallylammonium chloride), which we further refer to as PDADMAC, is a strong cationic polyelectrolyte (fig. 17a). It carries one positive charge per monomer unit thus resulting in a line charge density of about 1.1 nm^{-1}. PDADMAC was purchased from Sigma-Aldrich Chemie (Steinheim, Germany), as 20 wt.% solution in water, product number 409030-1L. The content of carbon and nitrogen, as well as the solution concentration were verified by the total carbon and nitrogen analysis [10], and were found to

Table 3: Characteristics of the latex particles studied

	Amidine latex	Sulfate latex
Name	surfactant-free white amidine latex	surfactant-free sulfate white polystyrene latex
Manufacturer	Interfacial Dynamics Corporation (Portland, USA)	
Batch	1939,1	1521,3
particle shape	spherical	
radius (transmission electron microscopy)	105 nm	95 nm
radius (dynamic light scattering)	110 nm	96 nm
coefficient of variation	0.08	0.03
density at 20°C	1055 kg/m^3	
functional group	amidine positively charged	sulfate negatively charged
surface charge density	100 mC/m^2	10 mC/m^2
pH-dependence of surface charge	almost independent (cf. fig. 33)	independent
dispersing medium	de-ionized water	

agree with the formula. Typical molecular mass is according to the manufacturer 400 kg/mol – 500 kg/mol , which indicates rather high polydispersity. The polyelectrolyte was used without further purification.

Poly(sodium styrene sulfonate), abbreviated PSS, with chemical formula in fig. 17b. Three different solid samples were purchased from Polymer Standards Service GmbH (Mainz, Germany), and used as received. Three types of PSS were used with different molecular masses; properties of the three polyelectrolytes from the producer are summarized in table 4.

Poly(vinylamine), also known as PVA (fig. 17c). Two polyelectrolytes

Table 4: Characteristics of PSS by the producer

Notation	M_m * [kg/mol]	M_p * [kg/mol]	D * [1]	batch No.
PSS29k	29	29.5	< 1.20	pss1088
PSS323k	323	340	< 1.04	pss200203
PSS2260k	2260	2350	< 1.20	pss8034-3

* M_m = weight average molecular mass

M_p = molar mass at the peak maximum

D = polydispersity index

were kindly provided in aqueous solutions by BASF Aktiengesellschaft (Ludwigshafen, Germany). Polymeric chain of both types of PVA are composed of two types of monomers: chargeable vinylamine (fig. 17c, top) and neutral vinylformamide unit (fig. 17c, bottom). Monomeric units with amine and formamide groups are distributed randomly along the linear polymer chain. We denoted the two different samples of PVA as PVA32 and PVA94, according to the ratio of the chargeable –NH_2 units (32% of –NH_2 in PVA32, 94% of –NH_2 in PVA94). All experiments with PVA were conducted at pH 4; at this pH more than 90% of –NH_2 groups are protonated [66]. Both samples

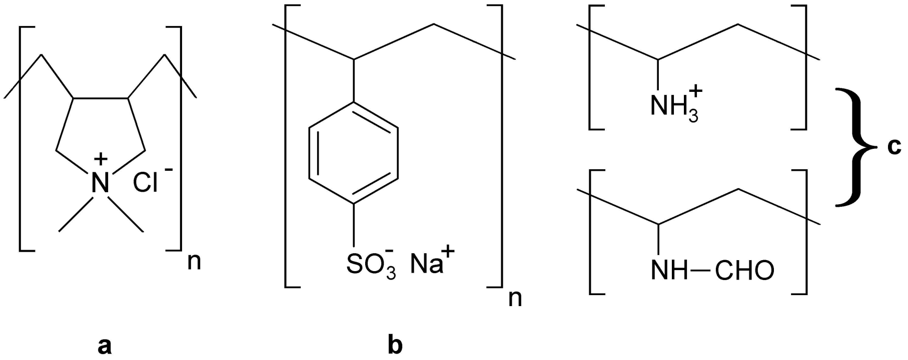

Figure 17: a) PDADMAC, b) PSS and c) PVA.

were used without further purification. Summary of the properties provided by the manufacturer for the two PVA polyelectrolytes is in table 5.

Other materials

Deionized filtered water, used for preparation of all solutions, was prepared with the Milli-Q A10 UV/UF system (Millipore, Billerica, USA). Total organic carbon content in water was less than 10 ppb, conductivity 18 MΩ cm or higher.

As we worked with very low concentrations of particles and polyelectrolytes, special attention had to be paid to the cleaning of glassware and plasticware used. In order to remove dust and residuals of organic impurities, we used the following cleaning procedure. Borosilicate glass cuvettes for single use Tube Hemolyse Boro 12×75 mm (Fisher Scientific, Wohlen, Switzerland) were cleaned with boiling mixture of concentrated H_2SO_4 and 30% solution of H_2O_2 at volume ratio of 3:1. Afterwards, they were rinsed extensively with MilliQ water and left immersed in water for at least 4 hours. The washing process with water was repeated 3 times in total. After quick drying in an oven the cuvettes were stored closed in a dust-free environment. For amidine latex particles, we preferred to use plasticware rather than glass, in order to avoid sticking of positively charged particles to negative charged glass surface. Plastic vessels were treated with 2% aqueous solution of Hellmanex II from Hellma GmbH (Müllheim, Germany) during at least 3 hours

Table 5: Characteristics of PVA by the manufacturer

Notation	Product name	pH of solution	Mean molecular mass [kg/mol]	Degree of hydrolysis [%]
PVA32	GK 181/91	7	470	32.1
PVA94	GK 181/80	11.5	520	94.3

at 60°C and then rinsed with copious amounts of Milli-Q water.

For all experiments, we used p.a. purity potassium chloride from Acros (Basel, Switzerland) as background electrolyte. Concentrated solutions of KCl were prepared from solid salt and prior to use, they were filtered twice with Durapore PVDF Membrane 0.1 μm filter by Millipore (Billerica, USA). Adjustment of pH was done with Titrisol solutions of HCl from Merck (Glattbrugg, Switzerland) or CO_2-free Dilut-it KOH purchased from Mallinckrodt Baker (Basel, Switzerland), respectively, in the range of 0.001 M to 1 M.

The most diluted suspensions of particles and polyelectrolytes were stored in dark and under refrigeration. Nevertheless, based on check of initial particle size and also decreased reproducibility of measurements, we found that after about 10 days the suspensions were aged. All diluted suspensions were therefore used for no longer than 3 days.

All components of the sample for layer thickness measurements, except the polyelectrolyte, were prepared at pH 4. Measurements of pH were performed with combination electrode 6.0234.110 made by Metrohm (Herisau, Switzerland) with continuous stirring of sample, until no drift was observed.

Dynamic light scattering

Hydrodynamic layer thickness of adsorbed polyelectrolyte was determined by dynamic light scattering. We have summarized theoretical background on this technique in section 1.2.

To decrease the total time necessary for a set of layer thickness measurements, we often measured two samples in parallel on two similar setups: goniometer system with 8 detectors and a compact goniometer.

Laser Goniometer System ALV/CGS-8F from ALV GmbH (Langen, Germany) was equipped with a 532 nm solid-state laser Verdi V2 made by Coherent Inc. (Santa Clara, USA) operated at 0.4 W. From the field of 8 detectors available, only one detector was used. Experiment run and cumulant fitting were performed with the ALV–5000/E-WIN (ver. 2.2.5) software.

Compact Goniometer System ALV/CGS-3 from ALV GmbH (Langen, Germany) with one detector and a 632.8 nm laser light source, model 1145P-3083 from JDS Uniphase, laser power 0.035 W. Experiment run and cumulant fitting were performed with the ALV–5000/E/EPP software (ver. 3.0.1.15).

All measurements were realized in an index matching bath filled with filtered toluene and thermostated at 25°C. Scattering angle was set to 90° for all measurements. Several layer thickness measurements were performed on both light scattering setups, and the results showed very good agreement.

Electrophoretic mobility

Electrophoretic mobilities were measured with a laser doppler velocimeter setup Zetasizer 2000 (Malvern Instruments Ltd., Malvern, UK). Basic principles of the method can be found in section 1.2.

Cell potential was set to 75 V, except for the measurements at 0.01 M ionic strength, where it was increased to 100 V. The reported electrophoretic mobilities are average values from at least 6 consecutive measurements.

4.3 Layer thickness measurements

In order to find appropriate experimental conditions for measurements of a very thin layer, prior to the layer thickness measurement itself, we have to perform a set of preliminary experiments. First, aggregation of bare particles has to be examined. The latter includes determination of critical coagulation concentration of bare particles and optimization of initial particle size and concentration. In the next preliminary measurement, we will investigate adsorbed mass of polyelectrolyte, with focus on polyelectrolyte dose at isoelectric point. The goal of this section is to describe in more detail the aforementioned procedure for the layer thickness measurement.

Aggregation of bare particles

After mixing colloidal particles with polyelectrolyte solution, an increase of the mean particle size often occurs, especially at higher ionic strengths. In the first approach, overall increase of mean particle radius can be intuitively assigned to the adsorption of polyelectrolyte. However, the mean size increase cannot be in general attributed only to the buildup of polyelectrolyte layer on particles, as aggregation of particles has to be taken into account as well. This is especially important in the case the layer thickness is small compared to the particle radius. Therefore, to determine the thickness of a thin adsorbed monolayer, it is crucial to distinguish the two contributions to the observed increase of the mean particle size.

Separation of the two contributions can be achieved by working at experimental conditions, where the rate of increase of the mean particle size due to aggregation is negligible compared to the rate of increase due to the formation of layer. The suppression of the aggregation can be accomplished by sufficient dilution of the particle suspension and by verifying that the aggregation rate is negligible even at conditions which favor fast (diffusion limited) aggregation. In other words, the extreme dilution reduces the particle aggregation rate to the point that the time scale of polymer adsorption is fast with respect to the characteristic time of the aggregation [62].

In the following, we will first try to find a critical concentration of salt, at which the aggregation of bare particles starts to be diffusion limited. At these conditions, particles start to undergo fast aggregation. Afterwards, we will discuss the selection of particle size and finally optimize the particle concentration at the conditions favoring fast aggregation, that is above the critical coagulation concentration.

The critical coagulation concentration (CCC) of a colloidal dispersion is a concentration of salt, at which abrupt change appears from stable to instable dispersion [7]. DLVO theory predicts that with increasing concentration of salt the stability ratio (eq. 6) decreases. Above the CCC, stability of suspension is not anymore dependent on concentration of salt; fast (diffusion limited) aggregation appears.

Essential condition for the measurement of thin layer thickness is that the time scale of particle aggregation is slow with respect to the characteristic time of the layer buildup. To find this point, we will try to find an optimal particle concentration at salt concentration higher than CCC. This means that we will look for conditions, at which even though the salt favors fast aggregation, the time scale of particle size increase is slow compared to the time scale necessary for the buildup of layer. Thus, the value of CCC serves as starting point for layer thickness measurements.

Stability measurements were conducted as described before in section 2.3. Appropriate amount of concentrated KCl solution was added to water in a borosilicate cuvette and stirred with vortex mixer. Afterwards, 200 μl of particle suspension was added, such that the total sample volume was 2000 μl and the total particle concentration was 0.54 mg/L of suspension. All sample components (water, KCl and particles) were beforehand acidified with HCl to set the pH to 4. Measurement of hydrodynamic radius started immediately after the sample preparation and lasted typically for about 1000 seconds.

Aggregation rate of suspension, expressed in terms of stability ratio, was examined as a function of salt concentration (fig. 18). The CCC separates the regions of slowly aggregating (stable) suspension ($<$ 250 mM) and fast aggregation regime (above 250 mM KCl), where the stability is not anymore sensitive to the increasing concentration of KCl.

We thus conclude, that the following measurement (optimization of the initial particle concentration) should be done at salt concentration of 500 mM, which is safely in the fast aggregation regime.

The optimization of initial particle size and concentration was carried as follows. Fig. 19 shows linear fits to the time dependence of the mean

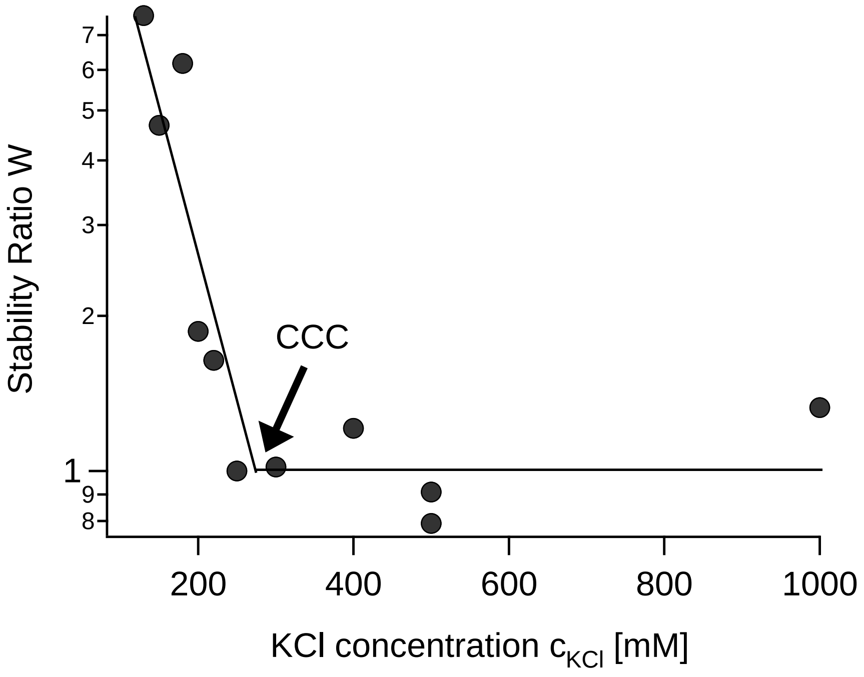

Figure 18: Stability ratio of sulfate latex particles, at pH 4. Lines are for eye guiding only. Critical coagulation concentration (CCC) is marked with an arrow.

particle radius of an aggregating suspension, at different concentrations of sulfate latex particles. Vertical axis represents hydrodynamic radius from which the initial hydrodynamic radius (at time zero) was subtracted. We refer to this quantity as the reduced hydrodynamic radius. Measurements were conducted at 500 mM KCl, that is at concentration which is safely above the CCC, as we concluded from the previous section. In other words, all measured suspensions exhibited fast aggregation.

Since we expect the layer thickness to be in order of 1 nm to 10 nm, from fig. 19 it is evident that at initial particle concentration of 0.535 mg/L the aggregation would make the layer thickness measurement impossible. After 4 hours, which is a typical time at which the thickness is evaluated, the overall increase of mean particle size would amount to 154 nm, as estimated by linear extrapolation. Nevertheless, by decreasing the concentration down to 0.011 mg/L, the overall size increase after 4 hours diminishes below 1 nm. This is

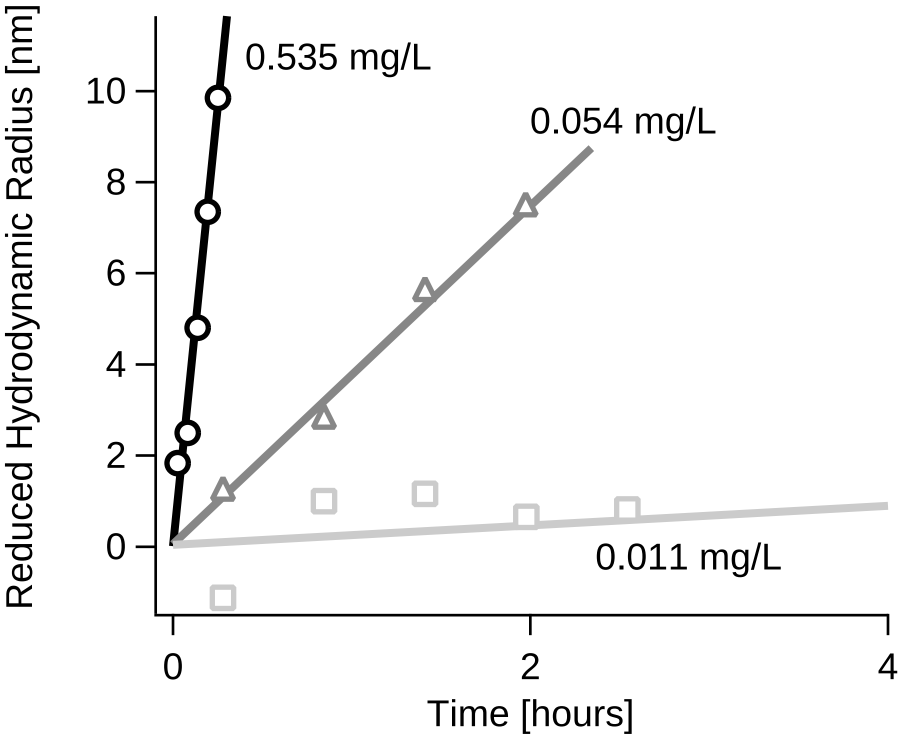

Figure 19: Optimization of initial particle concentration at 500 mM KCl. Initial particle size was subtracted from the measured hydrodynamic radii. Lines represent linear fits to block-averaged experimental data (markers).

already an acceptable value. In the next section we will show we can correct for this small contribution from the aggregation to the size increase, in order to obtain the net layer thickness.

Naturally, decreasing of the initial particle concentration also has its lower limits. Below 0.011 mg/L, the measurements of particle size (not shown) started to be difficult to reproduce. Low count rates (< 20 kHz) caused unreliable cumulant fits, which could be clearly seen on excessive standard deviations of experimental points from linear fits.

Optimization of initial particle concentration also serves as a check of our choice of model particles for layer thickness measurements. Our criteria for selection of particles were the following: (i) particles with regular spherical shape, (ii) low polydispersity, (iii) moderate surface charge, with the sign opposite to the charge of polyelectrolyte and (iv) small particle radius. While the first three conditions were easily fulfilled for the available latex particles, we had to make a compromise with the particle size. Ideally, the smaller would the particle be, the more pronounced would be the difference between the bare and coated particles. For the neutron scattering measurements (chapter 5), we used particles only 12 nm in radius. Unfortunately, it was not possible to use the same particle size for the light scattering measurements as well, since the optimization of particle concentration failed. Even if we decreased particle concentration slightly below the instrument detection limit, the increase of the apparent particle size due to aggregation was still too fast. Therefore, to slow down the aggregation, we had to choose similar particles with bigger radius. Table 6 summarizes the CCC and optimal concentration of all types of measured particles.

Adsorbed mass of polyelectrolyte

In the previous section, we have optimized the concentration of bare colloidal particles. The last step before proceeding to the layer thickness measurements is to find an appropriate concentration of polyelectrolyte with respect to the concentration of bare particles. If the polyelectrolyte concentration would be too low, average thickness of an adsorbed layer would be below the experimental noise. On the other hand, very high polyelectrolyte content might result to significant increase of the solvent viscosity and other undesired effects, such as bridging flocculation of particles.

Particles	Critical coagulation conc. [M]	Optimal particle conc. [mg/L]
sulfate latex	0.25	0.011
amidine latex	0.33	0.040

Table 6: Properties of bare particles: critical coagulation concentration (CCC) of KCl and optimal particle concentration at pH 4.

Measurements of electrophoretic mobility (principle reviewed in section 1.2) of colloidal particles in presence of oppositely charged polyelectrolyte can provide us with an information on the overall charge on the particle surface. In the following, we will discuss an example of negatively charged particles and cationic polyelectrolyte (fig. 20). By increasing the mass ratio of polyelectrolyte to particles, the overall particle charge increases due to adsorption, passing through an isoelectric point (IEP) where the surface charge of particle is completely compensated with the charge of the adsorbed polyelectrolyte layer. Due to overcharging effect [65], the uptake of polyelectrolyte on the particle surface does not level off at IEP, but continues up to saturation and causes the original negative particle charge to be reversed. The IEP dose (denoted with arrow in fig. 20) therefore separates range of polymer doses which result in unsaturated particle coating (lower plateau) and particles saturated with polyelectrolyte (upper plateau). In the following, the polyelectrolyte mass ratio used for the layer thickness measurements will be based on the dose at IEP, polyelectrolyte concentrations will be therefore expressed in terms of multiples of the dose at IEP.

As was experimentally verified [62], the polyelectrolyte dose at IEP does not depend on the concentration of salt. This feature permits us to use one value of dose at IEP also for measurements which are a function of salt concentration. A sample for electrophoretic mobility measurement with total volume of 10 ml was prepared by mixing of 0.1 mM HCl with latex particles in a plastic container. In the last step, diluted solution of polyelectrolyte was added and the sample was intensively stirred. Measurement started immediately after sample preparation. The final concentration of particles in sample was in the order of 10 mg/L. Prior to the measurements with polyelectrolyte we checked that the electrophoretic mobility does not change neither for 10 times smaller nor for 10 times higher particle concentrations. Table 7 summarizes polyelectrolyte dose at isoelectric point (IEP) for all investigated systems.

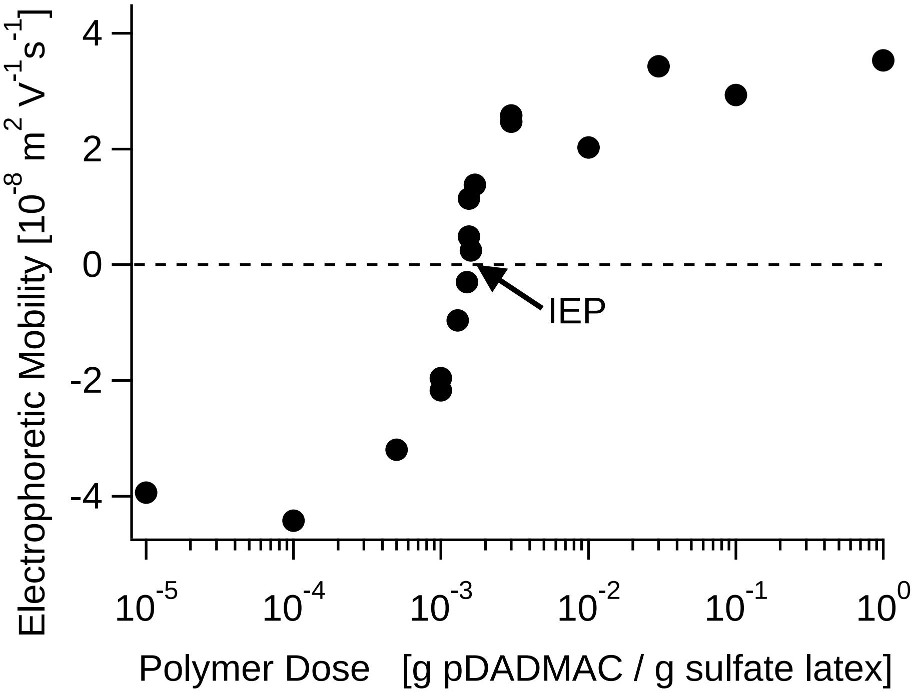

Figure 20: Electrophoretic mobility of sulfate latex particles as a function of polyelectrolyte dose. Isoelectric point (IEP, marked with an arrow) is reached at approx. 1.53×10^{-3} g PDADMAC/ 1 g sulfate latex. Dashed line indicates zero mobility.

Polyelectrolyte	Latex particles	Dose at IEP [mg/g particles]	Reference
PDADMAC	sulfate	1.5	this work
PVA32	sulfate	12	[65]
PVA94	sulfate	0.92	[65]
PSS (all)	amidine	6.3	[62]

Table 7: Polyelectrolyte dose at IEP measured by electrophoretic mobility.

Layer thickness measurement

Thickness of a polyelectrolyte layer on colloidal particles is determined as a difference between the particle size after and before adsorption of a polyelectrolyte. The first system we investigated was composed of the positively charged amidine latex particles and the negatively charged PSS. For this system we adapted an experimental procedure, which we further refer to as the "two-step method", since each single measurement was performed in two independent steps (samples). Later, we improved this method such that the entire measurement could be done only in one step, whereby we refer to the improved procedure as the "one-step method". The latter method was used for all discussed systems of particles and polyelectrolytes, except for the amidine latex with PSS.

The two-step method consists of two independent measurements. We first examined the bare particle size and in a different sample, we repeated this experiment with an addition of polyelectrolyte. To prepare the sample with bare particles, calculated amount of concentrated KCl solution (prepared at pH 4) was filled up to 1 ml with 0.1 mM HCl in borosilicate glass cuvette. Sample was then stirred with a vortex mixer and afterwards 1 ml of diluted suspension of colloidal particles was added. Particle concentrations in the measured sample were near 0.04 mg/L, that is 8×10^{12} particles/m^3. Cuvette was again stirred and immediately introduced to the measuring vat of the light scattering setup. Hydrodynamic radius was evaluated each 20 s from the second order cumulant fit of the correlation function and the collection of data took typically several hours.

Sample with polyelectrolyte was prepared and measured in a similar way, but before its introduction to the vat, small volume of polyelectrolyte solution was added gradually, under constant vortex stirring to ensure uniform polyelectrolyte distribution.

Typical record of a layer thickness measurement of the amidine latex + PSS system is sketched in fig. 21. Experimental noise of measured data points (grey circles) was reduced by block-averaging (black circles, arithmetic average was typically made out of 100 experimental points). Block-averaged points for bare particles are displayed as triangles, the original (non-averaged)

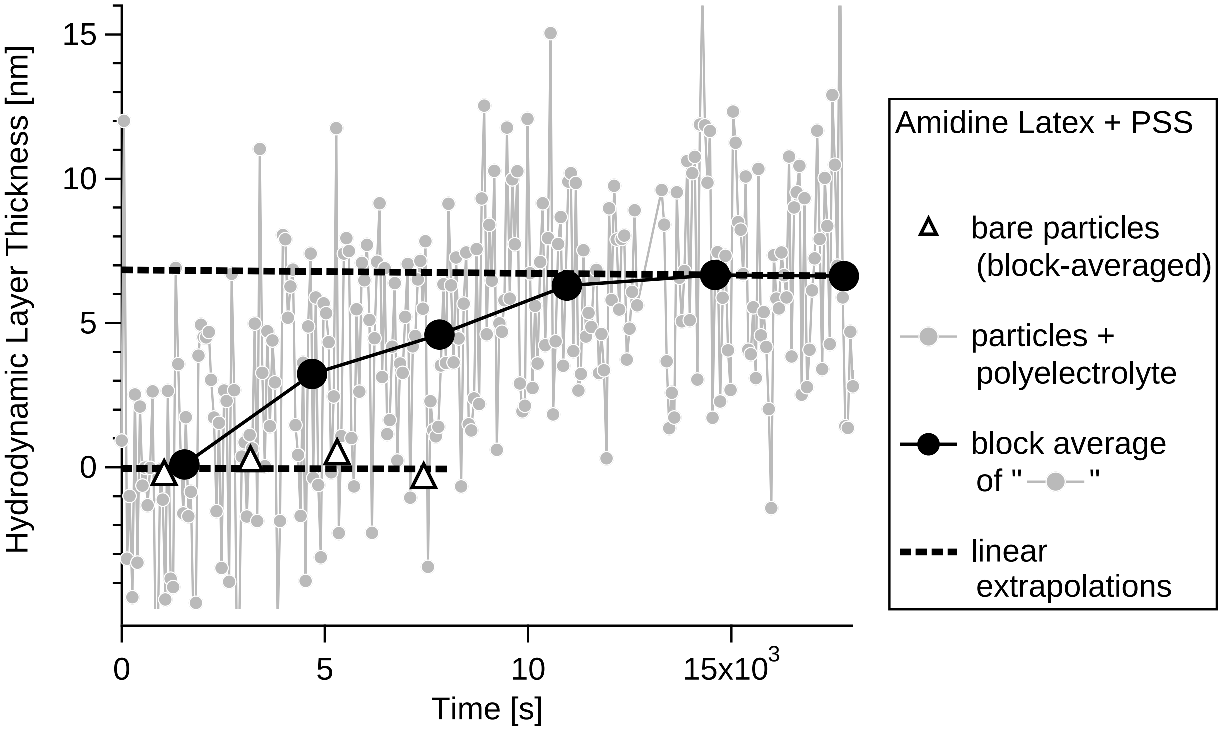

Figure 21: Typical layer thickness measurement with the two-step method.

points were omitted for clarity. Dashed lines are linear fits to experimental points for bare particles and coated particles, respectively. Points for the coated particles measured during the growth of the layer were excluded from the fit. Before plotting the data, we subtracted the extrapolated value of bare particle size at time zero from the vertical axis. In this way the extrapolation of the plateau points after polyelectrolyte adsorption shows on the vertical axis at zero time directly the hydrodynamic thickness of the polyelectrolyte layer.

The one-step method was used in most cases. For some colloidal particles it is possible to find experimental conditions, where the particle aggregation is below experimental noise. In our case, such conditions were realized for the amidine latex. However, since the decrease of particle concentration is restricted by the limits of measuring technique, for some other particles even at the best possible conditions, residual aggregation could still be observed. This was the case for the sulfate latex particles. While fast aggregation would make the layer thickness unmeasurable (cf. fig. 19, at 0.535 mg/L and 0.054 mg/L), residual aggregation (fig. 19, at 0.011 mg/L) can be accounted for, as we will show later.

In order to measure layer thickness in systems with residual aggregation present, we improved the two-step method as follows. Since with the improved method the experiment can be done in one step, we further refer to it as the ”one-step method”. In comparison with the two-step method, layer thickness measurement in one step has several advantages. First, particles with and without adsorbed polyelectrolyte are measured in one sample, which reduces influences of experimental errors. Second, time evolution of the hydrodynamic radius of the particles brings direct evidence that the steep increase of hydrodynamic radius of particles is related to the addition of polyelectrolyte. Finally, the one-step method saves material and offers shorter time for sample preparation.

Measurement of time evolution of hydrodynamic radius (fig. 22) started with a sample with bare particles, which was prepared in the same manner as for the two-step method. Once a sufficient number of data points were collected, experiment was interrupted for few minutes, the cuvette was removed from the vat and 20 μl of diluted polyelectrolyte solution was added, under vortex mixing. Hydrodynamic radius of particles was then monitored further and it was terminated several hours after the steep increase of particle size was ended.

An example of layer thickness measurement with the one-step method is shown in fig. 22. Experimental hydrodynamic radii (grey circles) were smoothed by block-averaging (black circles). We divided the time window of an experiment in the following three periods:

1. From time zero to the addition of polyelectrolyte (fig. 22) the measurement of the bare particles is carried out. Extrapolation of the linear fit

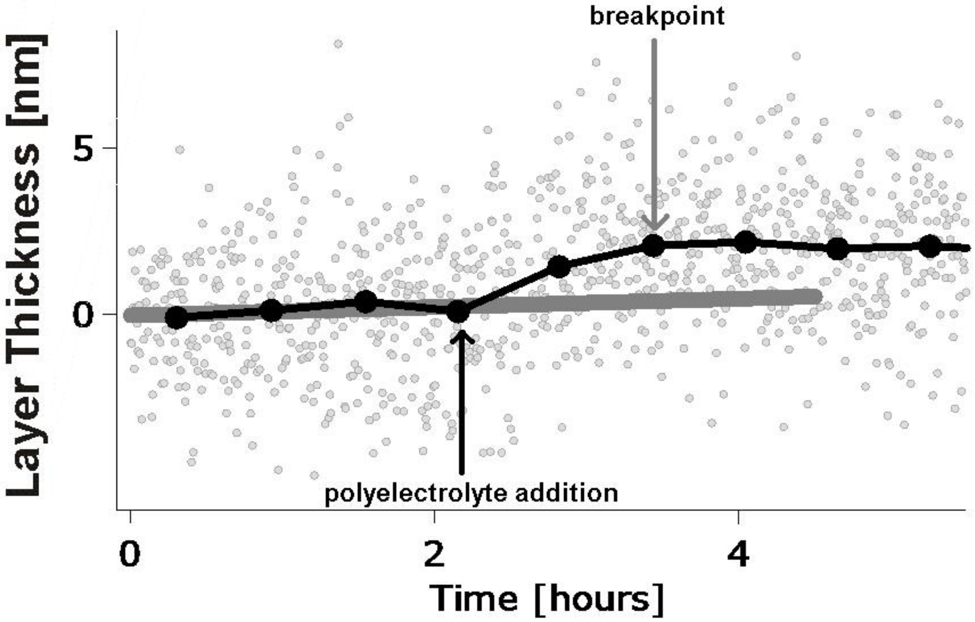

Figure 22: Typical layer thickness measurement with one-step method. Experimental points (grey circles) were block-averaged (black circles). Thick grey line is a linear fit to experimental points measured before polyelectrolyte addition, i.e. before the left-hand arrow points.

in this period of measurement serves as a baseline, which is accounting for residual aggregation, if present.

2. Addition of polyelectrolyte at the beginning of this period (fig. 22, black arrow) is followed by a steep increase of particle size due to buildup of a polyelectrolyte layer. We verified that the rate constant of the layer growth period was at least 1 order of magnitude larger than the one expected from fast aggregation.
3. After the breakpoint (fig. 22, grey arrow), the increase of particle size ends.

The resulting layer thickness is determined at the time of breakpoint between the second and third period (grey arrow in fig. 22). Layer thickness is a difference between the extrapolated bare particle radius and the radius at

investigated effect	particles	polyelectrolyte
dose	sulfate latex	PDADMAC
charge	sulfate latex	PVA32, PVA94
molecular mass	amidine latex	PSS29k, PSS323k, PSS2260k

Table 8: Summary of layer thickness measurements

the breakpoint. Note that the evaluation of layer thickness with the two-step method was a special case of evaluation procedure used for one-step method, when the slope of the linear fit to the radii of bare particles was zero.

4.4 Results and discussion

General trends in layer thickness

We investigated layer thickness of three different systems of colloidal particles and polyelectrolytes. Positively charged strong polyelectrolyte (PDADMAC) was adsorbed on negatively charged sulfate latex particles with pH-independent charge. Another examined system was composed of negatively charged sulfate latex particles with pH-independent charge, and two types of adsorbed positively charged weak polyelectrolytes, differing in ratio of charged/uncharged groups (PVA32 and PVA94). Finally, positively charged amidine latex particles, which charge was almost pH-independent, were investigated with three types of negatively charged strong polyelectrolytes with various molecular masses (PSS29k, PSS323k, PSS2260k). We summarize the measured systems and investigated effects on layer thickness in table 8.

Despite the diversity in properties of used materials, we can observe some general trends for all investigated systems of particles and polyelectrolytes. The thickness of an adsorbed polyelectrolyte layer was in the range of (0 to 7.6) nm. Maximum value of thicknesses for all three electrolytes were very close, namely 7.1 nm for PSS2260, 7.1 nm for PDADMAC, and 7.6 nm for PVA32. This point was despite the great variance in charge, molecular mass and electrochemical character of ionizable groups on adsorbed polyelectrolytes. Reliable values of layer thicknesses were observed at polyelectrolyte concentrations 10×IEP and higher. Although the layer thickness around 1×IEP is probably still not negligible, due to the qualitatively different behavior the presented method cannot give reliable results, as we will discuss further. Layer thicker than 1 nm developed in solutions with ionic strength 10 mM and higher. Without addition of salt, no significant thickness could be observed. Monotonous growth of layer with increasing concentration of KCl was found for all polyelectrolytes. While the thickness leveled off at about 50 mM salt for the two PVAs, maximal thickness with PSS was achieved at 100 mM and for the case of PDADMAC, the upper plateau seems still not to be reached at 100 mM. The different behavior can be rationalized by different stiffness of polymer chains. Among the three investigated polyelectrolytes (cf. fig. 17), only the PVA does not have voluminous carbon rings. Moreover, charged units are separated with neutral ones, which can also have an effect on lower chain stiffness. Therefore, smaller concentration of salt is necessary to screen intramolecular repulsions in PVA, favoring creation of loops and tails which makes the hydrodynamic thickness higher. As a conclusion, among the three polyelectrolytes, PVA reaches maximal thickness at the lowest salt.

Effect of viscosity on diffusion coefficient

Hydrodynamic radius of particles was calculated from diffusion coefficient, using Stokes-Einstein equation (eq. 2). For the calculation, viscosity of pure water was used for all measurements. We neglected the decrease of viscosity upon addition of KCl, since even for the highest KCl concentration used (0.5 M) the error introduced to particle size calculation is below 0.5% (based on viscosity data from [67]). If the addition of polyelectrolyte would have a significant effect on the solvent viscosity, an abrupt change of calculated particle radius upon polyelectrolyte addition would have to be observed. In fact, this was never the case, even at highest polyelectrolyte dose (5×10^{-4} g/L) the particle radius before and immediately after polyelectrolyte addition stayed, within experimental error, the same.

Scattering from polyelectrolyte

Most of the layer thickness measurements were done at high excess of polyelectrolyte, up to 1000× the dose at isoelectric point. Polyelectrolyte molecules, which are present free in solution, in principle contribute to the intensity of scattered light. Nevertheless, due to several orders of magnitude difference between molecular mass of particles and polyelectrolyte, the effect on intensity-weighted diffusion coefficient can be neglected. Thus, for light scattering the polyelectrolyte chains are only visible as adsorbed layer hindering the diffusion of particles.

Effect of salt on bare particle size

In a first approach, measurement of bare particle size could be performed for a certain type of particles only once, and then used for all experiments. To measure the initial particle radius in each single layer thickness experiment size is in fact of high importance, especially at higher salt concentrations. With increased amount of added KCl we observed slight shrinkage of bare particles, which was most probably due to the soft character of the polystyrene latex spheres or owing to presence of a thin soft hairy layer on particle surface (cf. hairy layer on silica particles in section 2). As discussed above, the reduction of particle size due to effect of added salt on the viscosity of solvent is unprobable. The shrinkage was not higher than 3% of size in salt-free solution, or (2–3) nm. By using the appropriate base line (inital particle size) for each experiment, the shrinkage effect on the layer thickness determination was eliminated.

Effect of polyelectrolyte dose on layer thickness

Fig. 24 shows the thickness of PDADMAC layer on sulfate latex particles as a function of polyelectrolyte dose, for three different concentrations of salt. In the whole range of plotted polyelectrolyte doses the layer thickness is insensitive to the increasing concentration of polyelectrolyte, and clearly depends on concentration of KCl. We note substantial scattering of data points, especially at 100 mM salt, which could be attributed to broad distribution of molecular masses of used PDADMAC. The final adsorbed layer thickness might be a result of a competition between smaller and longer chains, which could explain more complex behavior. On average, in the range of $\geq$10×IEP, layer thicknesses reached 0.4 nm, 1.7 nm and 4.8 for 0 mM, 25 mM and 100 mM added KCl concentration, respectively.

Although doses $<$10×IEP were investigated as well, layer thickness in this range could not be inferred due to qualitatively different time course of hydrodynamic radius of particles after addition of polyelectrolyte (fig. 23.). While for the data points in the range $\geq$10×IEP the breaking point after polyelectrolyte addition was evident, within a typical time window the measurements of hydrodynamic radius in range $<$10×IEP showed no plateau; on contrary, the radii continued to grow with unchanged slope. It is known that due to neutralization of charge at doses around 1×IEP, particles will undergo fast aggregation [62]. However, as we have shown above, the experimental conditions ensure that the fastest (diffusion limited) increase of measured particle size due to particle aggregation is much slower than the increase due to polyelectrolyte adsorption. The untypical time course of hydrodynamic radius should be a subject of further investigations.

A very simple calculation can give us an idea on the particle surface coverage, assuming that 100% of PDADMAC mass from the solution is adsorbed. If we divide surface of the sulfate latex particle with square of contour length of PDADMAC monomer unit (0.42 nm^2, [68]), we need $\approx$ 100 molecules of PDADMAC (450 kg/mol) to form a compact monolayer (100% coverage). At

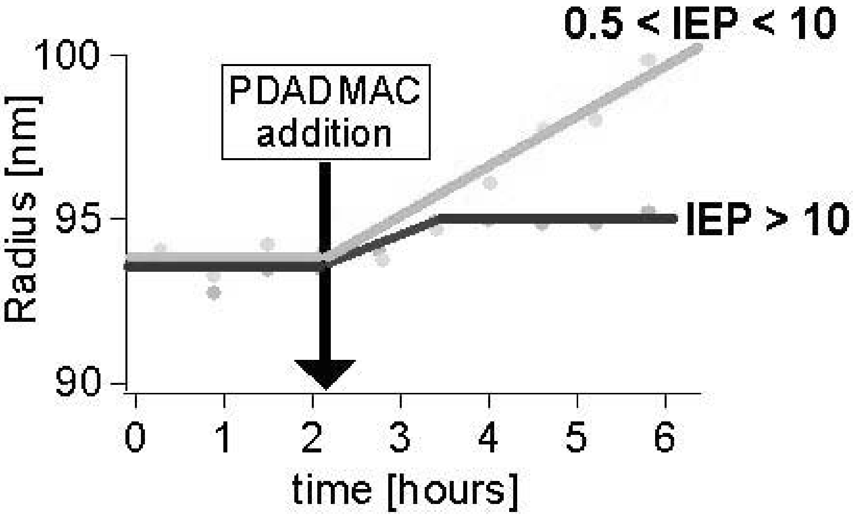

Figure 23: Time course of hydrodynamic radius for measurements at concentrations <10×IEP and ≥10×IEP.

1×IEP dose of PDADMAC, only 8 molecules of PDADMAC (450 kg/mol) are necessary to compensate the charge of one particle, thus covering only 8% of available particle surface. However, at concentrations above 1×IEP the surface coverage might be considerably higher, owing to the overcharging effect [65].

Dependence of hydrodynamic layer thickness on concentration of salt shows fig. 25. Increasing concentration of KCl screens the repulsion between polyelectrolyte segments, such that the polyelectrolyte behaves partially as an uncharged polymer. The latter favors creation of more loops and tails, which decrease the diffusion coefficient of particles, which indicates thicker layer.

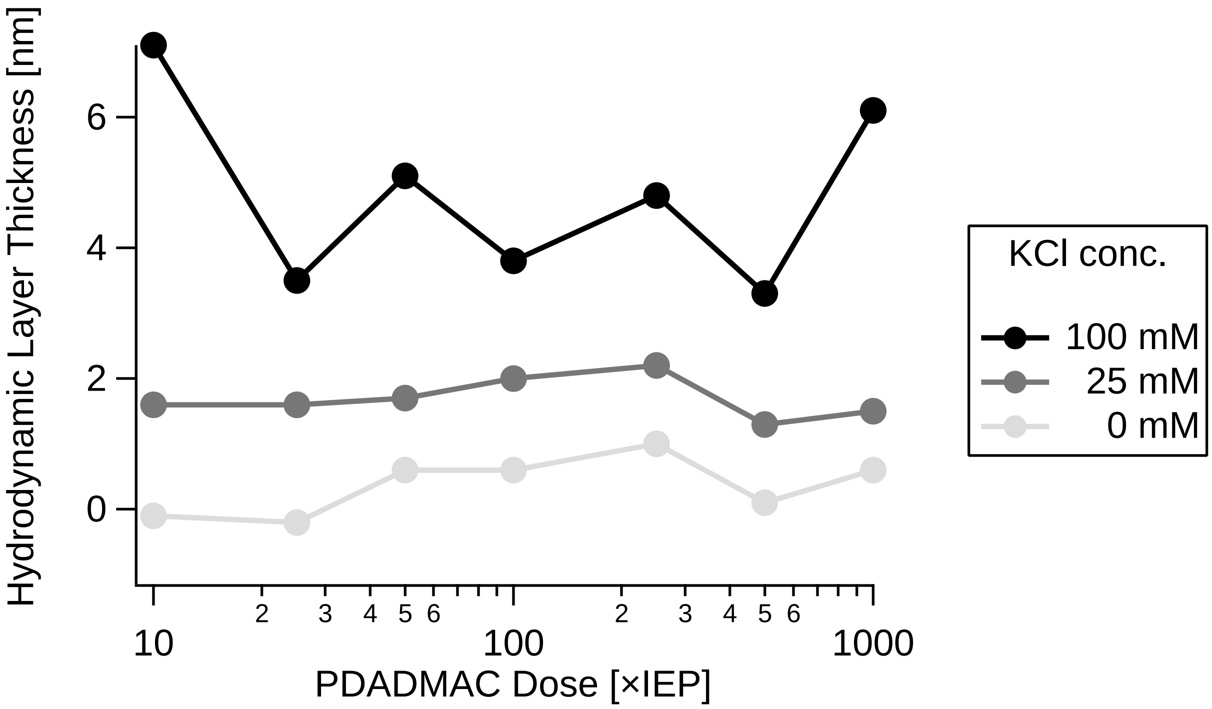

Figure 24: Hydrodynamic layer thickness as a function of polyelectrolyte dose. Lines are for eye guiding only. Concentration of PDADMAC is expressed in multiples of dose at isoelectric point (IEP).

Effect of polyelectrolyte charge on layer thickness

Despite the three fold difference in charge density of the two types of PVA, the layer thickness as a function of concentration of KCl is very similar (fig. 26). Theoretically, the lower is the charge on polyelectrolyte, the weaker are the electrostatic interactions of polyelectrolyte with the particle surface charge. Weaker interactions favor formation of tails and loops and so the hydrodynamic layer thickness should be higher. We suggest two reasons for the observed discrepancy: (i) At the experimental conditions we used, the two PVAs actually have the same ratio of charged (amine) and uncharged (formamide) groups and thus behave the same way. (ii) Interactions of the different two PVAs with particles are different, but this only results in change of the layer structure, while the hydrodynamic thickness remains the same.

The first explanation is based on the fact that both polyelectrolytes were prepared by incomplete hydrolysis of a precursor polymer, which was con-

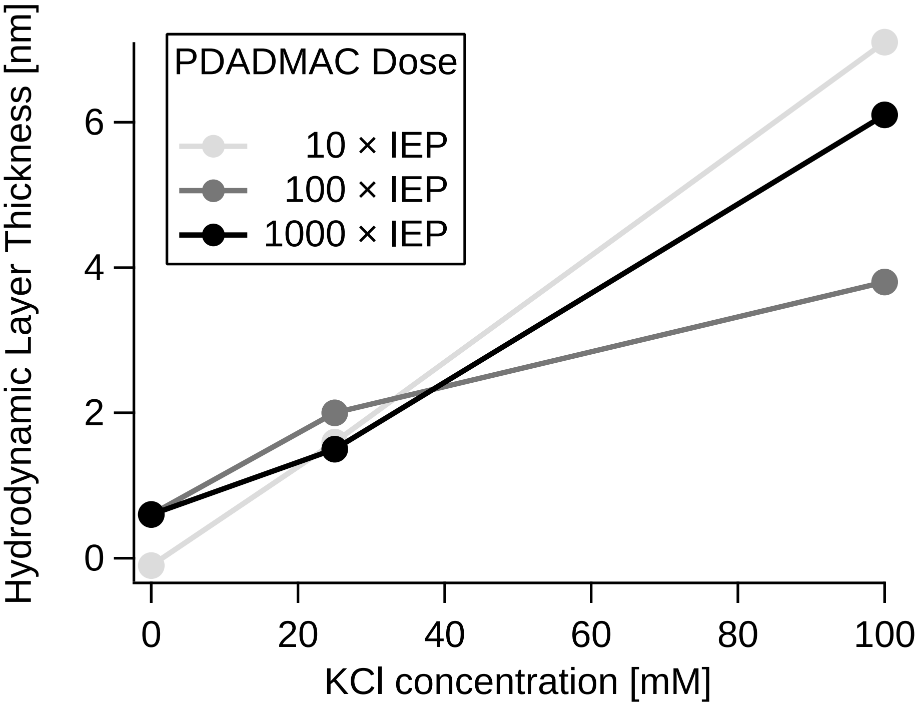

Figure 25: Hydrodynamic thickness of PDADMAC layer on sulfate latex particles as a function of salt. Lines are to guide the eye only.

taining only formamide groups, according to equation

$$-\text{NH-CHO} + \text{H}_3\text{O}^+ \rightleftharpoons -\text{NH}_2 + \text{HCOOH} \tag{19}$$

By increasing the concentration of H_3O^+, the equilibrium is shifted towards the $-NH_2$ groups. Although the reaction 19 is qualitatively possible, it would need much lower pH to have a non-negligible yield. Therefore, we strongly favor the second explanation, which suggests that the PVA32 and PVA94 layer are different in structure, but not in thickness. This explanation is based on the electrophoretic mobility measurements of polyelectrolyte dose at isoelectric point (tab. 7), which showed that there is more than 10 fold difference between the adsorbed mass of PVA32 and PVA94. Less charged polyelectrolyte is more prone to looser adsorption, forming tails and loops

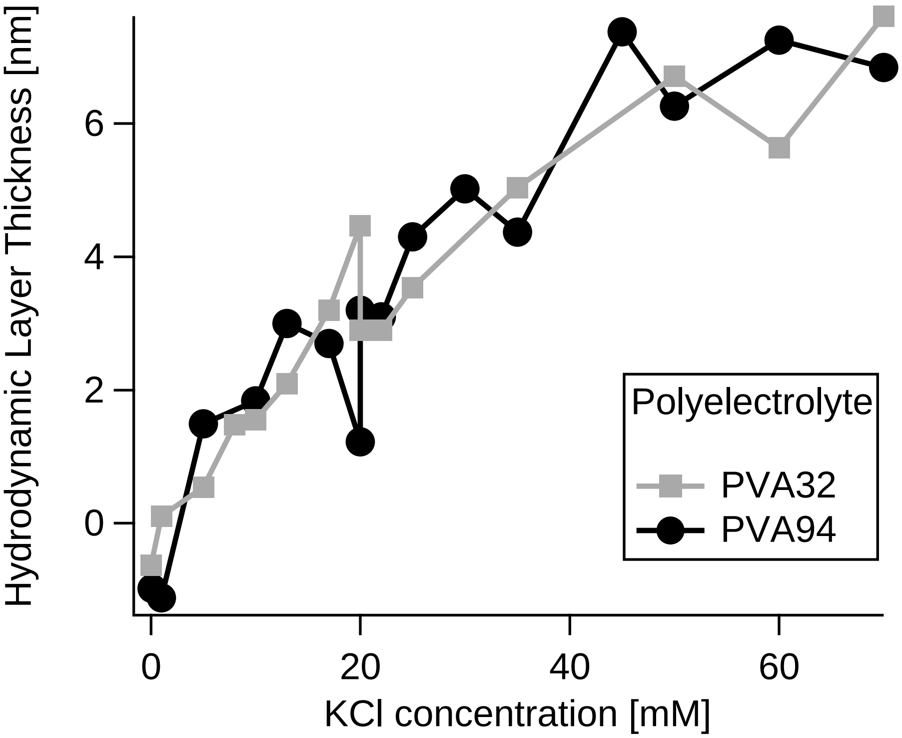

Figure 26: Hydrodynamic layer thickness as a function of salt concentration for different types of PVA. Lines are for eye guiding only. Measurements were performed at pH 4, at which more than 90% -NH_2 groups are protonated.

which decreases the effectivity of PVA32 to neutralize the particle charge and therefore higher mass is necessary to reach the IEP.

Effect of polyelectrolyte molecular mass on layer thickness

Molecular mass is one of the most important characteristics of a polyelectrolyte, since it has a substantial effect on many of the polyelectrolyte properties. In this section, we aim to investigate the effect of polyelectrolyte molecular mass on its layer thickness, as a function of polyelectrolyte dose and concentration of salt.

Fig. 27 shows dependence of hydrodynamic thickness of PSS layer adsorbed on amidine latex particles at 300 mM KCl. Three different molecular masses of PSS were investigated, namely (29, 323 and 2260) kg/mol, as a

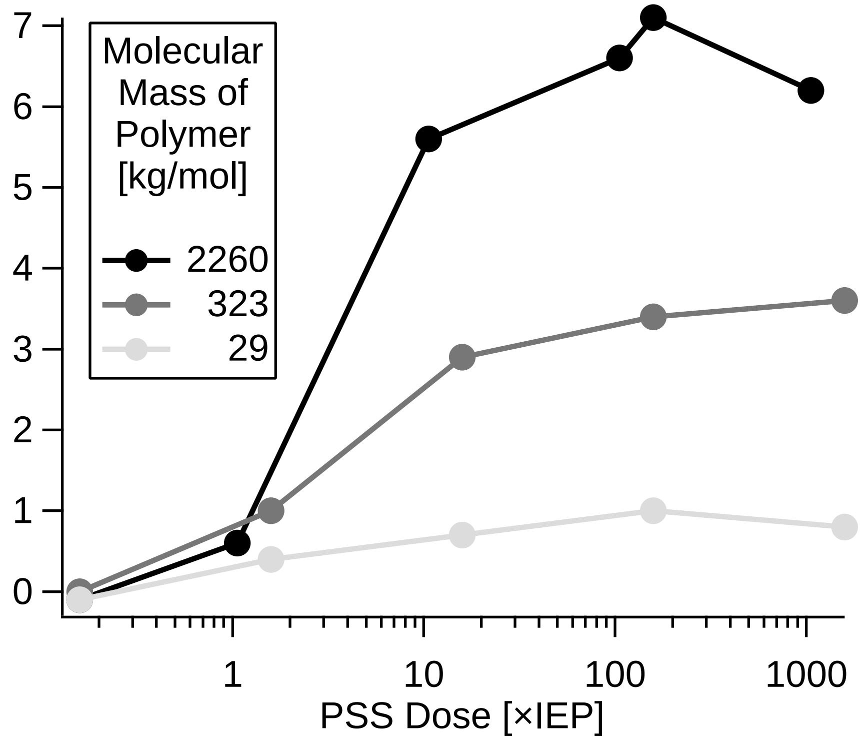

Figure 27: Hydrodynamic layer thickness as a function of polyelectrolyte dose for different molecular masses of PSS, at 300 mM KCl and pH 4. Lines are for eye guiding only. Concentration of PSS is expressed in multiples of dose at isoelectric point (IEP).

function of polyelectrolyte dose at pH 4. Concentration of PSS is expressed in terms of multiples of doses at isoelectric point (see table 7). Layer grows with increasing PSS dose and levels off at about 100×IEP concentration. This observation was already made on the basis of electrophoretic mobilities (section 4.3), which has shown that with increasing polyelectrolyte concentration the adsorbed mass is increasing. Approximately at 100×IEP dose the plateau for electrophoretic mobility measurement is reached.

The increasing layer thickness with increasing polyelectrolyte molecular mass can be rationalized by different conformations of adsorbed polyelectrolyte chains [7]. While short chains prefer to adsorb in a train-like conformation (fig. 2), with increasing chain length formation of loops and trains is still more favored. Since the hydrodynamic radius of coated particle is sensitive to the presence of loops and trains, we can observe an increased layer thickness for polyelectrolytes with higher molecular masses.

Dependence of layer thickness on concentration of KCl for different molecular masses of PSS at pH 4 is shown in fig. 28. Dose of PSS was fixed at 100×IEP for all curves. At low ionic strengths, the layer remains very thin. Observable layer develops only above 10 mM salt, then it steeply increases and reaches a plateau value around 100 mM.

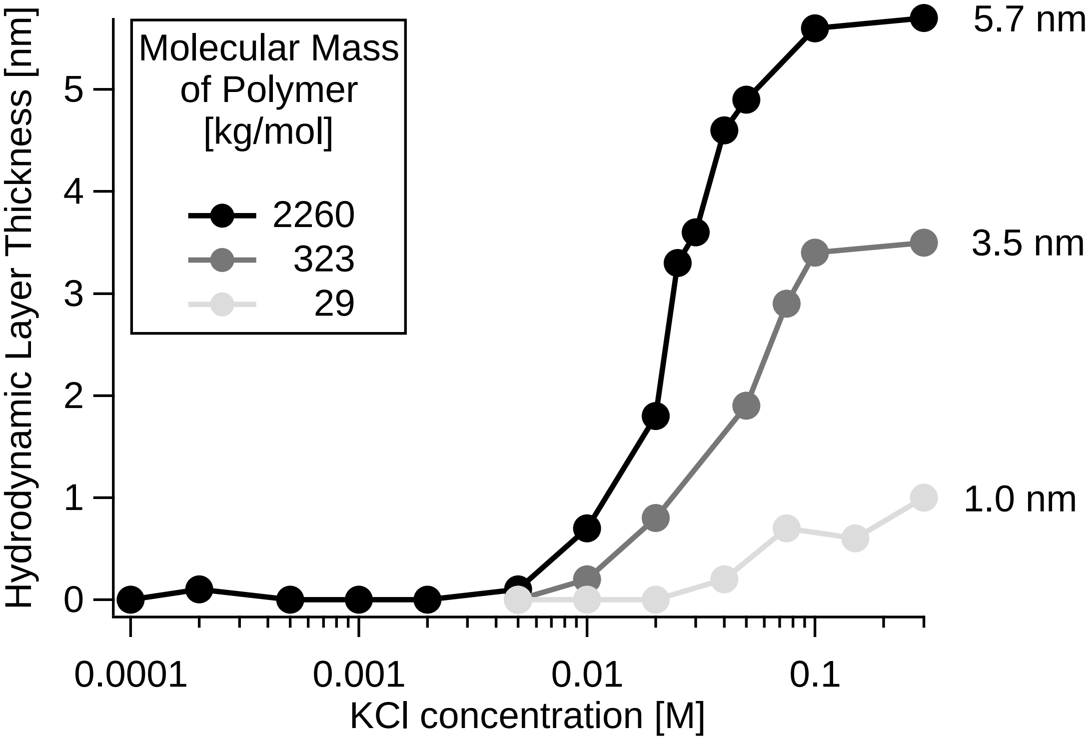

Figure 28: Hydrodynamic layer thickness as a function of salt concentration for different molecular masses of PSS, at pH 4. Lines are for eye guiding only. Numbers on the righthand side denote maximal measured thickness for given molecular mass.

We can explain the effect of increasing ionic strength by analyzing electrostatic interactions in play. Addition of background electrolyte (KCl) screens both types of interactions present: (i) repulsion between charges on polyelectrolyte segments and (ii) attractive interactions between oppositely charged polyelectrolyte and particle surface. At low salt, intramolecular charge repulsion favors the polyelectrolyte chains to adapt a rigid rod-like conformations. As the chains are stretched, they tend to adsorb in mostly in a flat train conformations and thus form thin layer. On the other hand, at high salt concentrations, both repulsive and attractive interactions are screened. Decreased intramolecular repulsion allows polyelectrolyte to became more coiled and at the same time the attractive chain-surface interactions are weaker, which gives rise to the formation of more loops and trains; thus the layer gets thicker.

In addition to the three types of PSS shown in figs. 27 and 28 we also examined layer thickness of PSS with molecular mass of 2.2 kg/mol. Although the electrophoretic mobility measurement of the 2.2 kg/mol PSS dose at isoelectric point (not shown) was very similar with the other three PSS, no layer could be detected with dynamic light scattering. We therefore suppose, that although the layer was present, it was very compact and its thickness was below the detection limit of our technique, owing to relatively very short polyelectrolyte chains.

4.5 Conclusion

We have presented a method for measurements of hydrodynamic layer thickness of a polyelectrolyte layer adsorbed on colloidal particles. The method is especially suitable for thin layers, with hydrodynamic thickness in range (1 to 10) nm, since it strictly separates the contribution of particle aggregation to the observed increase of particle size upon polyelectrolyte addition. Neglect of the aggregation could be a reason for which in some previous studies thickness in the order of tens of nanometers was reported for a polyelectrolyte monolayer on colloidal particles.

Despite a great variance in used particles and polyelectrolytes, we observed qualitatively similar trends in hydrodynamic layer thickness for all investigated systems. Polyelectrolyte layer thickness increases with (i) higher molecular mass of polyelectrolyte, (ii) increasing concentration of polyelectrolyte and (iii) raising concentration of background electrolyte (KCl).

Presented results of hydrodynamic layer thickness will be compared in the next section with layer structure inferred from small angle neutron scattering (SANS) measurements. In the future, we could examine adsorption of polyelectrolytes on oppositely charged particles, which surface was before overcompensated by divalent counterions (cf. chapter 3).

5 Characterization of an adsorbed polyelectrolyte by neutron scattering

5.1 Introduction

As was shown in the previous chapter, the surface of a substrate can be significantly modified by adsorption of an oppositely charged polyelectrolyte. Knowing the structure of the adsorbed polyelectrolyte layer is thus of substantial importance if one wants to be capable to predict and to vary the properties of a polyelectrolyte-coated surface. One important application are multilayered assemblies, which can be obtained by adsorbing positive and negatively charged polyelectrolytes in an alternating fashion [130]. For example, this method has been employed to produce hollow capsules by adsorption of a sequence of layers, which is followed by dissolution of the inner core.

Small angle neutron and X-ray techniques represent one of the promising techniques to gain insight into the structure and profile of the adsorbed polymer layer. These techniques have been mostly applied to neutral adsorbed polymers [123–129]. Small angle neutron scattering (SANS) has been also used to gain insight into the structure of adsorbed polymer layers on colloidal particles [79,80,131]. Dynamic light scattering can be used to monitor the thickness of a layer by following the change in the mean size due to the presence of an adsorbed layer. However, light scattering responds best for length scales, which are normally larger than the typical thickness of a layer and therefore severe experimental conditions are required to avoid colloidal aggregation (cf. chapter 4).

While multilayers of polyelectrolytes on colloids have been studied in much detail, little is known about the first layer, which might not necessarily be identical to the other layers of the multilayered assembly. The reason for such a lack of data is probably due to fact that such a layer is thin and not tenuous. While for thick layers it is rather straightforward to extract the profile of an adsorbed layer, for thin layers this approach is hampered by the fact that the weak scattering of the layer is overshadowed by the strong scattering originating from the particles. One approach is to study thick and dense polyelectrolyte brushes, as done by Mir et al. [79]. They employed the strategy of covalently grafting a polymer in organic solvent, which was then chemically transformed into charged brushes. This route led to rather thick layers whose profile turned out to extend over tens of nanometers into water and they were found to shrink upon addition of salt. This study is, to our knowledge, the only one that has focused on the properties of an adsorbed monolayer of a polyelectrolyte.

This chapter describes an attempt to obtain the structure of a single adsorbed polyelectrolyte layer. SANS was employed to measure layer thickness of PDADMAC adsorbed on oppositely charged sulfate terminated latex particles. The essence of this approach is that the particles used are deuterated, thus being basically invisible to the neutrons in heavy water. In this fashion, the thin layer becomes visible and can be studied. The existence of a very thin but rather dense layer is thus demonstrated.

5.2 Materials and methods

Deuterated sulfate terminated latex particles used in the SANS experiments obtained from Interfacial Dynamics Corporation (IDC, Portland, USA) had a mean radius of 12 nm and a polydispersity characterized by a coefficient of variation $c_v = 0.14$, as determined by transmission electron microscopy (TEM) by the manufacturer. The hydrodynamic radius measured by dynamic light scattering was found to be equal to 13 nm. Such a value is higher than the number averaged radius obtained with TEM, due to non-negligible polydispersity of the sample. Surface charge density was determined by conductometric titration to be equal to 6 mC/m^2 by the manufacturer. The concentration of the stock solution was 3.9% (w/w). The polyelectrolyte used was poly(diallyldimethyl ammonium) chloride (PDADMAC), the same sample as used in the previous chapter (cf. section 4.2). The particles were dialyzed against D_2O 99% for two times followed by a last dialysis with D_2O 99.95%. Residual H_2O still present after dialysis was quantified by nuclear magnetic resonance. The residual water content of the final particle suspension was found to be 3.5% in weight.

Small angle neutron scattering measurements were performed at SINQ (PSI, Villigen, Switzerland) on the SANS-II beamline. Quartz cuvettes (Hellma, 110-QS) of 2 mm thickness were used in all the experiments. Measurements were performed in a range of the magnitude of the scattering vectors q between 0.05 nm^{-1} and 2 nm^{-1} at two sample-detector distances of 0.97 m and 5 m, using a neutron wavelength of $\lambda = 0.6369$ nm. All measurements were carried out at room temperature. The samples were directly prepared in the cuvettes at a concentration of deuterated latex particles of 3% in weight. Bare particles were measured in 1.5 mM KCl solutions in H_2O/D_2O mixtures of various relative composition. These suspensions remained stable and transparent, as particle aggregation was prevented by the strong electrostatic repulsion between the particles. Particles with adsorbed PDADMAC were prepared by mixing the particle suspension with PDADMAC stock solution of 5% in weight. Mixing was promoted by stirring with a homemade Teflon paddle, until a homogeneous gel-like texture was obtained. In these conditions, the particles aggregate in spite of the addition of the high polymer dose. This phenomenon can be understood considering that, to achieve charge reversal, the suspension has to pass through isoelectric point. Here the aggregation is extremely rapid at such particle concentrations since particles bear no charge. The scattering intensities were isotropically averaged and corrected for transmission and background as described elsewhere [132].

The particle charge was addressed by electrophoretic mobility measurements performed on a laser Doppler velocimetry set-up (see section 4.2) as a function of PDADMAC dose. In these experiments, the concentration of latex particles was 1.2×10^{-4} (w/w) and the ionic strength of the suspension was

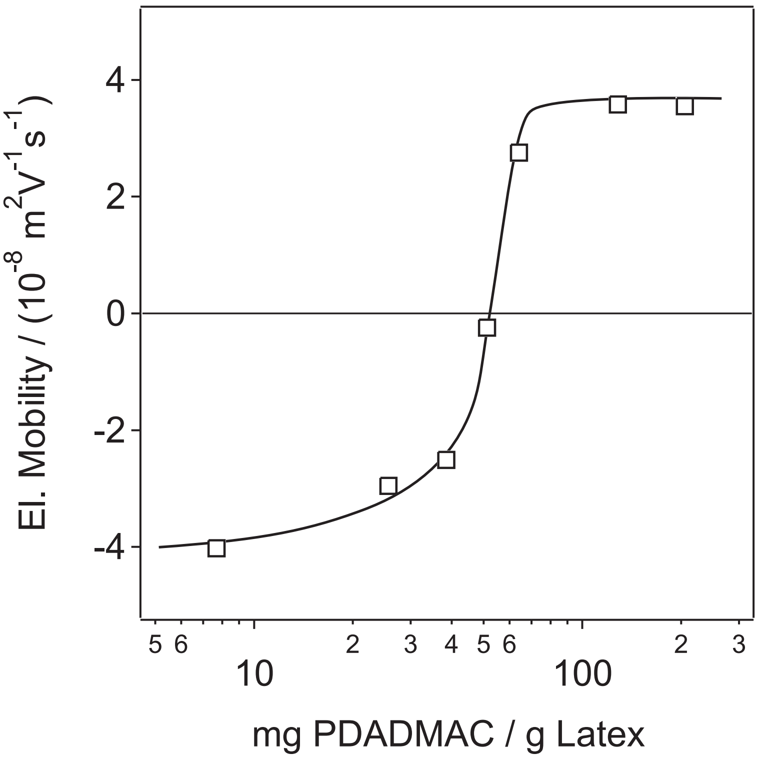

Figure 29: Electrophoretic mobility of deuterated sulfate latex particles as a function of PDADMAC dose. Line is for eye guide only.

10 mM in KCl medium and pH adjusted to 4 with HCl. The electrophoretic mobility is shown as a function of PDADMAC added dose in fig. 29.

The figure shows charge reversal of the particles through PDADMAC addition. The mobility of the particles gradually increases due to adsorption of the positively charged PDADMAC to the negatively charged latex particles. The isoelectric point (IEP) occurs at a polymer to latex mass ratio of 50 mg/g. At larger doses of PDADMAC, the sign of the mobility is reversed and switches to positive values. By further addition of PDADMAC, the mobility keeps unchanged indicating that a saturation polyelectrolyte layer has formed.

5.3 Results and discussion

The approach used to characterize an adsorbed layer on colloidal particles by means of SANS is that of contrast variation. In this technique one attempts to match the scattering length density of the solvent to that of the particles. Indeed, a low contrast between particles and solvent causes the scattering pattern to be dominated by the contribution of the adsorbed layer. At the same time, one should attempt the scattering background. Moreover, due to the kind of convolution relationship existing between the physical characteristics of the system and the measured quantity in a SANS experiment, it is beneficial to perform experiments at varying contrasts. As a matter of fact, the ability to fit a model, which describes the system to a series of experiments at increasing contrasts yields unambiguous evidence of its validity. In our case, it was found that suspensions of deuterated polystyrene particles (PS) in H_2O/D_2O mixtures was a combination which allowed to use the contrast variation technique, whereby contrast variation is achieved varying the relative amount of H_2O in D_2O. We should note, however, that in such system a complete particle contrast match cannot be achieved.

In order to properly interpret PDADMAC on deuterated PS experiments we first have to be able to properly model the contribution of the deuterated PS core. The reason for this is two-fold. First, we have to ascertain that the lowering the particle contrast does not expose inhomogeneities in the scattering density of the particles. Clearly, neglecting such contribution would make the interpretation of the corresponding experiments in the presence PDADMAC difficult. Second, the series at different contrasts yield information about the particle size distribution (PSD) that, once obtained, can be factored out from the fitting of the series of experiments on the deuterated PS/PDADMAC system.

To be able to analyze the bare particle experimental results, we first proceed to discuss the underlying theory of SANS for a collection of spheres. The differential scattering cross-section of a polydisperse colloidal suspension containing spherically symmetric particles can be expressed as [133]

$$\frac{\mathrm{d}\sigma}{\mathrm{d}\Omega} = N_0 \int n(R) V_p^2(R) \overline{\Delta\rho}^2(R) P(q,R) S(q,R) \mathrm{d}R + \frac{\mathrm{d}\sigma_{\mathrm{inc}}}{\mathrm{d}\Omega}, \tag{20}$$

where $n(R)$ is the fraction of the particle population having a radius R and a volume $V_p(R)$, N_0 is the particle number concentration, $P(q,R)$ is the form factor, $S(q,R)$ the structure factor, $d\sigma_{\mathrm{inc}}/d\Omega$ the contribution due to incoherent scattering, and $\overline{\Delta\rho}^2(R)$ is the volume weighted difference in scattering length density between the particle and the solvent:

$$\overline{\Delta\rho}^2(R) \equiv \frac{\int_0^R 4\pi r^2 (\rho_p(r) - \rho_s) \mathrm{d}r}{V_p(R)}, \tag{21}$$

with $\rho_p(r)$ and ρ_s the scattering length densities of the particles and the solvent, respectively. The form factor accounts for the single particle contribution to the total scattering, and can be written as $P(q,R) = F^2(q,R)$, where $F(q,R)$ is the scattering amplitude. In case of an homogeneous sphere, we have $F(q,R) = F_0(q,R) \equiv 3j_1(qR)/qR$ where $j_1(x) = (\sin x - x\cos x)/x^2$ is a spherical Bessel function of the first kind and order one. The structure factor was approximated in terms of hard spheres [134]. As the particles bear a net charge, the use of such a form factor would be strictly speaking incorrect. However, treating the hard sphere radius and the hard sphere volume fraction as free parameters in the fitting procedure has been shown to be effective to empirically correct such an inconsistency [135]. In the numerical implementation we have expressed the two aforementioned quantities as their "physical" counterpart mutiplied by two factors: α_R for the hard sphere radius and α_ϕ for the hard sphere volume fraction. Sample polydispersity was taken into account by assuming a Gaussian distribution with an average radius and a coefficient of variation, c_v both adjusted to the TEM values reported above. The smearing due to the finite wavelength resolution of the instrument was approximated by convoluting the calculated scatter-

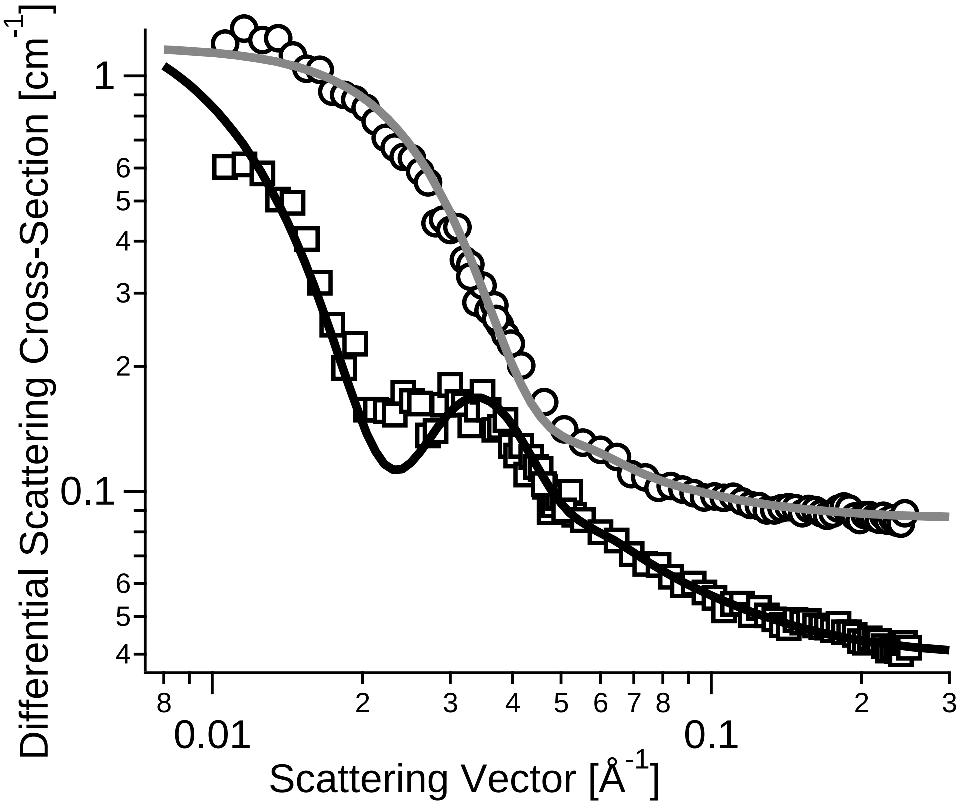

Figure 30: Measured SANS differential scattering cross-section for the bare particles (markers) at water content in weight of 3% (squares) and 8% (circles) with corresponding fits (see text).

ing profile with a Gaussian distribution with a coefficient of variation set to 0.134.

Figure 30 shows the differential scattering cross-section $d\sigma/d\Omega$ [cm^{-1}] of the bare latex particles for the two lowest water contents measured in 1.5 mM KCl (circles: 8% water weight fraction, squares 3% water weight fraction). We notice that by increasing the relative amount of water, the scattering from the particles increases because of the increased contrast between particles and surrounding medium. Fitting the experimental data to eq. 20 with the form factor of a sphere was however possible only for the higher contrasts. This point indicates that by lowering the contrast of the particles we expose the inhomogeneities in the scattering length density within the particles. As

Table 9: Fitting parameters of the core-shell model for the SANS measurement at 3% and 8% water content in weight with the bare particles.

h_1 [Å]	$\rho_s(8\%)$ [Å^{-2}]	$\rho_s(3\%)$ [Å^{-2}]	ρ_1 [Å^{-2}]	α_R	α_ϕ	$\beta(8\%)$	$\beta(3\%)$
9.90	5.03×10^{-6}	6.11×10^{-6}	2.07×10^{-6}	0.356	1.14	0.200	0.211

mentioned before, it is then crucial to properly describe such behavior if we want to be able to interpret the adsorption measurements later on. To accomplish this, we assumed the existence of an outer shell (of constant thickness) in the particles where the scattering length density is different from that of deuterated PS. In this situation, the scattering amplitude can be expressed as

$$F_1(q,R,h) = \frac{V_p(R_1)F_0(q,R_1)(\rho_p-\rho_1)+V_p(R)F_0(q,R)(\rho_1-\rho_s)}{V_p(R_1)(\rho_p-\rho_1)+V_p(R)(\rho_1-\rho_s)}, \tag{22}$$

where ρ_1 is the scattering length density of the outer shell, and $R_1 = R - h_1$ is the internal radius with h_1 the thickness of the shell. We then fitted the two lowest contrast measurements leaving as fitting parameters the shell thickness, h_1, its scattering length, ρ_1, the two hard sphere parameters, α_R and α_ϕ, the two scattering length densities, $\rho_s(8\%)$ and $\rho_s(3\%)$ of the solvent at 8% and 3% water content, respectively, and two factors, $\beta(8\%)$ and $\beta(3\%)$, which are multiplied to the coherent contribution to the scattering in order to account for experimental uncertainties in the number of particles present in the sample. A value of $6.47\times10^{-6}\text{Å}^{-2}$ for the scattering length, ρ_p of the internal core of the particles was calculated by means of the usual formulas starting from the scattering lengths of each atom in the deuterated PS repeating unit and assuming a density of 1.088 g/mL for the deuterated PS [143].

In Fig. 30 the resulting fits are shown (grey line: 8% water content and black line: 3% water content) while table 9 reports the corresponding fitting parameters. In spite of substantial number of fitting parameters, they can be mostly well determined. In fact, at least four among them, namely the scattering length densities of the two solvents and the two correction factors for the particle concentration, are fitted simply to account for experimental uncertainties in the sample preparation, which leaves practically only four parameters to fit. This statement is supported by two facts. First, the two fitted solvent scattering length densities reported in table 9 are extremely close to their respective theoretical value (i.e. the values calculate by means of the standard rules) of 5.75×10^{-6} $\mathring{A}^{-2}$ and 6.13×10^{-6} $\mathring{A}^{-2}$ for the 8% and 3% water content, respectively. At this point, one would naturally wonder why we decided to fit for these two parameters. As a matter of fact, the structure of the model implies that very small errors on the scattering length differences result in large variation of the predicted scattered intensities. This forces us to fit for these two additional quantities. Second, as far as the two corrections for the particle concentration are concerned, we note that the resulting fitted values are very close each other thus supporting our previous statement.

Being now able to describe the behavior of the bare particles at small contrast we move on analyzing the SANS data of the PDADMAC coated particles. Fig. 31 shows the scattering from particles coated with PDADMAC at a water content of 8%. Experiments were performed for PDADMAC dose leading to saturation of the electrophoretic mobility. Data were fitted to eq. (20) by modeling the form factor with the scattering amplitude appropriate for a core-shell particle coated with a uniform layer of thickness h_2, namely

$$\begin{aligned} F_2(q,R,h) &= \\ &= \frac{V_p(R_1)F_0(q,R_1)(\rho_p-\rho_1)+V_p(R)F_0(q,R)(\rho_1-\rho_2)+V_p(R_2)F_0(q,R_2)(\rho_2-\rho_s)}{V_p(R_1)(\rho_p-\rho_1)+V_p(R)(\rho_1-\rho_2)+V_p(R_2)(\rho_2-\rho_s)}, \end{aligned} \tag{23}$$

here $R_2 = R + h_2$ is the outer radius, the scattering length density of PDADMAC containing shell is given by $\rho_2 = \phi_{\rm pe}\rho_{\rm pe} + (1-\phi_{\rm pe})\rho_s$ with $\phi_{\rm pe}$ the volume fraction of PDADMAC in the shell and $\rho_{\rm pe}$ its scattering length density, while

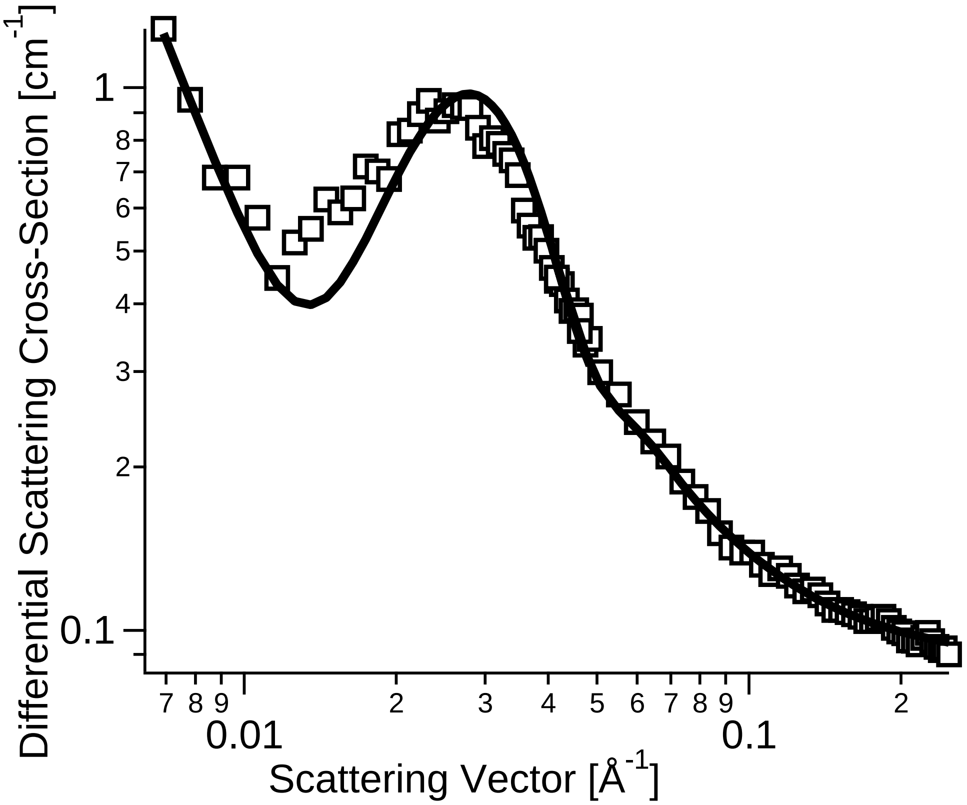

Figure 31: Measured differential scattering cross-section of PDADMAC coated particles at a water content of 8% in weight (markers) with fit (line, see text).

the other quantities have the same meaning as in eq. (22). As opposed to the case of the bare particle, which form stable suspensions, here we had to adopt a structure factor given by [127, 140]

$$S(q) = 1 + Aq^{-d_f}, \tag{24}$$

in order to properly describe the formation of fractal aggregates upon addition of PDADMAC to the sample as mentioned in section 5.2. Keeping all the values of the parameters obtained in the fit for the bare particle dataset, we fitted the scattering curve corresponding to a water content of 8% reported in fig. 31 by letting vary the adsorbed layer shell thickness, the corresponding scattering length density, the correction factor β_{pe} to the particle concentration, the scattering length density of the solvent, and the structure factor parameters. The resulting best fitting parameters are reported in table 10 and the corresponding prediction for the differential scattering cross-section is represented by the solid line in fig. 31. Similar argumentation regarding the number of fitting parameters applies in this case. Here again the value obtained for the solvent scattering length density is very near to the predicted value of 5.75×10^{-6} $\mathring{A}^{-2}$ for the present water content. It is worth noting that the possible contribution to the scattering profile due to PDADMAC in solution was ruled out by independent measurements done on pure PDADMAC samples of the same concentration employed to coat the particles. From the value of the scattering length of the outmost shell and adopting a value of 1.35×10^{-7} $\mathring{A}^{-2}$ for the scattering density of PDADMAC we calculate its volume fraction in the shell to be $\phi_{\mathrm{pe}} = 0.56$. The thickness of the layer is found to be $h_2 = 1.1$ nm. We further find that the layer is very compact, and it contains a polymer volume fraction of 0.6.

In turn we can obtain the most important quantity, namely the adsorbed mass $\Gamma = \delta_{\mathrm{pe}} h_2 \phi_{\mathrm{pe}} = 0.73$ mg/m^2, where for the density of PDADMAC, δ_{pe} we assumed a value of 1.2 g/mL. This value should be compared with 0.6 mg/m^2 obtained from the added amount on PDADMAC and the total particle surface, indicating that all PDADMAC is adsorbed on the particle surface. This fact is expected from the mobility measurements, as the PDADMAC dose was chosen to be equal to the onset of the plateau in mobility curve. It has been shown for very similar systems that the adsorption is complete for all polyelectrolyte doses up to this value [65]. The excellent agreement between

Table 10: Best fitting parameters of the one core two shells model for the PDADMAC coated particles SANS measurement at 8% water content in weight.

h_2 [Å]	$\rho_s(8\%)$ [$\mathring{A}^{-2}$]	ρ_2 [$\mathring{A}^{-2}$]	A	d_f	β_{pe}
10.9	5.60×10^{-6}	2.54×10^{-6}	1.48×10^{-5}	2.39	0.615

the two independently estimated values of the adsorbed mass represents a strong indication of the validity of the present experimental protocol.

We have shown that the box profile of uniform density for the polymer layer yields a very good description of data. One might be tempted to use alternative models accounting for a radial variation of the shell profile. However, given the limited q-range probed, it is unfortunately impossible to extract further information on the profile in the radial direction. For this reason, the estimated layer thickness from the SANS experiment must be interpreted as an average thickness, and we are currently unable to obtain further information on the profile.

The present observations are in good agreement with similar SANS measurements on larger particles coated with a much thicker polyelectrolyte multilayer at low salt. When dividing the observed layer thickness by the number of deposited layers, the average thickness of a single layer turns out to be the range of 1.5 nm - 1.8 nm and a polymer volume fraction of 0.58. While these values are well comparable to the ones reported here, the thickness of a single layer is somewhat smaller than the average value in the multi-layer. Although the systems studied are not fully comparable, the measurements suggest that first adsorbed polyelectrolyte layer is equally dense, but thinner than in a multi-layer.

These findings are equally in good agreement with the light scattering results discussed in the previous chapter. The present SANS experiments were conducted without addition of salt and at PDADMAC concentration of 2.4×IEP. At 10×IEP and no added salt, which were the experimental conditions most close to the ones used for SANS measurements, hydrodynamic thickness inferred from light scattering measurements was zero and increased to about 1 nm at 50×IEP (fig. 24). We suspect that this discrepancy might be a result of substantially different concentrations. While polyelectrolyte concentrations in SANS samples at 1×IEP were in order of 10^1 g/L, light scattering samples were in the order of 10^{-2} g/L. The high dilution of light scattering samples might therefore slowed down the build up of the layer such that no layer could be observed within the experimental time window. Thus, if we assume the suggested shift, we can compare SANS thickness at 2.4×IEP with light scattering results above 50×IEP. The latter thicknesses were 1.1 nm and 1.0 nm, respectively. Note that light scattering is very sensitive to loops and tails protruding into solution. The very close coincidence of the SANS thickness and the hydrodynamic thickness confirms that the layer is very compact, with almost no loops and tails.

5.4 Conclusion

We have been able to investigate an adsorbed monolayer of a cationic polyelectrolyte (PDADMAC) on a negatively charged colloidal particles by SANS. This technique gives a layer thickness of 1.1 nm. We further find that the layer is very compact, and it contains a polymer volume fraction of 0.6. By combining this value with the layer thickness, we find an adsorbed amount 0.73 mg/m^2, which is in excellent agreement with the plateau onset in the electrophoretic mobility. In agreement with the light scattering results discussed in the previous chapter, we confirm that the adsorbed layer of highly charged polyelectrolytes on an oppositely charged colloidal particles is very thin and extremely compact.

6 Aggregation of oppositely charged colloidal particles[2]

6.1 Introduction

In chapter 2, we were dealing with aggregation behavior of particles of the same kind, i.e. homoaggregation. In the following, we aim to extend our studies to a system composed of two different types of particles. Many important processes in nature and in industry are governed by heteroaggregation, that is aggregation between unequal particles. However, compared to homoaggregation [3, 14, 15, 20, 23, 25, 26, 40, 53, 81–87], the heteroaggregation phenomena has been studied to a lesser extent [27, 88–94]. The classical example of heteroaggregation is papermaking [95]. Thereby, the paper is being formed from the slurry through the heteroaggregation of cellulose fibers and filler particles. Other examples involve aggregate formation in flotation processes and water purification [96, 97] or the synthesis of coated particles or nanostructured materials [88, 98]. Heteroaggregation is also much more rich from a conceptual point of view because of the inherent asymmetry originating from the two surfaces of the different particles. Several authors have explored the predictions of the classical theory of Derjaguin, Landau, Verwey, and Overbeek (DLVO) in the symmetric and asymmetric situations [57, 99–104]. The major reason that heteroaggregation was studied to a lesser extent than homoaggregation is the lack of experimental techniques that could be used in routine applications.

One popular approach is to mimic the heteroaggregation processes by the deposition of colloidal particles on a suitably chosen collector [55, 105–108]. This approach evokes the fact that heteroaggregation becomes equivalent to deposition in the limit of a large disparity in the particle size of both constituents. Colloidal deposition can be studied by a variety of techniques,

---

[2] This chapter resulted in the following publication: Lin, W.; Kobayashi, M.; Skarba, M.; Mu, C.; Galletto, P.; Borkovec, M. *Langmuir*, **2006**, *22*, 1038.

such as chromatography in a porous bed [106, 109], optical microscopy [110, 111], or reflectivity [112, 113]. On the basis of such studies, a substantial understanding of colloidal interactions in asymmetric systems has emerged. For example, it has been clearly demonstrated that in oppositely charged systems deposition rate constants increase with decreasing ionic strength and that this trend can be quantitatively captured by DLVO theory [106, 114]. However, the major problem with this analogy is that colloidal deposition is just one special case of heteroaggregation; other techniques must be used to study heteroaggregation processes in the general case.

Heteroaggregation has been studied mainly in mixtures of colloidal particles by time-resolved light scattering techniques. This technique can be routinely used when only heteroaggregation takes place, such as in a mixture of oppositely charged particles at low ionic strength [92, 115, 116]. In the general case, however, homoaggregation and heteroaggregation take place simultaneously, and the separation of both processes is nontrivial. One way to tackle this problem is to measure an apparent aggregation rate constant in such a mixed system. If the particles are exactly the same size (and eventually of the same refractive index), then the apparent aggregation rate constant can be shown to be a weighted sum of the homoaggregation and heteroaggregation rate constants, where the weights are the products of the mole fractions of each constituent [27, 94]. Thus, by measuring this apparent aggregation rate constant as a function of the composition of the binary mixture, homoaggregation and heteroaggregation rate constants can be determined separately. However, this technique is very laborious and requires particles of identical size and composition but with different surface properties. For these reasons, it is of limited applicability in the general case, when both types of particles are of different size and consist of different materials.

In particle deposition, one equally faces the problem of separating homoaggregation from heteroaggregation (i.e., deposition). In this case, the depositing particles may undergo homoaggregation in suspension before they arrive at the collector surface, and eventually one studies the deposition of larger aggregates onto the collector surface. Particular designs for the inlets into the porous bed have been proposed to minimize this problem [117].

Recently, some of us have proposed that angular-resolved static or dynamic light scattering is capable of separating homoaggregation from heteroaggregation for particles of different size [42]. The technique relies on the fact that the form factors of the symmetric and asymmetric doublets made of particles of different size have a different angular dependence, and this feature can be used to separate homoaggregation from heteroaggregation in a single experiment. In this case, there is no need to study the same system at different compositions, even though such data can be useful to test the consistency of the technique. The technique proposed relies on the availability of an optical model for the particle doublets, and so far the simplified approximation due to Rayleigh, Debye, and Gans (RDG) has been used. This approximation is limited to smaller particles, and to be able to handle a wider range of particle size, the general superposition T-matrix technique must be used [118, 119].

As will be shown in this chapter, both techniques can be routinely used to analyze time-resolved light scattering data in binary mixtures of particle suspensions and allow the determination of absolute heteroaggregation rate constants, even in the presence of homoaggregation. The practicability of the technique will be illustrated by studying three different binary systems of oppositely charged particles, whereby the constituent particle systems have been thoroughly characterized with respect to their size, charge, and homoaggregation rates. The measured heteroaggregation rate constants are found to be in good agreement with predictions of DLVO theory.

6.2 Theory

In a colloidal suspension containing particles of opposite charge, homoaggregation as well as heteroaggregation can both occur and will diminish the suspension stability. Determining the heteroaggregation rate constant necessitates that the contributions of both processes are properly distinguished. We will demonstrate that this distinction can be routinely achieved with simultaneous static and dynamic light scattering (SSDLS) performed on a multiangle setup. Once the heteroaggregation rate constants have been determined, they can be compared with predictions of DLVO theory. These computational details are summarized in the following text.

Heteroaggregation rate constants by light scattering.

Consider a colloidal suspension composed of two types of oppositely charged spherical particles A and B. In this case, homoaggregation and heteroaggregation are possible. In the early stages of the aggregation process, particle doublets AA, BB, and AB form according to the following kinetic processes:

$$\begin{aligned} \mathrm{A} + \mathrm{A} &\rightarrow \mathrm{AA} \\ \mathrm{B} + \mathrm{B} &\rightarrow \mathrm{BB} \\ \mathrm{A} + \mathrm{B} &\rightarrow \mathrm{AB} \end{aligned} \tag{25}$$

The concentrations of dimers forming in an aggregating suspension follow the kinetics equations

$$\begin{aligned} \frac{\mathrm{d}N_{AA}(t)}{\mathrm{d}t} &= \frac{k_{AA}N_A^2(t)}{2} \\ \frac{\mathrm{d}N_{BB}(t)}{\mathrm{d}t} &= \frac{k_{BB}N_B^2(t)}{2} \\ \frac{\mathrm{d}N_{AB}(t)}{\mathrm{d}t} &= k_{AB}N_A(t)N_B(t) \end{aligned} \tag{26}$$

where t is the time and $N_A(t)$ and $N_B(t)$ denote the number concentrations of particles of type A and B, respectively. The homoaggregation rate constants for the formation of AA and BB are denoted as k_{AA} and k_{BB}, whereas k_{AB} is the heteroaggregation rate constant.

In a static light scattering experiment in an aggregating binary suspension, the scattered intensity $I(q,t)$ varies with the magnitude of the scattering vector q and time. The scattering vector is given by $q = \frac{4\pi}{\lambda}\sin(\frac{\theta}{2})$, where λ is the wavelength of the light in the medium and θ is the scattering angle. For a dilute aggregating suspension in the early stages, it can be expressed as the sum of scattering intensities due to monomers and doublets, namely

$$I(q,t) = \sum_k I_k(q) N_k(t) \tag{27}$$

where the index k runs over the species present A, B, AA, AB, and BB, the static light scattering intensity of monomers A and B are denoted by $I_A(q)$ and $I_B(q)$, and those of the doublets AA, AB, and BB are denoted by $I_{AA}(q)$, $I_{AB}(q)$, and $I_{BB}(q)$. The apparent rate in the static light scattering experiment intensity is obtained by differentiating eq. 27 and inserting the result into eq. 26. This rate can be written as

$$\frac{1}{I(q,0)} \frac{\mathrm{d}I(q,t)}{\mathrm{d}t}\bigg|_{t\to 0} = k_{AA}F_{AA}(q) + 2k_{AB}F_{AB}(q) + k_{BB}F_{BB}(q) \tag{28}$$

where $I(q,0) = I_A(q)N_A(0) + I_B(q)N_B(0)$ is the initial scattering intensity and the functions $F_{ij}(q)$ are given by [42]

$$F_{ij}(q) = N_0 x_i x_j \frac{I_{ij}(q) - I_i(q) - I_j(q)}{2[x_A I_A(q) + x_B I_B(q)]} \tag{29}$$

where $N_0 = N_A(0) + N_B(0)$ is the initial total particle number concentration and $x_i = N_i(0)/N_0$ is the number fraction of particle i (i = A and B).

In the dynamic light scattering experiment, the measured average diffusion coefficient results from the intensity-weighted contributions of all species present, namely

$$D(q,t) = \frac{\sum_k D_k I_k(q) N_k(t)}{\sum_k I_k(q) N_k(t)} \tag{30}$$

where D_k is the diffusion coefficient of species k with k=A, B, AA, AB, and BB. We usually express the diffusion coefficient in terms of the hydrodynamic radius by the Stokes-Einstein equation

$$D(q,t) = \frac{kT}{6\pi\eta r_h(q,t)} \tag{31}$$

where kT is the thermal energy and η is the viscosity of the medium. Differentiation of eq. 28, combined with eqs. 26 and 27, yields the rate of change of the hydrodynamic radius [42]

$$\left.\frac{1}{r_h(q,0)} \frac{\mathrm{d}r_h(q,t)}{\mathrm{d}t}\right|_{t\to 0} = k_{AA} H_{AA}(q) + 2k_{AB} H_{AB}(q) + k_{BB} H_{BB}(q) \tag{32}$$

with $H_{ij}(q) = F_{ij}(q) G_{ij}(q)$ and the latter function given by

$$G_{ij}(q) = N_0 x_i x_j \frac{I_{ij}(q)/r_{ij} - I_i(q)/r_i - I_j(q)/r_j}{2[x_A I_A(q)/r_A + x_B I_B(q)/r_B]} \tag{33}$$

where r_{ij} are the hydrodynamic radii of the doublets and r_i are the same quantities for the monomers, which coincide with the particle radii for spheres. The latter quantities are obtained by applying the Stokes-Einstein relation to the corresponding diffusion coefficients (cf. eq. 31).

For particles of small size and weak optical contrast, the approximation due to Rayleigh, Debye, and Gans (RDG) is appropriate to model the angular dependence of the scattered intensity for all species in solution. For the monomers, the scattering intensities are given by the classical expression for spheres [119]

$$I_i(q) \propto \frac{1}{q^6}[\sin(qr_i) + qr_i \cos(qr_j)]^2 \tag{34}$$

The intensity of the doublets can be written as [116]

$$I_{ij} = I_i(q) + I_j(q) + 2\sqrt{I_i(q)I_j(q)} \quad \frac{\sin[q(r_i + r_j)]}{q(r_i + r_j)} \tag{35}$$

In the general case of larger particles and strong contrast, the RDG theory fails, and the scattering intensities must be evaluated with the Mie theory for the monomers, and with the superposition T-matrix theory for the doublets [118, 119]. Although both approaches are mathematically relatively complex, comprehensive computer codes are available for both, and thus these theories can be used routinely for the determination of aggregation rates.

The relative hydrodynamic radius α of a doublet can be approximated by the following expression [116]

$$\alpha = \frac{2r_{AB}}{r_A + r_B} = 1.392 + 0.608\left(\frac{r_B - r_A}{r_B + r_A}\right)^2 \tag{36}$$

when the particle radii are known. This expression is valid at low Reynolds numbers.

Aggregation rate constants from DLVO theory

Theoretical aggregation rate constants are calculated from the modified Fuchs' expression [17]

$$k_{ij} = \frac{2(r_i + r_j)}{3\beta\eta r_i r_j}\left\{ \int_0^\infty \frac{B_{ij}(h)}{(r_i r_j + h)^2}\exp[\beta V_{ij}(h)]\mathrm{d}h \right\}^{-1} \tag{37}$$

where $\beta = 1/(kT)$ is the inverse thermal energy, h is the distance between particle surfaces, $V_{ij}(h)$ is the interaction potential, and $B_{ij}(h)$ is the hydrodynamic factor. The pair interaction energy is approximated as

$$V_{ij}(h) = V_{ij}^{(vdW)}(h) + V_{ij}^{(dl)}(h) \tag{38}$$

where $V_{ij}^{(vdW)}(h)$ is the van der Waals interaction potential and $V_{ij}^{(dl)}(h)$ is the potential due to overlap between the diffuse layers.

Within the Derjaguin approximation, the van der Waals interaction potential reads

$$V_{ij}^{(vdW)}(h) = -\frac{A_{ij} r_i r_j}{6(r_i + r_j)h} \tag{39}$$

where A_{ij} is the Hamaker constant between the media making up particles i and j. In an asymmetric system, the Hamaker constant can be estimated by means of the mixing rule [19]

$$A_{ij} = \sqrt{A_{ii}A_{jj}} \tag{40}$$

where A_{ii} is the Hamaker constant in the symmetric system. The double-layer overlap potential $V_{ij}^{(dl)}(h)$ was determined numerically by solving the Poisson-Boltzmann equation between two charged plates [57]. Depending on the situation, boundary conditions are chosen as constant charge or charge regulation. The hydrodynamic factor, which represents the relative longitudinal mutual diffusion coefficient, is approximated by the expression [54]

$$B_{ij}(h) = \frac{6(h/a_{ij})^2 + 13(h/a_{ij}) + 2}{6(h/a_{ij})^2 + 4(h/a_{ij})} \tag{41}$$

where the effective radius is given by $a_{ij} = 2r_i r_j/(r_i + r_j)$. Although this formula was developed for the symmetric case, it can be verified to coincide with the leading asymptotic terms for short and long distances in the asymmetric situation [120].

We will normally report the dimensionless stability ratio defined as

$$W_{ij} = \frac{k_{ij}^{(fast)}}{k_{ij}} \tag{42}$$

where k_{ij} is the actual rate constant and $k_{ij}^{(fast)}$ is the rate constant under fast aggregation conditions. Experimentally, the latter can be obtained by working at sufficiently high salt concentration where the electrostatic interactions are screened. Within DLVO theory, $k_{ij}^{(fast)}$ is obtained by considering only the van der Waals contribution in eq. 38.

Electrophoretic mobility

The particle charge can be assessed by electrophoretic mobility measurements. The electrophoretic mobility is evaluated from the ζ-potential with the standard electrokinetic model as implemented by O'Brien and White [52].

The potential at the shear plane is calculated from the potential profile of the diffuse layer

$$\zeta = \frac{4}{\beta e} \operatorname{arctanh}\left[\tanh\left(\frac{\beta e \psi_d}{4} \right) \exp(-\kappa d) \right]. \tag{43}$$

where ψ_d is the diffuse layer potential, d is the distance between the surface and the shear plane, and κ^{-1} is the Debye length. Such a distance d should be associated with the thickness of the water layer on the particle surface.

6.3 Experimental

Particle characterization and sample preparation

Sulfate- and amidine-terminated surfactant-free polystyrene latex particles were purchased from Interfacial Dynamics Corporation (IDC, Portland, USA). The particle size distribution was characterized by the number-weighted mean particle radius and the corresponding coefficient of variation (CV) as determined by transmission electron microscopy (TEM) by the manufacturer. He further reports the particle number concentration and the particle charge density as determined by conductometric titrations. The particle size was verified in a stable dilute suspension by static and dynamic light scattering, and both values were in excellent agreement with the values reported by the manufacturer. Before use, the latex particles were extensively dialyzed for about 2 weeks in deionized water (Milli-Q, Millipore) until no change in the conductivity of the surrounding water was detected. Particle concentrations given by the manufacturer were found to be in good agreement with the total carbon analysis, and their values after dialysis were obtained by comparison of the static light scattering intensity with that of the original samples. Silica particles (KEP30H) were kindly supplied by the manufacturer (Nippon Shokubai, Japan). The particles were held at 800°C in a covered quartz crucible for 24 h. The particle radii and CV were again determined by light scattering and TEM. The charge densities were obtained by potentiometric titrations. We have presented details on this batch of silica particles in chapter 2. All experiments were carried out at 25°C. Table 11 summarizes the important particle properties.

Electrophoretic mobility

A laser doppler velocimetry setup Zeta Sizer 2000 by Malvern (Malvern, UK) was used to measure the electrophoretic mobility of the particles. Measurements were carried out under similar conditions as for light scattering. The concentration of latex particles for the three samples studied was equal to about 4 mg/L, and the ionic strength of the suspension was tuned by the addition of 2 M KCl. The amidine latex A220 and silica were measured as a function of pH for different ionic strengths, which was adjusted by KCl. The suspension pH was measured with a combination electrode 6.0234.110 from Metrohm (Herisau, Switzerland). The concentration of silica particles in the suspensions was around 40 mg/L.

Particle aggregation by light scattering

The aggregation in colloidal particle suspensions was studied by time-resolved SSDLS. We used the same goniometer setup as described in chapter 2.

The autocorrelation functions are accumulated for 20 s and analyzed with a second-order cumulant fit. By rotating the goniometer (see fig. 5 in chapter 2), additional scattering angles can be measured, thereby increasing the angular resolution.

Glass cuvettes for light scattering were cleaned in boiling 3:1 mixtures

Table 11: Particle Characterization

batch	radius[a] [nm]	polydispersity[b] (CV)	site density[c] [nm^{-2}]	experimental fast rate[d] [$\times 10^{-18}$ m^3/s]	theoretical fast rate [e] [$\times 10^{-18}$ m^3/s]	Hamaker constant A[f] [$\times 10^{-20}$ J]
A160	80.0	0.14	0.51	2.7 ± 0.5	9.6	1.3
A220	110	0.08	0.64	3.3 ± 0.6	9.6	1.3
A482	241	0.03	1.0	2.4 ± 0.7	9.6	1.3
S277	139	0.05	0.20	2.7 ± 0.5	9.6	1.3
S358	179	0.03	0.075	2.1 ± 0.7	9.6	1.3
KEP30H	150	0.04	8.0	3.2 ± 0.6	8.4	0.8

[a] Radius obtained by light scattering.

[b] Polydispersity reported as the coefficient of variation (CV) obtained from transmission electron microscopy (TEM).

[c] Surface density of charged groups obtained by conductometric titrations.

[d] Absolute fast aggregation rate constant measured by simultaneous static and dynamic light scattering (SSDLS) at high salt conditions.

[e] Fast aggregation rate constant as calculated with eq. 37.

[f] Hamaker constant used to calculate the rate constants.

of concentrated H_2SO_4 and H_2O_2 (30%) and thoroughly rinsed with Milli-Q water. The background electrolyte was prepared in the cuvette at the prescribed concentration by diluting the 2 M KCl solution with Milli-Q water. For homoaggregation experiments, a dilute latex suspension was added to the electrolyte solution. For heteroaggregation experiments, dilute latex suspensions were mixed with the electrolyte solution; subsequently, these solutions were mixed together. In the case of latex particles, the total particle number concentration was $N_0 = 2 \times 10^{14}$ m^{-3}. For experiments involving latex particles, the electrolyte was adjusted to pH 4 with dilute HCl. In this case, the aggregation was monitored with an angular resolution of 8° for about 1 h. For experiments involving silica and amidine latex particles, the total particle number concentration was $N_0 = 6 \times 10^{13}$ m^{-3}. The pH of the solutions was varied by the addition of HCl and measured at the end of each experiment with a combination electrode. In this case, measurements were done every 5° because the total number concentration was sufficiently low and the aggregation proceeded rather slowly.

The formation of aggregates was monitored by changes in the scattering intensity and the increase in the mean hydrodynamic radius of the suspension at sufficiently short times. The initial rate of change of the scattering intensity and the hydrodynamic radius measured at different scattering angles were estimated from the slope of the straight line fitted to the experimental data. The early stages of aggregation can be probed by ensuring that the relative increase in the hydrodynamic radius does not exceed 20%. In addition, the half-time of the aggregation $T_{1/2} \approx 1/(k_{AA}N_0)$, which can be estimated by assuming the rate constant is equal to the Smoluchowski value of 1.2×10^{-17} m^3/s, is always larger than the time window of the experiment.

6.4 Results and discussion

Suspensions of positively charged amidine latex particles, negatively charged sulfate latex, or silica particles were characterized with respect to their surface charge and the rate of homoaggregation. Heteroaggregation rate constants were determined in binary mixtures of these positively and negatively charged particles over a wide range of solution composition. The obtained results are compared with calculations based on DLVO theory.

Model particle suspensions and homoaggregation

We will first report on the results of amidine latex particles and then discuss analogous results for sulfate latex particles and finally summarize the properties of the silica particles used.

Three batches of amidine latex particles were investigated, namely, A160, A220, and A482. Their particle radii measured by light scattering and their surface charge densities obtained by conductometric titrations are summarized in table 11. Figure 32 shows their electrophoretic mobilities as a function of the ionic strength in KCl solutions at pH 4. Because of the positive charge of the particles, the values of the mobility are positive, and they go through a characteristic maximum. As indicated by the solid line in fig. 32, this maximum can be rationalized in terms of the standard electrokinetic model for particles of a fixed surface charge density as implemented by O'Brien and White [52]. To obtain quantitative agreement, however, we have introduced a finite distance of the plane of shear located at $d = 0.5$ nm. In this fashion, the data can be quantified with the conductometric charge densities given in table 11. When no plane of shear is introduced, the surface charge must be substantially reduced to obtain acceptable agreement with the experimental data [121]. We have further verified that the electrophoretic mobilities of these particles are basically independent of pH in the relevant range (fig. 33).

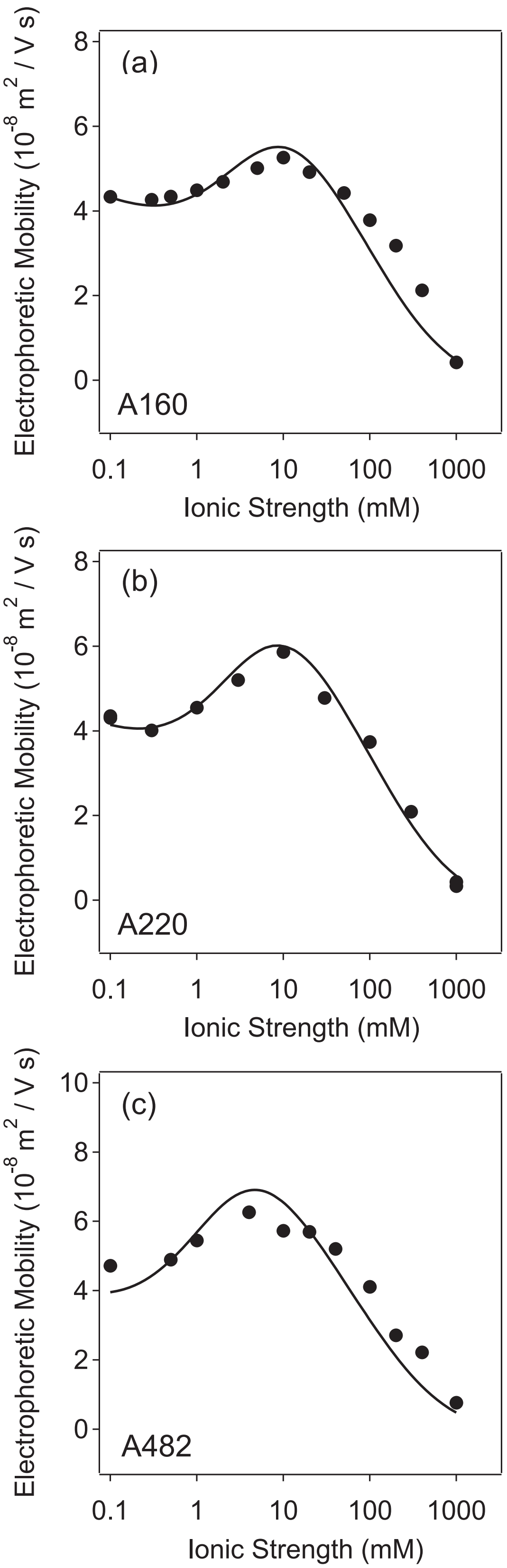

Figure 32: Electrophoretic mobility of amidine latex particles as a function of the ionic strength in KCl at pH 4. Symbols denote experimental points, and solid lines are theoretical calculations with the standard electrokinetic model with the conductometric surface charge reported in table 11 and with a plane of shear at a distance d = 0.5 nm. (a) A160, (b) A220, and (c) A482.

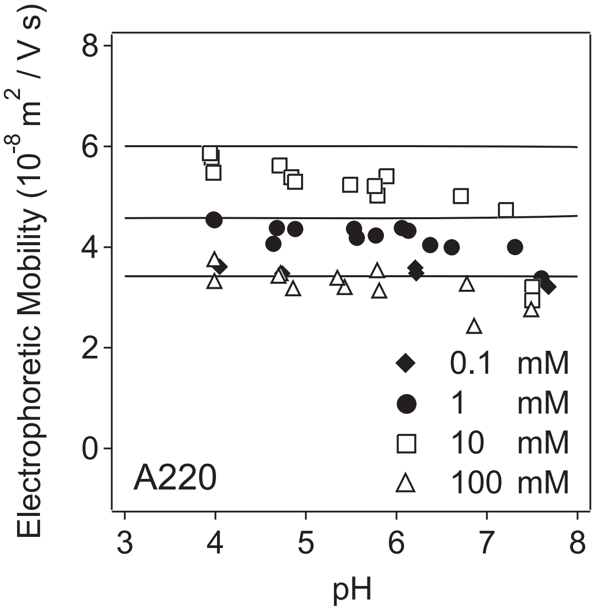

Figure 33: Electrophoretic mobility of amidine latex particles A220 as a function of pH at different ionic strengths in KCl. Symbols denote experimental points, and solid lines indicate the constant values expected. The slight decrease in the experimental data indicates weak deprotonation of the amidine surface groups.

The stability ratios of the amidine latex particles are reported as a function of the ionic strength in fig. 34. One observes the typical behavior where the stability ratio is unity for high ionic strengths (fast aggregation conditions), and below the critical coagulation concentration (CCC) it strongly increases with decreasing ionic strengths (slow aggregation conditions). The DLVO theory suggests qualitatively similar behavior. Quantitatively, however, it fails in two respects because it predicts the CCC to lie at substantially higher ionic strengths and a dependence of the stability ratio on the ionic strength that is much stronger than experimentally observed. In the calculations, we have used constant charge boundary conditions and a Hamaker constant of 1.3×10^{20} J as proposed earlier [53]. The choice of different boundary conditions (e.g., constant potential) affects the results only marginally. However, by decreasing the Hamaker constant one could in principle rationalize the position of the CCC, but the Hamaker constant would have to be at least 1 order of magnitude smaller. This value is certainly unrealistic. We suspect that the reason for the discrepancy in the position of the CCC is the reduction of the surface charge by the adsorbed anions. However, the slope of the stability curve cannot be influenced by any of the mentioned parameters, and this deviation is probably related to surface charge heterogeneities or discrete charge effects [53].

For all three amidine particles, the fast aggregation rate constants are in the range of $(2.8 \pm 0.4) \times 10^{18}$ m^3/s, which is somewhat lower than the value of 9.6×10^{18} m^3/s predicted by DLVO theory (table 11). Similar discrepancies have been reported earlier for similar particles, and they are probably related to the inaccuracies in the DLVO interaction potential at larger distances [53].

In a similar fashion, we have analyzed two batches of sulfate latex particles, namely, S277 and S358. The particle radii and surface charge densities are given in tab. 11. The electrophoretic mobilities are shown in fig. 35 as a function of the ionic strength in KCl solutions of pH 4. In this case, the particle charge is negative, and thus the electrophoretic mobility bears a negative

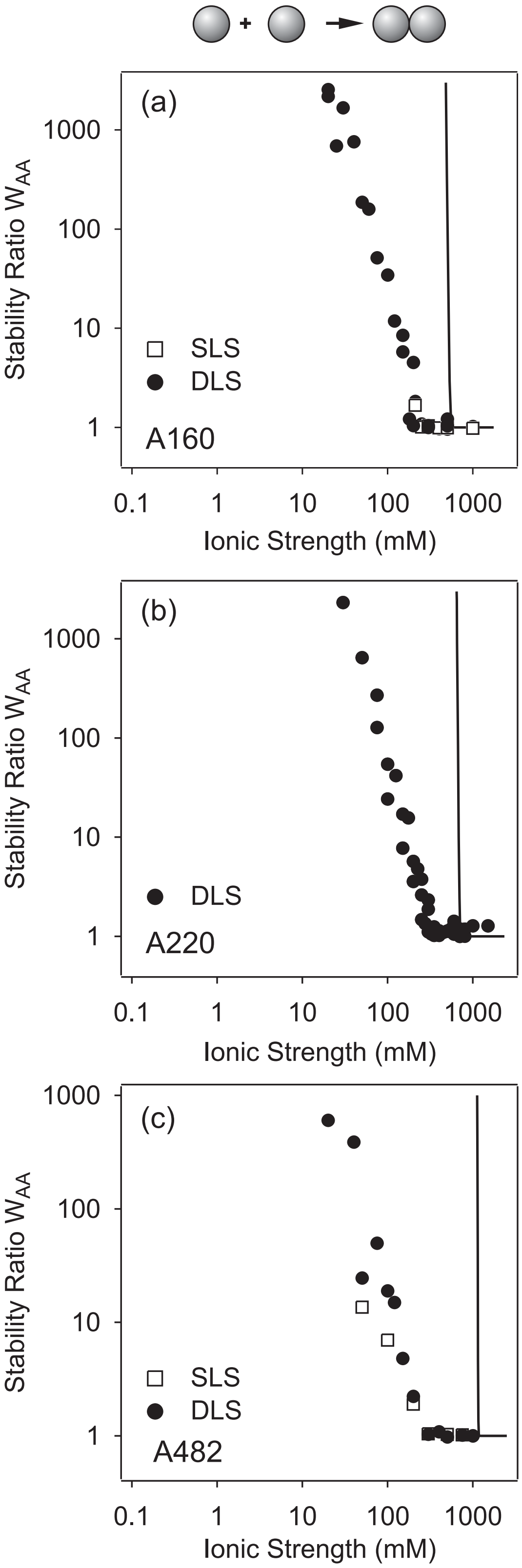

Figure 34: Stability ratios of amidine latex particles as a function of the ionic strength in KCl at pH 4. The experimental data are compared with DLVO theory with the conductometric surface charge reported in Table 1, constant charge boundary conditions, and a Hamaker constant of 1.3×10^{20} J. (a) A160, (b) A220, and (c) A482. The DLVO theory predicts a stronger ionic strength dependence than expected experimentally.

sign. A dependence analogous to that for the amidine particles is observed, but in this case, the mobilities go through a minimum as a function of the ionic strength. The solid line in fig. 35 demonstrates that this minimum can also be explained in terms of the standard electrokinetic model [122]. However, quantitative agreement is obtained with the conductometric charge densities without a plane of shear ($d = 0$). Recall that the plane of shear had to be introduced at a distance of $d = 0.5$ nm for the amidine latex particles. This difference could reflect that the particle surface of the sulfate latex is smoother than for the amidine latex.

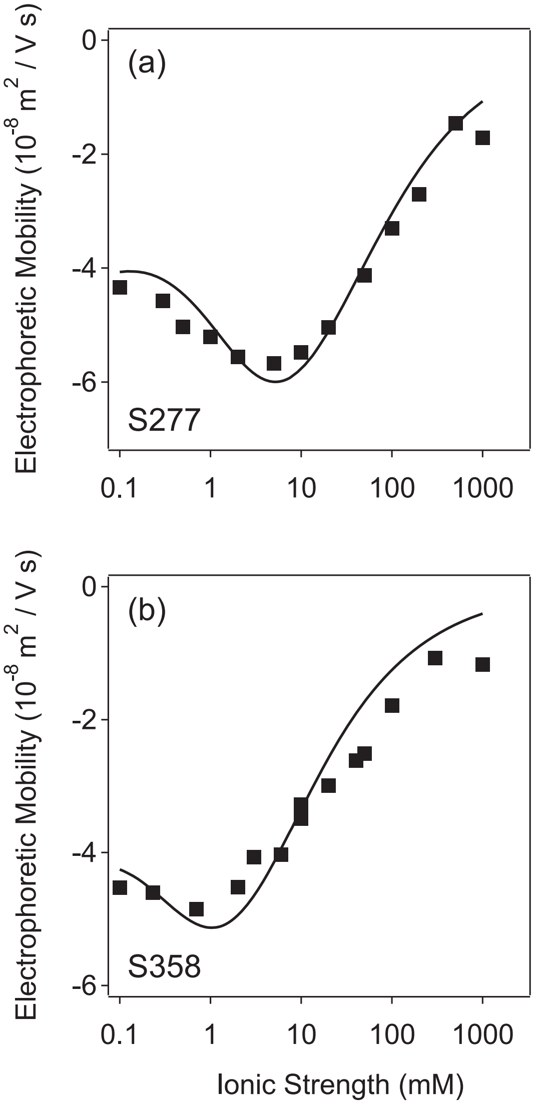

Figure 35: Electrophoretic mobility of sulfate latex particles as a function of the ionic strength in KCl at pH 4. Symbols denote experimental points, and solid lines are theoretical calculations with the standard electrokinetic model with the conductometric surface charge reported in table 11 and no plane of shear ($d = 0$). (a) S277 and (b) S358.

The stability ratios for the sulfate latex particles are shown as a function of the ionic strength in fig. 36. Behavior very similar to that for the amidine latex is observed. At high ionic strengths, the stability ratio is unity, and it strongly increases with decreasing ionic strengths below the CCC. The DLVO theory predicts the position of the CCC more accurately than in the case of the amidine particles, but the same discrepancies concerning the slope of the stability curve remain. Again, we use constant charge boundary conditions and a Hamaker constant of 1.3×10^{20} J. The agreement of the CCC for the sulfate latex is certainly better than for the amidine particles.

The fast aggregation rate constants are in the range of $(2.4 \pm 0.4) \times 10^{18}$ m^3/s. These values are similar to the ones reported for the amidine latex particles and lie below the value obtained by DLVO theory (tab. 11). Again, we suspect that inaccuracies in the DLVO interaction potential at larger distances are responsible for this behavior.

The analogous results for silica particles KEP30H are shown in figs. 10b and 11b and table 11. The characterization, charging behavior, and stability of these particles have been extensively discussed in chapter 2; therefore, only a brief summary is given here for completeness. The electrophoretic mobility is shown in fig. 10b, and it strongly decreases with increasing pH. The reason is the buildup of negative surface charge due to the dissociation of silanol groups according to eq. 7. The dissociation equilibrium can be modeled in the context of the basic Stern model [39, 50]. The parameters used are the dissociation constant of the silanol surface group of $\mathrm{p}K = 7.5$, the Stern capacitance of 2.9 $\mathrm{F/m}^2$, and a surface site density of 8 nm^{-2} as proposed by Hiemstra et al. [50]. Again, the standard electrokinetic model is capable to describe the electrokinetic data quantitatively. However, a finite distance of the shear plane of $d = 0.25$ nm must be introduced in order to rationalize the data.

The stability data for these silica particles are shown in fig. 11b. One observes that the particles aggregate rapidly at low pH, while the aggregation

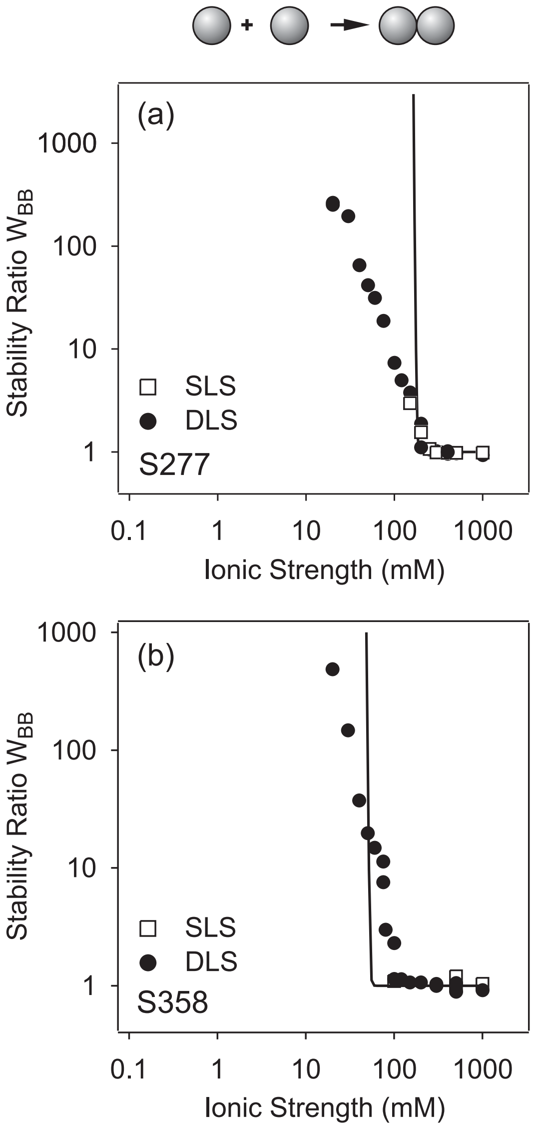

Figure 36: Stability ratio of sulfate latex particles as a function of the ionic strength in KCl at pH 4. The experimental data are compared with DLVO theory with the conductometric surface charge reported in table 11, constant charge boundary conditions, and a Hamaker constant of 1.3×10^{-20} J. (a) S277 and (b) S358. The DLVO theory predicts a stronger ionic strength dependence than expected experimentally.

slows down when the pH is increased. The trends can be explained with DLVO theory reasonably well. The accepted value of the Hamaker constant $A = 8.3 \times 10^{-21}$ J for silica across water was used for the calculations [19,44]. We have further used full charge regulation to evaluate the stability ratios, but the boundary conditions have a relatively minor effect on the predicted stability ratios. Although the ionic strength dependencies are not described very well, such relatively good agreement with DLVO theory is rather unusual for silica [20,23,25]. A detailed discussion of this point was made in chapter 2 and in [26]. The fast aggregation rate constants are $(3.7 \pm 0.6) \times 10^{-18}$ m^3/s, which is somewhat larger than the values reported for the latex particles (tab. 11). Again, this value is lower than the one obtained by DLVO theory, probably for the same reason as discussed above.

Heteroaggregation of oppositely charged particles

After the discussion of these model particle suspensions, we will focus on the measurement of the heteroaggregation rate constants, possibly in the presence of homoaggregation. Later, we will compare the experimental results with DLVO theory. Three binary systems of oppositely charged particles were investigated, namely, A160-S277, A482-S358, and A220-KEP30H (tab. 12).

Determination of heteroaggregation rate constants

We have measured the initial apparent static and dynamic aggregation rate constants as a function of the scattering angle for dilute binary mixtures of oppositely charged particles. Exemplary results are summarized in fig. 37. The left column refers to static light scattering (SLS), and the right column, to dynamic light scattering (DLS). The heteroaggregation rate constants k_{AB} are determined by fitting the expressions given in eqs. 28 and 32 to the experimental data. No other parameters are fitted because they are known from independent experiments. The particle number density and the mole fraction of the amidine latex particles x_A are known from sample preparation. The homoaggregation rate constants k_{AA} and k_{BB} have been discussed previously, and the determined values have been used in the analysis. The relative hydrodynamic radius of the dimer has been estimated from the approximation formula given in eq. 36. Finally, the optical properties of the dimer can be calculated on the basis of one of the two approaches discussed, either RDG theory or T-matrix analysis. Although the T-matrix analysis is the rigorous way to treat the problem, the RDG theory is much simpler and also correct for sufficiently small particles. However, the T-matrix requires the refractive indices of the particles, which have been taken to be 1.596 for

Table 12: Heteroaggregation Rate Constants

binary system[a]	ionic strength [M]	experimental rate (SLS)[b] [$\times 10^{-18}$ m^3/s]	experimental rate (DLS)[c] [$\times 10^{-18}$ m^3/s]	theoretical fast rate [d] [$\times 10^{-18}$ m^3/s]	Hamaker constant A[e] [$\times 10^{-20}$ J]
A160-S277	0.0001	6.4±0.4	6.4±0.4		
x_A=0.80	0.002	5.0±0.4	4.5±0.4		
	1.5	3.6±0.3	3.9±0.4		
	> 0.1[f]	3.6±0.4	3.7±0.5	10.3	1.3
A482-S358	0.0001	5.0±0.4	5.0±0.4		
x_A=0.20	0.001	4.5±0.4	4.6±0.4		
	1.0	3.9±0.5	4.0±0.5		
	> 0.1[f]	4.0±0.7	3.9±0.7	9.8	1.3
A220-KEP30H[g]	0.0001	7.8±0.7	8.7±0.7		
x_A=0.67	0.001	4.5±0.6	5.2±0.6		
	1.0	3.7±0.4	3.1±0.3		
	> 0.1[f]	4.1±0.4	3.3±0.3	9.0	1.0

[a] Binary colloidal systems investigated at the number faction of amidine particles x_A.

[b] Heteroaggregation rate constant measured by static light scattering (SLS).

[c] Heteroaggregation rate constant measured by dynamic light scattering (DLS).

[d] Fast heteroaggregation rate constant calculated with eq. 37.

[e] Hamaker constant used to calculate the rate constants.

[f] Fast aggregation conditions.

[g] Measurement made at pH 7; all others are at pH 4.

latex and 1.460 for silica [44,85]. The best fits of the experimental data with both theories are shown in fig. 37, whereby thin lines correspond to RDG and thick lines correspond to the T-matrix analysis. The resulting heteroaggregation rate constants are summarized in table 12. The good agreement between the rate constants obtained by static and dynamic light scattering, being two rather different methods, confirms the validity of the presented approach. In general, however, we consider multiangle dynamic light scattering to be the method of choice, particularly because the data can be extrapolated to short times more easily [42].

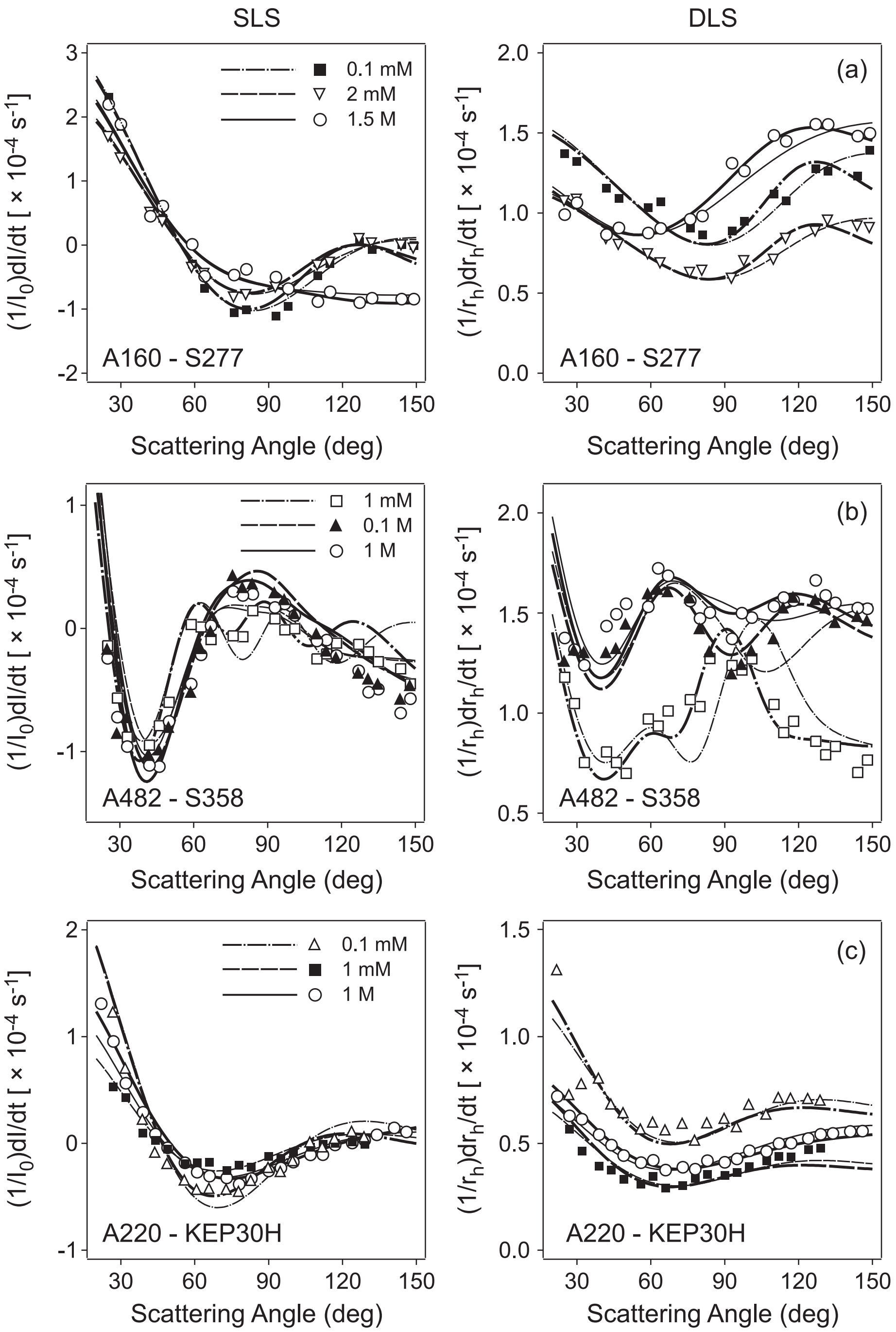

Figure 37: Apparent aggregation rates as measured by static light scattering (SLS) and dynamic light scattering (DLS). The experimental points are plotted as a function of the scattering angle. Thin lines are best fits to the RDG model, and thick lines are best fits to the T-matrix method. Amidine and sulfate latex particles at fixed number fraction of amidine x_A for various ionic strengths. (a) A160-S277 at $x_A = 0.80$ and (b) A482-S358 at $x_A = 0.20$. (c) Amidine latex and silica particles A220-KEP30H at $x_A = 0.67$ for various ionic strengths.

Let us first discuss the case of amidine and sulfate latex particle mixture A160-S277 shown in fig. 37a, where measurements at three ionic strengths are compared. The amidine number fraction is $x_A = 0.80$. In this case, both particles are relatively small. Therefore, the RDG theory represents a good approximation, and the T-matrix results are not very different. At the two lowest ionic strengths of 0.1 and 2 mM, only heteroaggregation occurs. This point is obvious from the fact that the angular dependence of the apparent rate constants is the same and only its magnitude is different. This difference in magnitude is related to the fact that the heteroaggregation rate constant at 0.1 mM is substantially larger than the value at 2 mM (table 12). This decrease is related to the screening of the attractive interactions between the particles and will be discussed in more detail below. At an ionic strength of 1.5 M, heteroaggregation and homoaggregation occur simultaneously. This point is obvious from fig. 37a because the angular dependence of the apparent rate constants is different than at low ionic strengths. One should point out that even in the presence of homoaggregation the present method is very sensitive to heteroaggregation. Without heteroaggregation, it would be impossible to describe the observed angular dependence. The resulting values of heteroaggregation rate constants in the fast aggregation regime are comparable to the corresponding rate constants for homoaggregation. We found the heteroaggregation rate constant to be independent of ionic strength for values above 0.1 M, and the corresponding averaged values are reported in table 12. We have carried out similar calculations by taking into account sample polydispersity, and we found that their effects were minor indeed.

From a chemical point of view, the second example of amidine and sulfate latex particle mixture A482-S358 investigated at the number fraction of $x_A = 0.20$ is very similar to the previous one. However, the particles are much larger, and thus we expect the RDG theory to fail. This point is clearly illustrated in fig. 37b, where one can see that it is impossible to obtain a good fit with the RDG theory, whereas with the T-matrix method an almost perfect fit is obtained. Note that the particularly distinct features in the 0.1 mM data are described perfectly well with the T-matrix analysis. The resulting heteroaggregation rate constants are again summarized in table 12, and their values are comparable to the ones found for the previous case of the A160-S277 mixture. The fast heteroaggregation rate constants are again very similar.

As the last example, we have studied the mixture of amidine and silica particles A220-KEP30H at pH 7.0. Representative results are summarized in 37c and table 12 at an amidine number fraction of $x_A = 0.67$. Because the particles are relatively small and the optical contrast of silica is weaker than for latex, RDG is expected to hold. This fact is confirmed by the fact that RDG theory and T-matrix analysis give virtually identical results. This case again illustrates the situation where heteroaggregation happens exclusively at low ionic strength whereas at higher ionic strength homoaggregation and heteroaggregation occur at the same time. The resulting fast heteroaggregation rate constants are again very similar to the previously reported ones.

Heteroaggregation rate constants and DLVO theory

We now come to the major results of this chapter, namely, the measurements of absolute heteroaggregation rate constants for oppositely charged particles as a function of the salt level and the particle charge. The variation of the latter is achieved for the silica particles by changing the pH. We will first report the absolute heteroaggregation rate constants in the fast aggregation regime and then discuss the corresponding stability ratios as a function of salt level and pH.

Table 12 summarizes the rate constants in the fast regime. There is no systematic difference between the three systems investigated, and we find $(3.7 \pm 0.4) \times 10^{18}$ m^3/s. This rate constant is somewhat larger than the values observed for homoaggregation. Depending on the system, the DLVO theory predicts values in the range of $(9.0 \pm 0.5) \times 10^{18}$ m^3/s. The Hamaker constant for the mixed silica–latex system is estimated by the mixing rule (table 12 and eq. 40). As in the case for homoaggregation, the predicted rate constants are larger than the ones observed experimentally. We suspect that the reasons for the discrepancy are the same as for homoaggregation, and they could be related to inaccuracies in the DLVO potential at larger distances.

The ionic strength dependence of the stability ratios for pure heteroaggregation in the sulfate-amidine mixtures is shown in fig. 38a and b. In both systems, one observes a decrease in the stability ratio with decreasing ionic strength. This decrease is gradual and sets only at ionic strengths <10 mM. At the lowest ionic strengths investigated, the maximum acceleration was about a factor of 2. This dependence can be predicted by DLVO theory without any adjustable parameters with the constant charge boundary condition. In an earlier study, some of us have reported a much stronger dependence of the heteroaggregation rate constant on the ionic strength in a similar amidine-sulfate system [42]. We have also been able to observe similar behavior for a different pair of amidine-sulfate particles but not for the ones reported here. Possibly, differences in the particle synthesis or the presence of impurities is responsible for this anomaly.

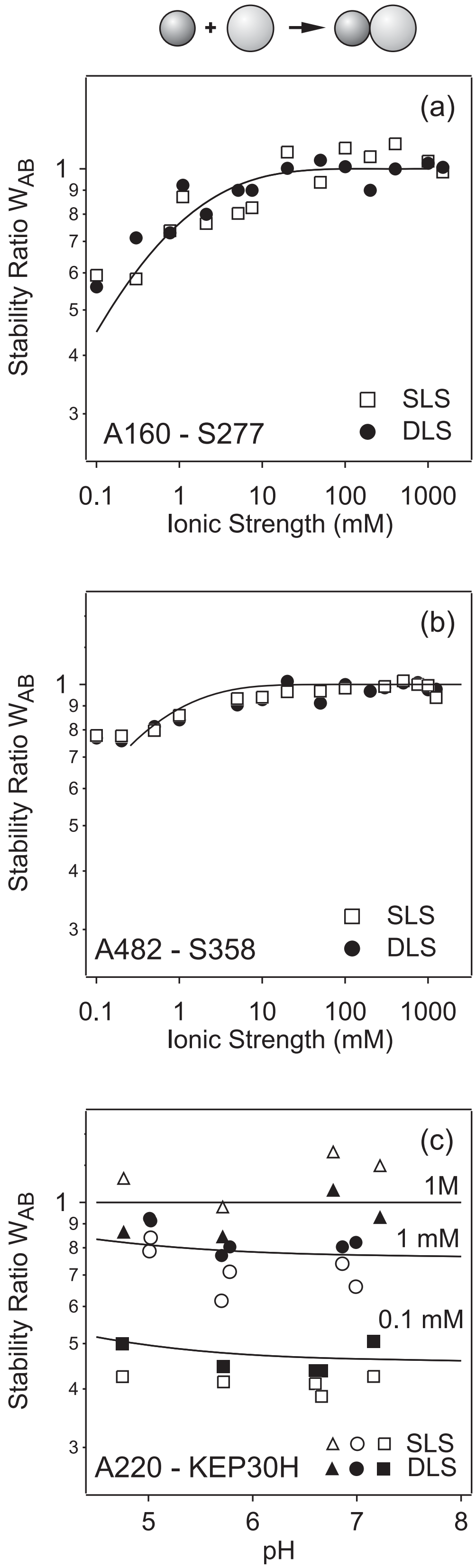

Figure 38: Heteroaggregation in mixed binary suspensions of oppositely charged particles. Symbols are experimental points, and lines are DLVO calculations. Stability ratio for amidine and sulfate latex as a function of ionic strength, namely, (a) A160-S277 and (b) A482-S358. In the latter case, DLVO theory yields spurious instabilities at lower ionic strengths. (c) Stability ratio for amidine latex and silica particles A220-KEP30H as a function of pH for various ionic strengths.

The silica-amidine system is more interesting because the surface charge of silica can be varied over a wide range. The results of the stability ratios as a function of pH are shown for different salt levels in Figure 38c. At first sight, one might be surprised to find that the heteroaggregation rate remains independent of pH, although the charge on silica has been varied by almost 2 orders of magnitude. At the same time, the surface charge of amidine remains essentially constant, as verified by electrophoresis (fig. 33). The DLVO theory predicts the observed trend in the heteroaggregation rate perfectly well. Evidently, heteroaggregation rate constants of oppositely charged particles are independent of the surface charge density over a wide range of values. This insensitivity is related to the fact that the interaction potential is always attractive and the rate constant is mainly limited by diffusion and is hardly affected by additional attractive forces. However, the overall suspension stability will be a strong function of the particle charge [91]. This effect results from the fact that homoaggregation and heteroaggregation will occur simultaneously and the homoaggregation rate constant depends strongly on the particle charge.

6.5 Conclusion

We have measured heteroaggregation rate constants in mixtures of well-characterized colloidal particles of opposite charge with multiangle static and dynamic light scattering. With this technique, it is possible not only to measure absolute heteroaggregation rate constants routinely but also to perform such measurements in the presence of homoaggregation. In particular, we are able to accurately estimate absolute heteroaggregation rate constants in the fast aggregation regime for the first time. Heteroaggregation rate constants have also been measured over a wide range of parameters, for example, ionic strength and different surface charge densities. We find that the rate constant slowly increases with decreasing ionic strength, and provided the surface charge is sufficiently large, it is largely independent of its magnitude.

The DLVO theory captures these trends quantitatively.

7 Conclusions and outlook

We have presented a study on interactions of colloidal particles with simple electrolytes and polyelectrolytes.

After heat treatment, colloidal stability of Stöber-type silica particles follows the predictions of DLVO theory quantitatively. This observation is in sharp contrast to many reports of anomalous colloidal stability of silica. While heating had substantial effect on the surface charge measured by potentiometric titrations, almost no change was observed for electrophoretic mobilities. In future, heating effect on other types of silica or other metal-oxide particles could be investigated in more detail.

Investigations of charging and electrokinetic properties of colloidal particles were conducted also in presence of divalent counterions. Due to strong ion-ion correlations in such systems, qualitatively different behavior of electrophoretic mobility was observed. As the classical theories neglect the ion-ion correlations, they failed to predict the overcharging effect. Monte Carlo simulations, based on purely physical interactions, were able to explain the sign reversal of the electrokinetic potential. Further research in this direction might be focused on effects of other simple electrolytes, especially those with trivalent cations.

Charge on colloidal particles was also reversed by adsorption of oppositely charged polyelectrolytes. Thickness of an adsorbed polyelectrolyte monolayer was measured by both light and neutron scattering techniques. With presented light scattering technique, typical measured hydrodynamic thickness varied between (1 to 8) nm. Similar trends in layer thickness were found for different systems of particles and polyelectrolytes. Measurements with small angle neutron scattering confirmed that the layer of PDADMAC is very thin and compact.

Heteroaggregation rate constants were measured in mixtures of oppositely charged particles. With the adopted technique we were able to perform such measurements in the presence of homoaggregation. In particular, we are able to accurately estimate absolute heteroaggregation rate constants in the fast aggregation regime for the first time. Observed trends were in accordance with DLVO theory.

Remerciements

Je souhaite remercier toutes les personnes qui ont rendu possible la réalisation de cette thèse, en particulier:

Prof. Michal Borkovec pour ses conseils, ses encouragements et pour les discussions scientifiques que nous avons partagées durant ces quatre ans,

Prof. Massimo Morbidelli (ETH Zürich) et Prof. Oliver Wenger (Université de Genève) pour avoir accepté de faire partie du comité scientifique de cette thèse et pour tous leurs commentaires précieux,

tous mes collègues du Laboratory of Colloid and Surface Chemistry, en particulier Dr. Andrea Vaccaro, Dr. Duško Čakara, Dr. Paolo Galletto, Dr. Georg Papastavrou, Dr. Wei Lin and Dr. Motoyoshi Kobayashi pour toutes les heures de discussions productives passées en leur compagnie,

Dr. Christophe Labbez (Université de Bourgogne) et Prof. Bo Jönsson (Université de Lund) pour m'avoir fourni la simulation de Monte Carlo,

Stéphane Jeanneret et François Bujard pour leur assistance au niveau de l'électronique et de la mécanique,

Esther Schwarz et Sandra Salinas pour leur aide généreuse concernant l'administration,

le Fonds national suisse de la recherche scientifique et l'Université de Genève pour leur soutien matériel,

et ma famille pour tout leur soutien.

References

[1] Ostwald, W. *An introduction to theoretical and applied colloid chemistry.* Chapman and Hall: London, 1919.

[2] Hamley, I. W. *Introduction to soft matter.* John Wiley: Chichester, 2000.

[3] Vaccaro, A.; Sefcik, J.; Morbidelli, M. *Polymer*, **2005**, *46*, 1157.

[4] Adamson, A. W. *Physical Chemistry of Surfaces.* John Wiley: New York, 1997.

[5] An, S. W.; Thirtle, P. N.; Thomas, R. K.; Baines, F. L.; Billingham, N. C.; Armes, S. P.; Penfold, J. *Macromolecules*, **1999**, *32*, 2731.

[6] Ballauff, M. *Prog. Polym. Sci.*, **2007**, *32*, 1135.

[7] Evans D. F.; Wennerström H. *The colloidal domain.* John Wiley: New York, 1999.

[8] Horvath, A. E. *PhD thesis.* Royal Institute of Technology, Stockholm, Sweden, 2003.

[9] Dobrynin, A. V.; Deshkovski A.; Rubinstein M. *Macromolecules*, **2001**, *34*, 3421.

[10] Čakara, D. *PhD thesis.* University of Geneva, Geneva, Switzerland, 2004.

[11] Baes, C. F.; Mesmer, R. E. *The Hydrolysis of Cations.* John Wiley: New York, 1981.

[12] Borkovec, M. *Measuring Particle Size by Light Scattering, in Handbook of Applied Surface and Colloid Chemistry.* John Wiley: New York, 1948.

[13] Berne, B. J.; Pecora, R. *Dynamic Light Scattering.* John Wiley: New York, 1976.

[14] Sefcik, J.; Verduyn, M.; Storti, G.; Morbidelli, M. *Prog. Colloid Polym. Sci.*, **2004**, *126*, 108.

[15] Derjaguin, B. W.; Landau, L. *Acta Physicochim. URRS*, **1941**, *14*, 633.

[16] Verwey, E. J.; Overbeek, J. T. G. *Theory of the Stability of Lyophobic Colloids.* Elsevier: Amsterdam, 1948.

[17] Russel, W. B.; Saville, D. A.; Schowalter, W. R. *Colloidal Dispersions.* Cambridge Univ. Press: Cambridge, 1989.

[18] Hiemenz, P. C.; Rajagopalan, R. *Principle of Colloid and Surface Chemistry.* Dekker: New York, 1997.

[19] Israelachvili, J. N. *Intermolecular and Surface Forces.* Academic Press: London, 1991.

[20] Allen, L. H.; Matijevic, E. *J. Colloid Interface Sci.*, **1969**, *31*, 287.

[21] Allen, L. H.; Matijevic, E. *J. Colloid Interface Sci.*, **1970**, *33*, 420.

[22] Higashitani, K.; Kondo, M.; Hatade, S. *J. Colloid Interface Sci.*, **1991**, *142*, 204.

[23] Depasse, J.; Watillon, A. *J. Colloid Interface Sci.*, **1970**, *33*, 430.

[24] Depasse, J. *J. Colloid Interface Sci.*, **1999**, *220*, 174.

[25] Harding, R.D. *J. Colloid Interface Sci.*, **1971**, *35*, 172.

[26] Kobayashi, M.; Juillerat, F.; Galletto, P.; Bowen, P.; Borkovec, M. *Langmuir*, **2005**, *21*, 5761.

[27] Kihira, H.; Matijevic, E. *Langmuir*, **1992**, *8*, 2855.

[28] Chang, S. Y.; Ring, E. M.; Trujillo, T. A. *Colloid Polym. Sci.*, **1991**, *269*, 843.

[29] Kihira, H.; Ryde, N.; Matijevic, E. *J. Chem. Soc. Faraday Trans.*, **1992**, *88*, 2379.

[30] Killmann, E.; Adolph, H. *Colloid Polym. Sci.*, **1995**, *273*, 1071.

[31] Barany, S.; Cohen Stuart, M. A., Fleer, G. J. *Colloids Surf. A*, **1996**, *106*, 213.

[32] Stöber, W.; Fink, A.; Bohn, E. *J. Colloid Interface Sci.*, **1968**, *26*, 62.

[33] de Keizer, A.; van der Ent, E. M.; Koopal, L. K. *Colloids Surf. A*, **1998**, *142*, 303.

[34] Wells, J.D.; Koopal, L. K.; de Keizer, A. *Colloids Surf. A*, **2000**, *166*, 171.

[35] Minor, M.; van der Linde, A. J.; van Leeuwen, H. P.; Lyklema, J. *Colloids Surf. A*, **1998**, *142*, 165.

[36] Kerker, M. *The Scattering of Light and Other Electromagnetic Radiations.* Academic Press: New York, 1969.

[37] Stumm, W.; Morgan, J. J. *Aquatic Chemistry.* John Wiley: New York, 1996.

[38] Kinniburgh, D. G.; Milne, C. J.; Venema, P. *Soil Sci. Soc. Am. J.*, **1995**, *59*, 417.

[39] Borkovec, M.; Jönsson, B.; Koper, G. J. M. *Colloid Surface Sci.*, **2001**, *16*, 99.

[40] Holthoff, H.; Egelhaaf, S. U.; Borkovec, M.; Schurtenberger, P.; Sticher, H. *Langmuir*, **1996**, *12*, 5541.

[41] Holthoff, H.; Schmitt, A.; Fernandez-Barbero, A.; Borkovec, M.; Cabrerizo-Vilchez, M. A.; Schurtenberger, P.; Hidalgo-Alvarez, R. *J. Colloid Interface Sci.*, **1997**, *192*, 463.

[42] Yu, W. L.; Borkovec, M. *J. Phys. Chem. B*, **2002**, *106*, 13106.

[43] Giesche, H. *in: T. Sugimoto (Ed.), Fine Particles.* Dekker: New York, 2000.

[44] Iler, R. K. *The Chemistry of Silica.* John Wiley: New York, 1979.

[45] Kitchener, J. A. *Faraday Discuss.*, **1971**, *59*, 379.

[46] Vigil, G.; Xu, Z.; Steinberg, S.; Israelachvili, J. *J. Colloid Interface Sci.*, **1994**, *165*, 367.

[47] Adler, J. J.; Rabinovich, Y. I.; Mouldgil, B. M. *J. Colloid Interface Sci.*, **2001**, *237*, 249.

[48] Zhmud, B. V.; Meruk, A.; Bergstrom, L. *J. Colloid Interface Sci.*, **1998**, *207*, 332.

[49] Hiemstra, T.; van Riemsdijk, W. H. *Colloids Surf.*, **1991**, *59*, 7.

[50] Hiemstra, T.; de Wit, J. C. M.; van Riemsdijk, W. H. *J. Colloid Interface Sci.*, **1989**, *133*, 105.

[51] Hiemstra, T.; van Riemsdijk, W. H.; Bolt, G. H. *J. Colloid Interface Sci.*, **1989**, *133*, 91.

[52] O'Brien, R. W.; White, L. R. *J. Chem. Soc. Faraday Trans. 2*, **1978**, *74*, 1607.

[53] Behrens, S. H.; Christl, D. I.; Emmerzael, R.; Schurtenberger, P.; Borkovec, M. *Langmuir*, **2000**, *16*, 2566.

[54] Honig, E. P.; Roeberse, G. J.; Wiersema, P. H. *J. Colloid Interface Sci.*, **1971**, *36*, 97.

[55] Elimelech, M.; Gregory, J.; Jia, X.; Williams, R. *Particle Deposition and Aggregation: Measurement, Modeling, and Simulation.* ButterworthHeinemann: Oxford, 1995.

[56] Behrens, S. H.; Borkovec, M.; *J. Phys. Chem. B*, **1999**, *103*, 2918.

[57] Pericet-Camara, R.; Papastavrou, G.; Behrens, S. H.; Borkovec, M. *J. Phys. Chem. B*, **2004**, *108*, 19467.

[58] Schudel, M.; Behrens, S. H.; Holthoff, H.; Kretzschmar, R.; Borkovec, M. *J. Colloid Interface Sci.*, **1997**, *196*, 241.

[59] Hiemstra, T.; van Riemsdijk, W. H. *Langmuir*, **1999**, *15*, 8045.

[60] van Zanten, J. H.; Elimelech, M. *J. Colloid Interface Sci.*, **1992**, *154*, 1.

[61] Samoshina Y.; Nylander T.; Shubin V.; Bauer R.; Eskilsson K. *Langmuir*, **2005**, *21*, 5872.

[62] Gillies, G.; Lin, W.; Borkovec, M. *J. Phys. Chem. B.*, **2007**, *111*, 8626.

[63] Dove, P. M.; Craven, C. M. *Geochim. Cosmochim. Acta*, **2005**, *69*, 4963.

[64] Labbez, C.; Jönsson B.; Pochard, I.; Nonat, A.; Cabane, B. *J. Phys. Chem. B*, **2006**, *110*, 9219.

[65] Kleimann J.; Gehin-Delval C.; Auweter H.; Borkovec M. *Langmuir*, **2005**, *21*, 3688.

[66] Katchalsky, A.; Mazur, J.; Spitnik, P. J. *Polymer Sci.*, **1957**, *23*, 513.

[67] *Handbook of Chemistry and Physics.* CRC Press: Cleveland, 1976.

[68] Zhang, H.; Dubin P. L.; Ray J.; Manning G. S.; Moorefield C. N.; Newkome G. R. *J. Phys. Chem. B*, **1999**, *103*, 2347.

[69] Kosmulski, M.; Matijevic, E. *Langmuir*, **1992**, *8*, 1060.

[70] Lyklema, J. *Colloids Surf., A*, **2006**, *291*, 3.

[71] Labbez, C.; Jönsson, B. *Lect. Note Comp. Sci.*, **2007**, vo26, 4699.

[72] Jönsson, B.; Nonat, A.; Labbez, C.; Cabane, B.; Wennerström, H. *Langmuir*, **2005**, *21*, 9211.

[73] Dr. Christophe Labbez, University of Bourgogne in Dijon, France (personal communication).

[74] Liu, A. *Colloids Surf., A*, **2000**, *174*, 245.

[75] Bauer, D.; Killmann, E.: Jaeger, W. *Prog. Colloid Polym. Sci.*, **1998**, *109*, 161.

[76] Schmitt, J.; Gruenewald, T.; Decher, G.; Pershan, P. S.; Kjaer, K.; Lösche, M. *Macromolecules*, **1993**, *26*, 7058.

[77] Lösche, M.; Schmitt, J.; Decher, G.; Bouwman W. G.; Kjaer K. *Macromolecules*, **1998**, *31*, 8893.

[78] Rustemeier, O.; Killmann, E. *J. Colloid Interface Sci.*, **1997**, *190*, 360.

[79] Mir, Y.; Auroy P.; Auvray L. *Phys. Rev. Lett.*, **1995**, *75*, 2863.

[80] Estrela-Lopis, I.; Leporatti, S.; Moya, S.; Brandt, A.; Donath, E.; Möhwald, H. *Langmuir*, **2002**, *18*, 7861.

[81] Verwey, E. J. W.; Overbeek, J. T. G. *Theory of Stability of Lyophobic Colloids.* Elsevier: Amsterdam, 1948.

[82] Matijevic, E.; Shulz, K.; Mirnik, M.; Herak, J.; Vouk, V. B.; Slunjski, M.; Babic, S.; Kratohvil, J.; Palmar, T. J. *Phys. Chem.* **1953**, *57*, 301.

[83] Healy, T. W.; Homola, A.; James, R. O.; Hunter, R. *J. Faraday Discuss.* **1978**, 156.

[84] Weitz, D. A.; Oliveria, M. *Phys. ReV. Lett.* **1984**, *52*, 1433.

[85] Holthoff, H.; Borkovec, M.; Schurtenberger, *P. Phys. Rev. E*, **1997**, *56*, 6945.

[86] Lattuada, M.; Wu, H.; Morbidelli, M. *J. Colloid Interface Sci.*, **2003**, *268*, 106.

[87] Lopez-Leon, T.; Gea-Jodar, P. M.; Bastos-Gonzalez, D.; Ortega-Vinuesa, J. L. *Langmuir*, **2005**, *21*, 87.

[88] Hall, R. J.; Pinkrah, V. T.; Chowdhry, B. Z.; Snowden, M. *J. Colloids Surf. A*, **2004**, *233*, 25.

[89] Rasa, M.; Philipse, A. P.; Meeldijk, J. D. *J. Colloid Interface Sci.*, **2004**, *278*, 115.

[90] Kim, A. Y.; Hauch, K. D.; Berg, J. C.; Martin, J. E.; Anderson, R. A. *J. Colloid Interface Sci.*, **2003**, *260*, 149.

[91] Puertas, A. M.; Fernandez-Barbero, A.; de las Nieves, F. J. *J. Colloid Interface Sci.*, **2003**, *265*, 36.

[92] Puertas, A. M.; Fernandez-Barbero, A.; de las Nieves, F. J. *J. Chem. Phys.*, **2001**, *114*, 591.

[93] Ouali, I.; Pefferkorn, E.; Elaissari, A.; Pichot, C.; Mandrand, B. *J. Colloid Interface Sci.*, **1995**, *171*, 276.

[94] James, R. O.; Homola, A.; Healy, T. W. *J. Chem. Soc., Faraday Trans. 1*, **1977**, *73*, 1436.

[95] Horn, D.; Linhart, F. *Retention aids. 2nd ed.* Blackie Academic and Professional: Glasgow, 1996.

[96] Muster, T. H.; Toikka, G.; Hayes, R. A.; Prestidge, C. A.; Ralston, *J. Colloids Surf. A*, **1996**, *106*, 203.

[97] Gillies, G.; Kappl, M.; Butt, H. J. *Langmuir*, **2005**, *21*, 5882.

[98] Ji, Y. Q.; Black, L.; Weidler, P. G.; Janek, M. *Langmuir*, **2004**, *20*, 9796.

[99] Grabbe, A.; Horn, R. G. *J. Colloid Interface Sci.*, **1993**, *157*, 375.

[100] Behrens, S. H.; Borkovec, M. *Phys. Rev. E*, *1999*, *60*, 7040.

[101] Behrens, S. H.; Borkovec, M. *J. Chem. Phys.*, **1999**, *111*, 382.

[102] Carnie, S. L.; Chan, D. Y. C. *J. Colloid Interface Sci.*, **1993**, *161*, 260.

[103] Chan, D.; Perram, J. W.; White, L. R.; Healy, T. W. *J. Chem. Soc., Faraday Trans. 1*, **1975**, *71*, 1046.

[104] Biesheuvel, P. M. *J. Colloid Interface Sci.*, **2004**, *275*, 514.

[105] Adamczyk, Z.; Weronski, P. *Adv. Colloid Interface Sci.*, **1999**, *83*, 137.

[106] Elimelech, M. *J. Colloid Interface Sci.* **1991**, *146*, 337.

[107] Privman, V.; Frisch, H. L.; Ryde, N.; Matijevic, E. *J. Chem. Soc., Faraday Trans.*, **1991**, *87*, 1371.

[108] Ryde, N.; Kallay, N.; Matijevic, E. *J. Chem. Soc., Faraday Trans.*, **1991**, *87*, 1377.

[109] Grolimund, D.; Elimelech, M.; Borkovec, M.; Barmettler, K.; Kretzschmar, R.; Sticher, H. *Environ. Sci. Technol.*, **1998**, *32*, 3562.

[110] Yang, J.; Bos, R.; Poortinga, A.; Wit, P. J.; Belder, G. F.; Busscher, H. J. *Langmuir*, **1999**, *15*, 4671.

[111] Luthi, Y.; Ricka, J.; Borkovec, M. *J. Colloid Interface Sci.*, **1998**, *206*, 314.

[112] Bohmer, M. R.; van der Zeeuw, E. A.; Koper, G. J. M. *J. Colloid Interface Sci.*, **1998**, *197*, 242.

[113] Mann, E. K.; van der Zeeuw, E. A.; Koper, G. J. M.; Schaaf, P.; Bedeaux, D. *J. Phys. Chem.*, **1995**, *99*, 790.

[114] Adamczyk, Z.; Siwek, B.; Zembala, M.; Warszynski, P. *J. Colloid Interface Sci.*, **1989**, *130*, 578.

[115] Ryde, N.; Matijevic, E. *J. Chem. Soc., Faraday Trans.*, **1994**, *90*, 167.

[116] Yu, W. L.; Matijevic, E.; Borkovec, M. *Langmuir*, **2002**, *18*, 7853.

[117] Ryde, N. P.; Matijevic, E. *Colloids Surf. A*, **2000**, *165*, 59.

[118] Galletto, P.; Lin, W.; Mishchenko, M. I.; Borkovec, M. *J. Chem. Phys.*, **2005**, *292*, 139.

[119] Mishchenko, M. I.; Travis, L. D.; Lacis, A. A. *Scattering, Absorption, and Emission of Light by Small Particles.* Cambridge University Press: Cambridge, 2002.

[120] Jeffrey, D. J.; Onishi, Y. *J. Fluid Mech.*, **1984**, *139*, 261.

[121] Borkovec, M.; Behrens, S. H.; Semmler, M. *Langmuir*, **2000**, *16*, 5209.

[122] Behrens, S. H.; Semmler, M.; Borkovec, M. *Prog. Colloid Polym. Sci.*, **1998**, *110*, 66.

[123] Forster, S.; Wenz, E.; Lindner, P. *Phys. Rev. Lett.*, **1996**, *77*, 95.

[124] Auroy, P.; Auvray, L.; Leger, L. *Macromolecules*, **1991**, *24*, 2523.

[125] Auroy, P.; Mir, Y.; Auvray, L. *Phys. Rev. Lett.*, **1992**, *69*, 93.

[126] Hone, J. H. E.; Cosgrove, T.; Saphiannikova, M.; Obey, T. M.; Marshall, J. C.; Crowley, T. L. *Langmuir*, **2002**, *18*, 855.

[127] Pedersen, J. S. *Adv. Colloid Interface Sci.*, **1997**, *70*, 171.

[128] Pedersen, J. S.; Svaneborg, C.; Almdal, K.; Hamley, I. W.; Young, R. N. *Macromolecules*, **2003**, *36*, 416.

[129] Marshall, J. C.; Cosgrove, T.; Leermakers, F.; Obey, T. M.; Dreiss, C. A. *Langmuir*, **2004**, *20*, 4480.

[130] Decher, G. *Science*, **1997**, *277*, 1232.

[131] Likos, C. N.; Vaynberg, K. A.; Lowen, H.; Wagner, N. J. *Langmuir*, **2000**, *16*, 4100.

[132] Strunz, P.; Saroun, J.; Keiderling, U.; Wiedenmann, A.; Przenioslo, R. *J. Appl. Crystallogr.*, **2000**, *33*, 829.

[133] Pedersen, J. S. *J. Appl. Crystallogr.*, **1994**, *27*, 595.

[134] Kinning, D. J.; Thomas, E. L. *Macromolecules*, **1984**, *17*, 1712.

[135] Stieger, M.; Pedersen, J. S.; Lindner, P.; Richtering, W. *Langmuir*, **2004**, *20*, 7283.

[136] Seebergh, J. E.; Berg, J. C. *Colloids Surf., A*, **1995**, *100*, 139.

[137] Gittings, M. R.; Saville, D. A. *Colloids Surf., A*, **1998**, *141*, 111.

[138] Peula, J. M.; Fernandez-Barbero, A.; Hidalgo-Alvarez, R.; delasNieves, F. J. *Langmuir*, **1997**, *13*, 3938.

[139] Marlow, B. J.; Rowell, R. L. *Langmuir*, **1991**, *7*, 2970.

[140] Freltoft, T.; Kjems, J. K.; Sinha, S. K. *Phys. Rev. B: Condens. Matter*, **1986**, *33*, 269.

[141] Seelenmeyer, S.; Deike, I.; Rosenfeldt, S.; Norhausen, C.; Dingenouts, N.; Ballauff, M.; Narayanan, T.; Lindner, P. *J. Chem. Phys.*, **2001**, *114*, 10471.

[142] Sinn, C.; Niehuser, R.; Overbeck, E.; Palberg, T. *Part. Part. Syst. Charact.*, **1999**, *16*, 95.

[143] Wallace, W. E.; Beck Tan, N. C.; Wu, W. L.; Satija, S. *J. Chem. Phys.*, **1998**, *108*, 3798.